Title
Extending flight time and range of eVTOL aircraft via modularity and novel design

Author
Jain, Karan P.

Publication Date
2023

Peer reviewed|Thesis/dissertation

Extending Flight Time and Range of eVTOL Aircraft via Modularity and Novel Design

By

Karan Pradeep Jain

A dissertation submitted in partial satisfaction of the

requirements for the degree of

Doctor of Philosophy

in

Engineering - Mechanical Engineering

in the

Graduate Division

of the

University of California, Berkeley

Committee in charge:

Assistant Professor Mark Mueller, Chair
Associate Professor Koushil Sreenath
Professor Pieter Abbeel

Spring 2023

Extending Flight Time and Range of eVTOL Aircraft via Modularity and Novel Design

Abstract

Extending Flight Time and Range of eVTOL Aircraft via Modularity and Novel Design

by

Karan Pradeep Jain

Doctor of Philosophy in Engineering - Mechanical Engineering

University of California, Berkeley

Assistant Professor Mark Mueller, Chair

Electric vertical takeoff and landing (eVTOL) aircraft are employed in several applications such as aerial photography, delivery, search and rescue missions owing to their compactness and ability to hover. However, they inherently have lower endurance and range as compared to their fixed-wing counterparts. Existing approaches to address this issue have explored increasing the mechanical, electrical, or aerodynamic efficiency of the system, replacing the batteries of the drone on ground stations, recharging them in-flight via large wireless chargers or laser power beaming, and several other innovative solutions exist.

Given the demand for long-duration flights and long range for applications such as drone delivery and urban aerial mobility (UAM), this dissertation explores various ways to increase the endurance of eVTOLs by adding modularity and incorporating novel design and talks about the interesting challenges that arise from them.

We begin by calculating how the flight time of an eVTOL is affected by simply adding more battery. We find that there is a fundamental flight time limit for hovering eVTOL that cannot be exceeded by just adding more battery. This motivates the exploration of new designs and approaches to improve their endurance.

First, we explore a simple approach of tethering a series of multirotors to a power source. We evaluate the power requirements to run such a system which helps in design optimization and can be used to guarantee electrical safety. We discover that there exists a critical boundary of thrusts the multirotors can produce that cannot be exceeded due to fundamental electrical limitations. The boundary can be manipulated by changing the voltage of the power supply or the resistance of the cables. We also compare the power consumption for one tethered quadcopter and two tethered quadcopters and show that for large quadcopters far enough from the anchor point, a two-quadcopter system consumes lesser power.

Next, we explore the idea of using the multirotor battery in stages to discard the discharged portion of the battery which results in lower power consumption due to reduced mass. We

find that even if we stage the energy source continuously (e.g. gasoline in a combustion engine), there still exists a fundamental flight time limit that cannot be exceeded. We consider two optimal staging problems that aim to maximize the flight time and present analytical or visual solutions which are validated experimentally.

Then, we present the idea of flying batteries – modular batteries that can fly to a mission quadcopter, dock with it, power and recharge it in-flight, and fly away after discharging, allowing us to repeat the process. This approach lifts the limitation due to energy storage. We present an analysis to evaluate the constraints that need to be satisfied to unlock unlimited endurance for eVTOL aircraft. We then discuss a stochastic model that can be used to predict the probability of success of a long-duration mission when using flying batteries.

Lastly, we present a computer vision-based solution that can be used to get the flying batteries system working in the real world. The solution involves using purely onboard sensing for the mission vehicle via a combination of an inertial measurement unit (IMU) and a camera that can generate pose measurements with respect to the flying battery. Measurements from these sensors can be fused to generate relative state estimates that can be used to dock two vehicles in-flight with a centimeter-level precision.

We strive to experimentally validate the analysis and proposed approaches presented throughout this thesis.

Contents

Acknowledgments

I would like to thank my parents Kavita Jain and Pradeep Jain, my brother Samar Jain, and my grandparents for their love, knowledge, and encouragement through all the stages of my life so far. Mummy, thanks for sending home-cooked food items from the other side of the Earth. Papa, thanks for your words of wisdom. Dada, thanks for keeping me updated with world news. Monty, thanks for being a constant source of entertainment. And everyone else, thank you for standing by me. I would also like to thank my fiancee Ritika Shrivastava for her unwavering love and support during my Ph.D. and through the last few years. The invaluable time spent with you all made me who I am today and makes me look forward to a bright future with all of you.

It has been an honor being advised by Professor Mark Mueller. Thank you for inspiring me to be ambitious and for your incredible mentorship and guidance in my research as well as my personal goals. Your subtle but witty sarcasm never fails to get me. I hope to continue to uphold the same level of excellence and ambition you instilled in me throughout the rest of my career.

I thank Professor Mark Mueller, Professor Koushil Sreenath, and Professor Pieter Abbeel for serving on my dissertation committee. I am also thankful to Professor Venkat Anantharam and Professor Kameshwar Poolla for serving on my qualifying exam committee.

Thanks to all my colleagues at UC Berkeley: Clark, Nathan, Xiangyu, Prasanth, Jaeseung, Jerry, Ting-Hao, Aakash, Elvis, Minos, Trey, Junseok, Ean, Daisy, Teaya, Carlo, and many more. I learned a lot from you and thanks for your help with my research at Berkeley. I will cherish the time we worked together (and went to free food events).

I would also like to give a shoutout to Anurag, Aviral, Shubham, and Sid, who have been a great source of personal as well as professional support, and extend this thanks to Curry Junta. I love hiking, biking, cooking, and playing frisbee with you all.

Finally, the works in this thesis would not have been possible without funding from the following sources: the Graduate Division Block Grant, Chang-Lin Tien Graduate Fellowship, NAVER LABS, and 42air. The experimental testbed at the HiPeRLab is the result of contributions of many people, a full list of which can be found at `hiperlab.berkeley.edu/members/`.

Chapter 1

Introduction

Electric vertical takeoff and landing (eVTOL) aircraft [1] are a class of aerial vehicles that can hover, and take off from, and land on, a small space, as opposed to conventional fixed-wing aircraft that require long runways. As a result, they have emerged as a leading candidate in urban air mobility (UAM) [2] considerations. Companies such as Joby aviation [3, 4], Wisk Aero, Lilium, etc. have raised billions of dollars to develop eVTOL "air taxis" [5].

Miniature versions of eVTOL aircraft are typically seen in the form of a multicopter. An example is shown in Figure 1.1. These are employed in a number of useful tasks, including search and rescue, package delivery, cinematography, and inspection, among many additional functions [6, 7, 8, 9, 10].

Although eVTOLs are simple and useful machines, they inherently have lower endurance and range as compared to fixed-wing aircraft [11]. The low endurance is primarily due to two reasons – (i) electric energy sources (batteries) have orders of magnitude lower specific energy compared to combustion-based fuels [12], and (ii) hovering eVTOLs cannot take advantage of the high lift-to-drag ratio like fixed-wing aircraft. Moreover, there is a demand for long eVTOL flight time for applications such as surveillance, picking fruits [13], cleaning high-rise buildings, and firefighting. There is also a need for a long eVTOL range for applications such as package delivery [14], and transporting people via air taxis [15].

In this dissertation, we focus on solving the first issue via novel approaches that focus on the hardware design of the vehicles, and system architecture, to mitigate the endurance and range constraints due to limited energy storage.

1.1 Motivation – flight time of a hovering eVTOL

In this section, we analyze the flight time of a single battery-powered hovering eVTOL and show that there exists a fundamental limit to the flight time. Specifically, we show that the achievable flight time only increases up to a certain point, as more battery is used on a vehicle.

Figure 1.1: A custom-built quadcopter with motion-capture marker balls.

We model the aerodynamic power consumption p_i of an individual propeller i to be related to its thrust f_i as

$$p_i \propto f_i^{\frac{3}{2}}. \tag{1.1}$$

This can be derived from actuator disk theory [16], or from mechanical analysis of hub torque and rotational speed [17].

Assuming constant specific energy e_b, the total available energy E_{batt} in a battery will be e_b times the battery's mass.

Let m_0 be the "dry" mass (mass of all components of the eVTOL, excluding the battery), and let ϕ be the fraction of the *total* vehicle mass that is the battery mass so that the total vehicle mass is $\frac{1}{1-\phi}m_0$ and the battery mass is $\frac{\phi}{1-\phi}m_0$.

For a hovering eVTOL, the individual propeller thrusts scale proportionally with the vehicle's total mass. The electric power draw p_{elec} can be written as,

$$p_{\text{elec}} = k_p \left(\frac{1}{1-\phi} m_0\right)^{3/2}, \tag{1.2}$$

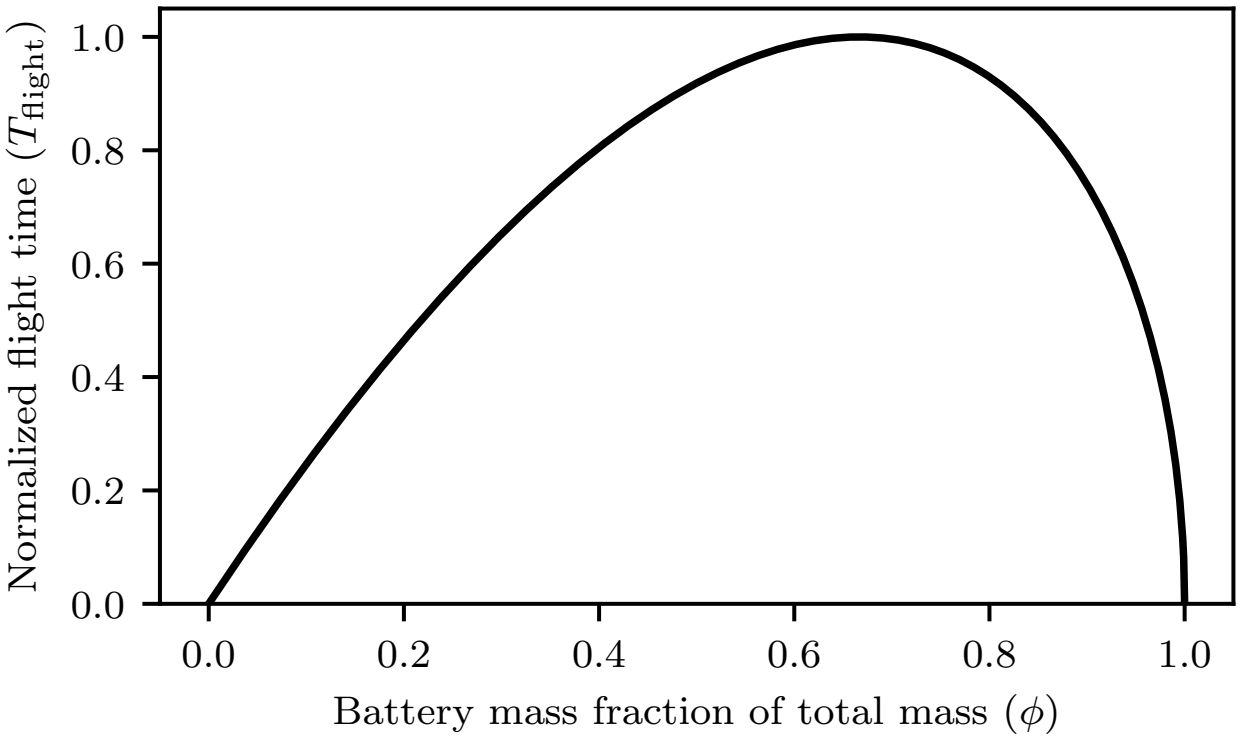

Figure 1.2: Effect of battery mass on normalized hovering flight time. After the peak at $\phi = \frac{2}{3}$, a larger battery reduces flight time.

where the power consumption coefficient k_p is determined by propeller design, gravitational acceleration, and powertrain efficiency. We assume these parameters are constant for a given vehicle.

The available flight time t_{flight} can then be related to the vehicle mass m_0, and battery mass fraction:

$$t_{\text{flight}} = \frac{E_{\text{batt}}}{p_{\text{elec}}} = \frac{e_b \frac{\phi}{1-\phi} m_0}{k_p \left(\frac{1}{1-\phi} m_0\right)^{3/2}} \propto \frac{\phi\sqrt{1-\phi}}{\sqrt{m_0}}. \tag{1.3}$$

This relationship is plotted in Figure 1.2, showing that vehicles with relatively small batteries expect to see a strong improvement in total flight time with increasing battery mass, until a peak where the battery takes up two-thirds of the vehicle's mass. Note that this is a fundamental limit for a self-contained battery-powered eVTOL which cannot be exceeded by adding more battery.

This analysis motivates the study of novel methods to exceed the flight-time limitation imposed by (1.3).

1.2 Literature survey

We present a literature survey of existing innovative approaches that aim to increase the endurance and range of eVTOL aircraft.

Broadly, we can classify the approaches into two types: self-contained and externally assisted. Self-contained methods typically involve increasing mechanical or electrical efficiency or the use of optimization-based methods over objectives such as flight time or range. One such approach is exploiting the efficiency of a fixed-wing and hovering ability of eVTOLs by converting them into a hybrid aerial vehicle [18]. Manipulation of vehicle structure by tilting rotors to increase efficiency is shown in [17]. Tilting the propellers of an eVTOL in forward flight direction to reduce drag area and hence power consumption is shown in [19]. An online strategy for optimizing efficiency by altering flight parameters (e.g. speed) over a trajectory is presented in [20]. The analysis of a solar-powered aerial vehicle, which can potentially fly for a long time, is shown in [21]. However, such a vehicle requires a large wing span, is sensitive to weather conditions, and is not suitable for indoor settings.

Externally assisted methods typically involve the use of fixed stations or mobile vehicles for the replacement or the charging of energy sources. Battery swapping at a fixed ground station has been presented in [22, 23], and on a mobile ground base has been shown in [24]. One limitation of ground-based swapping stations is an interruption to the mission. For example, if an eVTOL's mission is monitoring a target, then going to a ground station for battery replacement could result in a mission failure.

Currently, unlimited flight time has been demonstrated either by tethering the eVTOL to a power source [25], or by power beaming via microwave [26] or LASER [27]. While a tethered quadcopter has limited flight reach and maneuverability, in applications such as atmospheric analysis[28], construction/industrial inspections[29], surveillance[30], or aerial manipulation, the choice of tethering the quadcopter is a reasonable trade-off between reach and extended flight. Their uses have also been demonstrated in a variety of commercial applications such as picking fruits in an orchard [13] and cleaning buildings and wind turbine blades. Power beaming via LASER has a limited range (typically up to a kilometer [31]) and requires line of sight, so increasing the range of the eVTOL would entail having several LASER sources along the path which could be quite expensive because of the high fixed cost of installation of several LASERs and high variable cost due to low efficiency (typically less than 20% [32]).

Lastly, we have alternative energy sources that bring us out of the electric energy realm, but are still an important consideration for the objective of long-duration flight of VTOL aircraft. Fuel cell powered multirotors have been shown to have almost twice as much endurance as a lithium polymer battery-powered multirotor [33]. Hybrid electric power has also been explored for multirotors [34], and there are hybrid-powered drones in the market with a flight time as high as 13 h. This is due to the orders of magnitude higher specific energy of combustion fuels as compared to Lithium-ion batteries [12].

The takeaway from this survey is that most methods for extending the endurance of eVTOL aircraft either have an incremental effect or bring about some other restriction such as limited reach (e.g. tethering) or unreasonable cost (e.g. LASER power beaming). Even

exploring alternate energy sources such as gasoline only increases the flight time by a finite amount in the best possible case, which is proven in [35].

1.3 A note on experimental hardware in this dissertation

We note that most eVTOL components (e.g. motors, propellers, batteries, flight controllers) can be manufactured at scale, which allows eVTOLs to be built at relatively low costs. This has allowed for the widespread adoption of eVTOLs as industrial tools, as platforms for various forms of research and entertainment, and as the leading candidate in urban air mobility.

Thus, in this dissertation, the approaches for extending their endurance and range are developed such that they do not significantly reduce the simplicity of the vehicle or increase its cost, ensuring that any proposed changes to the conventional eVTOL design align with the original reasons for their widespread adoption.

Finally, because this dissertation is primarily concerned with techniques that tangibly impact the endurance of eVTOLs, each proposed concept is experimentally validated and demonstrated via flight experiments.

1.4 Dissertation outline

The dissertation is organized in increasing order of payoff to the eVTOL endurance and range, which is also positively correlated with the complexity of the system.

Chapter 2: Tethered Power for a Series of Quadcopters: Analysis and Applications. We begin with the simplest approach of mitigating energy storage constraints – by plugging in the aerial vehicle to a power supply via a tether. This eliminates any flight time limitation due to the energy source. However, this comes with the tradeoff of limited reach of the vehicles, which is governed by the tether length. We present a power analysis for a series of multirotors connected to a power supply with respect to the thrust of each multirotor which guarantees electrical safety and helps in design optimization. We also experimentally demonstrate the use of a two-quadcopter tethered system as compared to a one-quadcopter tethered system in a cluttered environment, such as passing through a window and grasping an object over an obstacle. A video of the proposed approach can be viewed at `https://youtu.be/I7NbjkcJqZg`.

Chapter 3: Staging energy sources to extend flight time of a multirotor UAV. Next, we present an approach where an aerial vehicle can eject the used portions of its energy source, getting rid of dead mass. This helps reduce power consumption and increases the flight time of the vehicle. We also show that a multirotor powered by an internal combustion engine (essentially having a continuously staged energy source) has an upper limit on achievable flight time independent of the available fuel mass. Lastly, we validate

the analysis with flight experiments on a custom two-stage battery-powered quadcopter. We achieve a 19% increase in flight time using the batteries in two stages as compared to a single stage. A video of the proposed approach can be viewed at `https://youtu.be/CUjPCRUO66U`.

Chapter 4: Unlimited endurance for eVTOL aircraft using Flying Batteries. In the remainder of the dissertation, we explore and demonstrate the concept of in-flight battery swapping, in a manner substantially different from the conventional understanding of battery swapping. Specifically, instead of having a complicated and heavy mechanism to swap batteries on a mission vehicle, we make the spare batteries modular by giving them the ability to fly and connect to the mission vehicle in flight. We call such a spare battery a "flying battery" – a small eVTOL carrying a secondary battery that can dock with the mission vehicle, and power the mission vehicle while also recharging the mission vehicle's onboard (reserve) battery. We present a flight time analysis that takes the power consumption into account to come up with requirements on the recharging rate that enable unlimited endurance for the mission vehicle. We also develop a stochastic model to characterize the probability of success of docking and that of the entire mission, which requires several flying batteries docking and undocking along the way. We perform a long-duration flight experiment involving repeated docking, battery switching plus recharging, and undocking of several flying batteries. At the end of the experiment, the primary battery on the mission vehicle is observed to be nearly fully charged, which proves that the energy storage restriction on endurance is successfully eliminated. Importantly, the unlimited endurance does not involve a complex battery swapping mechanism, is unrestricted in range, and is not associated with a large increase in overall mass or size, leaving the mission vehicle in fundamentally the same safety class. A video of the proposed approach can be viewed at `https://youtu.be/PpJIo4HXl_Q`.

Chapter 5: Docking two multirotors in midair using relative vision measurements. Finally, we explore methods to port the flying battery concept in a practical setting – with purely onboard sensing. The method we present is a partial solution to the problem. It solves the problem of precise relative localization of two eVTOL vehicles that allows them to dock reliably. We use a combination of two sensors – (i) an inertial measurement unit (IMU) to get acceleration and angular velocity measurements, and (ii) a camera-marker pair where a light-weight, low-cost camera installed on the mission vehicle which can look at a marker installed on the flying battery to get relative pose measurements. The measurements from these sensors are fused via an EKF to estimate the relative pose of the mission vehicle with respect to the flying battery, and its absolute roll and pitch. These estimates are then used to control the mission vehicle and dock it with the flying battery, which requires a centimeter-level precision. The docking using purely onboard sensing for the mission vehicle is demonstrated experimentally to be repeatable and reliable. A video of the proposed approach can be viewed at `https://youtu.be/m9YqOm3VtTM`.

Finally, the major contributions and findings are summarized in Chapter 6.

The materials in this thesis are based on the following papers:

- Karan P Jain et al. "Tethered Power Supply for Quadcopters: Architecture, Analysis and Experiments". In: *arXiv preprint arXiv:2203.08180* (2022)

- Karan P Jain et al. "Staging energy sources to extend flight time of a multirotor UAV". in: *2020 IEEE/RSJ International Conference on Intelligent Robots and Systems (IROS)*. IEEE. 2020, pp. 1132–1139

- Karan P Jain and Mark W Mueller. "Flying batteries: In-flight battery switching to increase multirotor flight time". In: *2020 IEEE International Conference on Robotics and Automation (ICRA)*. IEEE. 2020, pp. 3510–3516

- Karan P Jain et al. "Modeling of aerodynamic disturbances for proximity flight of multirotors". In: *2019 International Conference on Unmanned Aircraft Systems (ICUAS)*. IEEE. 2019, pp. 1261–1269

- Karan P Jain, Minos Park, and Mark W Mueller. "Docking two multirotors in midair using relative vision measurements". In: *arXiv preprint arXiv:2011.05565* (2020)

1.5 Contributions of this dissertation

In this section, the contributions of this dissertation are listed chapter by chapter.

Chapter 2: Tethered Power for a Series of Quadcopters: Analysis and Applications.

- We formulate the power consumption from the power supply as a function of quadcopter thrusts and study the influence of various parameters such as tether resistance and input voltage. The power analysis shows the existence of a critical boundary of thrusts beyond which it is electrically impossible to produce the thrusts.

- We show a power comparison for a fixed end-effector quadcopter position (see Figure 2.2) between one tethered quadcopter and a two tethered quadcopter system, taking into account the power analysis and catenary forces from the tether. This allows us to find configurations where two quadcopter system has a lower total power consumption that frees up thrust capacity for the end-effector quadcopter, increasing its maneuverability and agility.

- We demonstrate applications of a system of two tethered quadcopters – flying through a corridor and picking up an object in a space with obstacles.

Chapter 3: Staging energy sources to extend flight time of a multirotor UAV.

- The design space for multirotors with various discrete staging configurations is explored by analyzing the effect on flight time with respect to the energy storage mass.

- Flight time performance is also analyzed for a continuously staged source – an internal combustion engine driving propellers.
- Using energy sources in multiple stages as opposed to a single stage is shown to benefit flight time analytically and is validated experimentally.
- The environmental impacts and use cases of staging are assessed to realize specialized areas where the benefits of staging can be exploited, for example in industrial settings, emergency situations, or for interplanetary exploration missions.

Chapter 4: Unlimited endurance for eVTOL aircraft using Flying Batteries.

- We present a flight time analysis to predict the flight time added by the flying batteries, and evaluate specific constraints on the recharging rate and the energy content of the primary battery that are necessary for unlimited flight duration.
- We develop a stochastic docking model as a design tool to choose parameters for the docking mechanism and trajectory that maximizes the probability of success of a mission. Monte Carlo simulations are done to characterize this success probability theoretically. This is then experimentally validated for various docking mechanism designs.
- We experimentally validate that flying batteries can unlock unlimited endurance from an energy storage perspective. This is done in an indoor flight space using a motion-capture system for localization. The battery switching circuit design is updated to include a charging circuit to recharge the primary battery (onboard the main vehicle). The recharging rate is chosen based on the constraints from the flight time analysis to unlock unlimited endurance. Moreover, the mechanical design of the docking mechanism is modified based on the stochastic model to improve the reliability of the system, and the probability of success of docking.

Chapter 5: Docking two multirotors in midair using relative vision measurements.

- We derive a complete 6 degree of freedom (DoF) localization of one multirotor with respect to another, using only onboard sensors. Specifically, we derive a state estimation algorithm based on the extended Kalman filter (EKF) that takes, as input, inertial measurements (acceleration and angular velocity) and relative pose (position and orientation) measurements. These measurements are then used to estimate the relative position and velocity of one multirotor with respect to another, and its absolute attitude with respect to the inertial frame.

- We develop a control architecture to experimentally validate the relative localization algorithm using an onboard camera on the first quadcopter and a marker (which provides full 6 DoF information on detection) on the second, and control the first quadcopter using just the onboard estimates.
- We experimentally demonstrate mid-air docking on custom-designed quadcopters using these onboard estimates – a task that requires a position precision on the order of a centimeter.

Chapter 2

Tethered Power for a Series of Quadcopters: Analysis and Applications

Tethered quadcopters are used for extended flight operations where the power to the system is provided via a tether connected to an external power source. In this work, we consider a system of multiple quadcopters powered by a single tether. We study the design factors that influence the power requirements, such as the electrical resistance of the tether, input voltage, and quadcopters' positions. We present an analysis to predict the required power to be supplied to a series of N tethered quadcopters, with respect to the thrust of each quadcopter which guarantees electrical safety and helps in design optimization. We find that there is a critical boundary of thrusts that cannot be exceeded due to fundamental electrical limitations. We compare the power consumption for one tethered quadcopter and two tethered quadcopters and show that for large quadcopters far enough from the anchor point, a two-quadcopter system consumes lesser power. We show that, for a representative use case of firefighting, a tethered system with two quadcopters consumes 26% less power than a corresponding system with one quadcopter. Finally, we present experiments[1] demonstrating the use of a two-quadcopter tethered system as compared to a one-quadcopter tethered system in a cluttered environment, such as passing through a window and grasping an object over an obstacle.

The material in this chapter is based on the following work uploaded to arXiv.

- Karan P Jain et al. "Tethered Power Supply for Quadcopters: Architecture, Analysis and Experiments". In: *arXiv preprint arXiv:2203.08180* (2022)

[1]The explanation and experimental validation video can be found here: `https://youtu.be/I7NbjkcJqZg`

2.1 Introduction

Aerial vehicles like quadcopters are used in various applications, from surveillance to manipulation to exploring other planets[40, 41]. While these vehicles are primarily utilized for passive tasks such as surveillance[42] and photography[43], research groups and industries actively pursue aerial vehicles for manipulation tasks involving grasping/positioning[44], assembling/dismantling parts[45], or transporting payloads[46] using one or more vehicles.

Aerial vehicles, however, are largely constrained in their flight time, and payload capacity, due to their limited hardware and power supply. Various innovations towards extending the flight time and range of quadcopters have been explored. Methods such as swapping the batteries at a ground station[22], replacing batteries in-flight using other quadcopters[37], and using the batteries in multiple stages[35] have demonstrated increased flight times. However, these systems can run out of power if not replaced in time and would require the quadcopters to land.

An alternate approach to extend flight time is to supply the power through an external tether from a fixed/mobile ground station. While a tethered quadcopter has limited flight reach and maneuverability, in applications such as atmospheric analysis[28], construction/industrial inspections[29], surveillance[30], or aerial manipulation, the choice of tethering the quadcopter is a reasonable trade-off between reach and extended flight. Their uses have also been demonstrated in a variety of commercial applications such as picking fruits in an orchard [13] and cleaning buildings and wind turbine blades.

Most tethered aerial systems are limited to only vertical flights, especially when carrying heavy tethers such as in cleaning buildings. A single tethered system is limited in their horizontal reachability. Works such as [47, 48] consider a new type of system consisting of a series of tethered quadcopters to improve the reachability of the tethered systems, especially in cluttered environments.

Related Work

Quadcopter systems tethered to a fixed or moving base have been explored in the past [49, 50, 51, 52]. Control algorithms for the tethered quadcopters were developed in [53], where the tether is modeled as a massless rigid link. To account for the mass of the cable during dynamic maneuvers, the tether is modeled as a series of lumped mass links in [54, 55]. Catenary models are used to model the tether in [56, 57], however, such models can be used only under quasi-static conditions. A system of tethered quadcopters connected in series is studied in [47, 48, 58]. A string of quadcopters would extend the horizontal reachability as well as the ability to navigate in a cluttered environment.

Although tethering a quadcopter to a power supply provides access to unlimited energy, a power analysis is useful to guarantee that the power draw of the system is within the rated limit of the supply. It is also beneficial in choosing the right type of tether since there is a trade-off between the mass of the tether (influencing the thrust and power requirements on the quadcopter) and the resistance of the tether (influencing the resistive power losses).

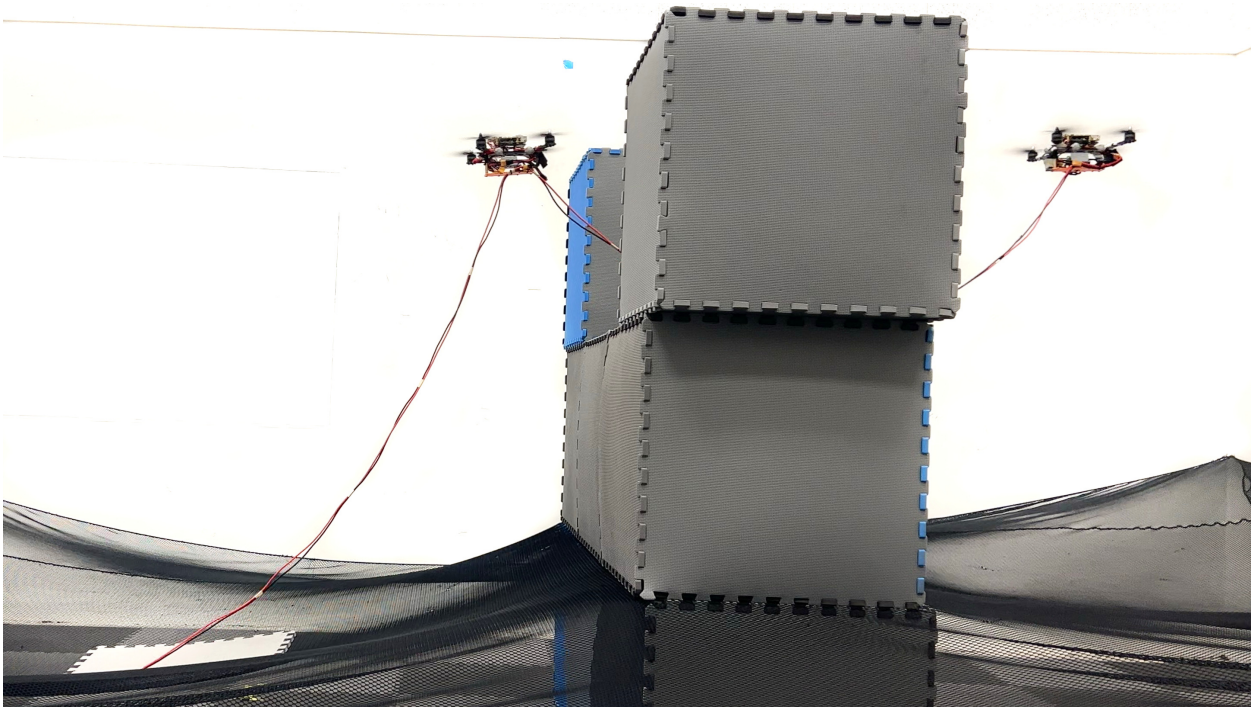

Figure 2.1: Experiment demonstrating two quadcopters tethered using a single cable, supplying power from an external power source. The quadcopters are electrically connected in parallel. Multiple quadcopters can be used collaboratively to achieve tethered flight over unknown/challenging terrain while increasing the horizontal reachability of the quadcopter. A video for the experiment is provided as an attachment.

Energy analysis for a downward tethered quadcopter that is not externally powered is shown in [59]. Power supply for tethered drones is analyzed in [49], where comparisons between a battery-operated drone and a tethered drone with an external DC power source are drawn. In, [25], power analysis for a single tethered quadcopter with respect to various factors such as input voltage, wire resistance, and cable length has been discussed, but the effects of catenary forces on the power were not considered. Moreover, extending the power to multiple quadcopters increases the complexity of the system and requires further study.

Contributions

In this work, we look into multiple quadcopters powered via a single tether from an external power source. The contributions of this work are as follows:

- We formulate the power consumption as a function of quadcopter thrusts and study

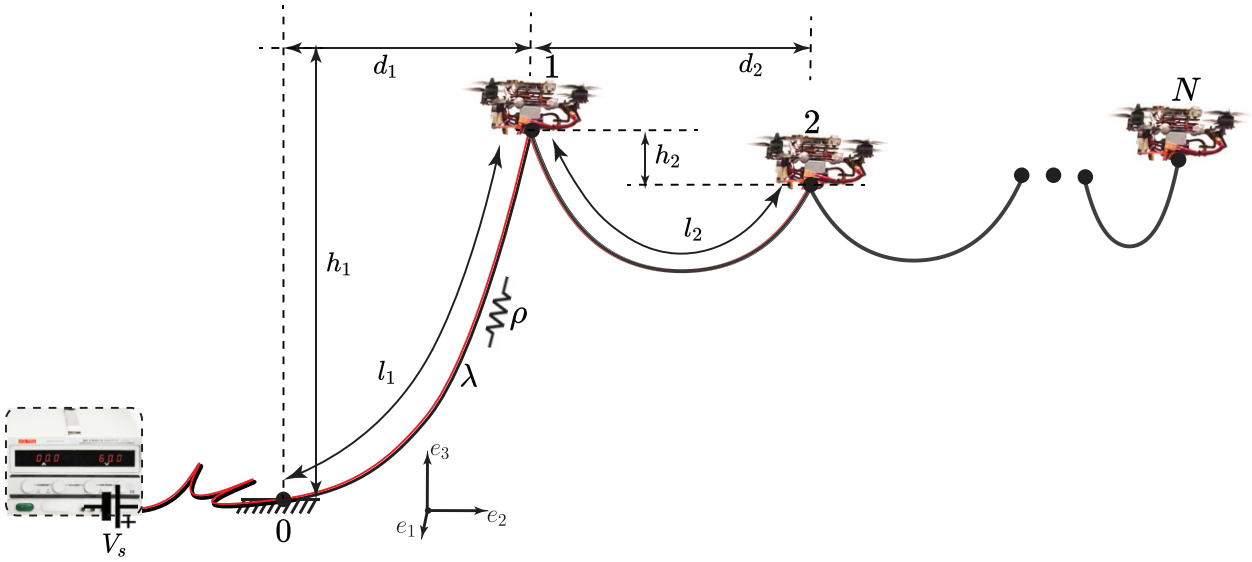

Figure 2.2: Schematic for a series of quadcopters in hover tethered to an external power source using a single tether. The last (N-th) quadcopter is referred to as the end-effector quadcopter.

the influence of various parameters such as tether resistance and input voltage. The power analysis shows the existence of a critical boundary of thrusts beyond which it is electrically impossible to produce the thrusts.

- We show a power comparison for a fixed end-effector quadcopter position (see Figure 2.2) between one tethered quadcopter and a two tethered quadcopter system, taking into account the power analysis and catenary forces from the tether. This allows us to find configurations where two quadcopter system has a lower total power consumption that frees up thrust capacity for the end-effector quadcopter, increasing its maneuverability and agility.

- Finally, we demonstrate applications of a system of two tethered quadcopters – flying through a corridor and picking up an object in a space with obstacles.

2.2 System Description

In this section, we describe a series of identical quadcopters powered by a single tether connected to a power source and review various factors influencing the power requirement of the system under quasi-static hover conditions.

Variables	Definition
m_j	Mass of Quadcopter j [kg]
l_j	Tether length between Quadcopter $j-1$ and j [m]
λ_j	Tether mass per unit length of the j-th section [$\mathrm{kg\,m^{-1}}$]
L	Total tether length in the system [m]
f_j	Scalar thrust magnitude of Quadcopter j [N]
$\mathbf{t} \in \mathbb{R}^3$	Force vector on the quadcopter due to the tether [N]
P_s	Power supplied by the source [W]
V_s	Voltage at the source [V]
i_s	Current delivered by the source [A]
P_j	Power consumption of Quadcopter j [W]
V_j	Voltage across Quadcopter j [V]
i_j	Current consumed by Quadcopter j [A]
ρ_j	Tether resistance per unit length of j-th section [$\Omega\,\mathrm{m^{-1}}$]
R_j	Tether resistance of the j-th section [Ω]

Table 2.1: List of various symbols representing mechanical and electrical quantities used in this work.

Consider a uniform tether supply connected to an external power source attached to the quadcopters as shown in Figure 2.2. One end of the tether is attached to a quadcopter and the other is fixed to the ground (indexed 0). We assume the tether is rigidly attached to the center-of-mass of the quadcopter, i.e., the tether applies only translation force on the quadcopter. Each quadcopter is indexed $i = \{1, 2, \ldots, N\}$, in ascending order away from the power source.

Let the length of the cable segment between the quadcopters $i-1$ and i be l_i. The horizontal and vertical distances between the quadcopters are given as h_i and d_i, respectively. Without loss of generality, we consider the system to be in a single catenary plane for the rest of the chapter. The total length of the tether from the power source to the last quadcopter N is L. We assume the tether is uniform along its length, with λ mass per unit length. Table 2.1 lists the various symbols used in this work. With no external disturbances, the thrust required by each quadcopter at hover is,

$$f_i = \|m_i g \mathbf{e_3} - \mathbf{t}_i - \mathbf{t}_{i+1}\|, \tag{2.1}$$

where m_i is the mass of the quadcopter and $\mathbf{t}_i$, $\mathbf{t}_{i+1}$ are the catenary forces due to the tether on either side of the quadcopter.

A uniform cable suspended between two fixed points forms a catenary curve[60], where the equation in the catenary plane is expressed using the catenary parameters a, b, c as,

$$z = a \cosh\left((y - b)/a\right) + c, \tag{2.2}$$

and can be numerically solved using the position of the endpoints. At hover, under quasi-static conditions, the tether between the quadcopters takes the catenary shape. The catenary parameter a_i for each tether segment is computed by numerically solving the transcendental equation,

$$\sqrt{l_i^2 - h_i^2} = 2a_i \sinh^2(\tfrac{d_i}{2a_i}), \tag{2.3}$$

and parameters b_i, c_i are computed as follows,

$$b_i = \tfrac{d_i}{2} - a_i \tanh^{-1}(h_i/l_i), c_i = -a_i \cosh(-b_i)/a_i. \tag{2.4}$$

To solve for the catenary forces $\mathbf{t}_i$, $\mathbf{t}_{i+1}$ at the ends of the tether segment, directions of the catenary forces at the ends are computed using the gradient of the catenary equation. The magnitude of the tensions is calculated by equating the net catenary forces to the weight of the tether (at quasi-static equilibrium).

Making use of the thrust generated by a quadcopter in (2.1) at hover, we compute the electrical power consumption of the power train, using actuator disk model (see [35]) as,

$$P_i = c_p f_i^{\frac{3}{2}}, \tag{2.5}$$

where the power constant c_p is a function of the propeller size A_{prop}, ambient air density ρ_{air}, propeller efficiency η_{prop} based on the propeller figure of merit, powertrain efficiency η_{pt}, and number of propellers n,

$$c_p = \frac{1}{\eta_{\text{prop}}\eta_{\text{pt}}\sqrt{2\rho_{\text{air}} n A_{\text{prop}}}}. \tag{2.6}$$

We assume that the propeller and powertrain efficiency is constant and neglects power consumption by the onboard sensors and computers.

To optimally design a power-supply system and to choose the various design factors for tethered quadcopters flight, we need to understand the effect of various design parameters which are considered in the next section.

2.3 Electrical Power Analysis

As mentioned in Section 2.1, power analysis can provide guarantees of being within rated limits of the power supply which ensures safety, and help in optimizing for design parameters such as tether resistance and input voltage.

We analyze the power consumption and power supply requirements for N quadcopters tethered to a single power supply with respect to the thrust that each quadcopter produces. Consider N quadcopters connected electrically in parallel as shown in Figure 2.3. The portion of the tether between Quadcopter $(j-1)$ and Quadcopter j has as a resistance R_j. The $j = 1$ portion refers to the part of the tether between the power supply and Quadcopter 1.

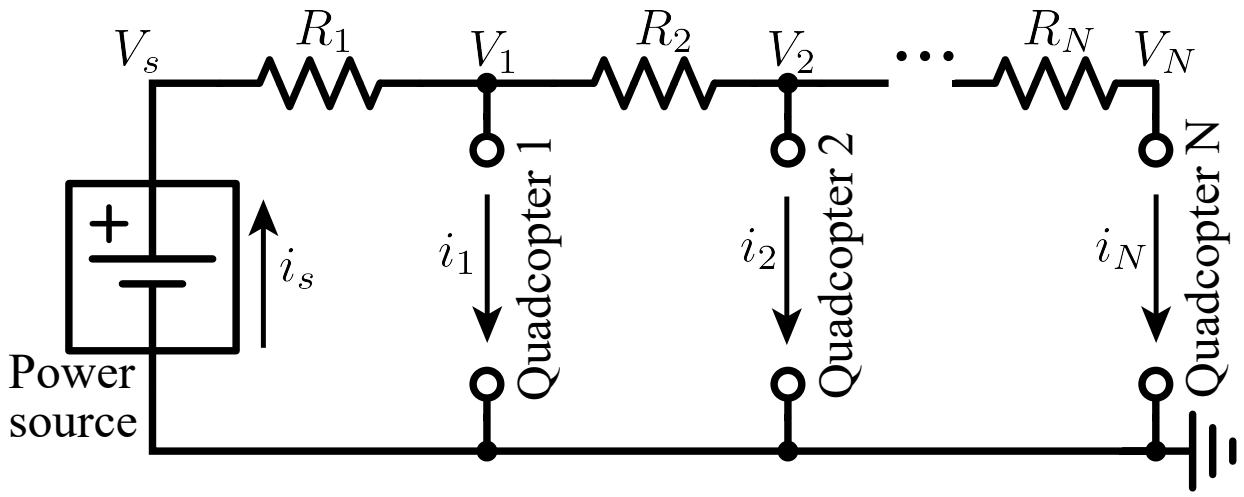

Figure 2.3: Circuit diagram for the proposed power supply architecture for N tethered quadcopters. If the resistive losses are too high, a solution is to transmit power at a high voltage via the tether.

The power supply voltage and current are denoted as V_s and i_s respectively. We assume that the thrust to be produced by the j-th quadcopter f_j is already known. Then from (2.5), we know its power consumed P_j. After the resistive voltage drop, let the voltage at the j-th quadcopter be V_j. Then the current consumption by this quadcopter will be given by,

$$V_j i_j = P_j. \tag{2.7}$$

Looking at Figure 2.3, we can apply Kirchoff's circuit laws to derive,

$$V_k = V_{k-1} - \left(\sum_{l=k}^{N} i_l \right) R_k, \quad k = 1, \ldots, N, \tag{2.8}$$

where $V_0 = V_s$. Simplifying the set of equations (2.8), we can get the voltage across the quadcopters in terms of source voltage and current consumed by the quadcopters as,

$$V_j = V_s - \sum_{k=1}^{j} \left(\sum_{l=k}^{N} i_l \right) R_k, \quad j = 1, \ldots, N. \tag{2.9}$$

We have $2N$ unknowns $(V_1, i_1, \ldots, V_N, i_N)$ but only N equations. We know the power consumption P_j by each quadcopter. Therefore, we multiply each equation in (2.9), by the

respective quadcopter current consumption i_j, to get,

$$P_j = V_s i_j - i_j \sum_{k=1}^{j} \left(\sum_{l=k}^{N} i_l \right) R_k, \quad j = 1, \ldots, N. \tag{2.10}$$

Equations (2.10) are N simultaneous quadratic equations in N variables $\{i_1, \ldots, i_N\}$, which can be solved numerically. With those values, we can get the power supplied P_s as,

$$i_s = \sum_{j=1}^{N} i_j \ , \qquad P_s = V_s i_s. \tag{2.11}$$

The analytical expression for the power supplied in terms of quadcopter thrust for $N = 1$ is,

$$P_s = \frac{V_s^2}{2R_1} \left(1 - \sqrt{1 - \frac{4c_p f_1^{3/2} R_1}{V_s^2}} \right) \tag{2.12}$$

This expression is useful to draw conclusions about the dependence of thrust boundaries for the multiple quadcopter tethered system on the design parameters. This is covered in subsequent subsections.

For the specific two quadcopters tethered system, the required supply power is plotted as a heatmap against the thrusts of the two quadcopters in Figure 2.4. Once the system application is decided and the quadcopters are designed, such a plot could be used to choose the appropriate power supply and cable which meets the power requirements at the designed thrust values of the quadcopters.

Note that there is a boundary in the plot beyond which any additional current supplied would simply increase the resistive losses and none of the extra power will reach the quadcopters. Thus any thrust combination that belongs in the white region in the plot cannot be produced. We would like to emphasize that this is not a limitation of the power source, but a fundamental electrical limitation of the tethered-quadcopters system because of the physical parameters such as resistance and power consumption requirements. This is also supported by equation (2.12), where increasing the thrust beyond a certain limit results in no real solutions for the supplied power. This limit is given by,

$$f_{\text{crit}} = \frac{V_s^{4/3}}{(4c_p)^{2/3} R^{2/3}} \tag{2.13}$$

Manipulating this thrust boundary could be of particular interest to designers to choose the power supply and tether size, given the system parameters, while guaranteeing electrical safety. Given the quadcopters' power consumption coefficient c_p, the boundary can be influenced by the following parameters: power supply voltage V_s and the tether resistances $\{R_1, \ldots, R_N\}$. This influence is studied in the following subsections.

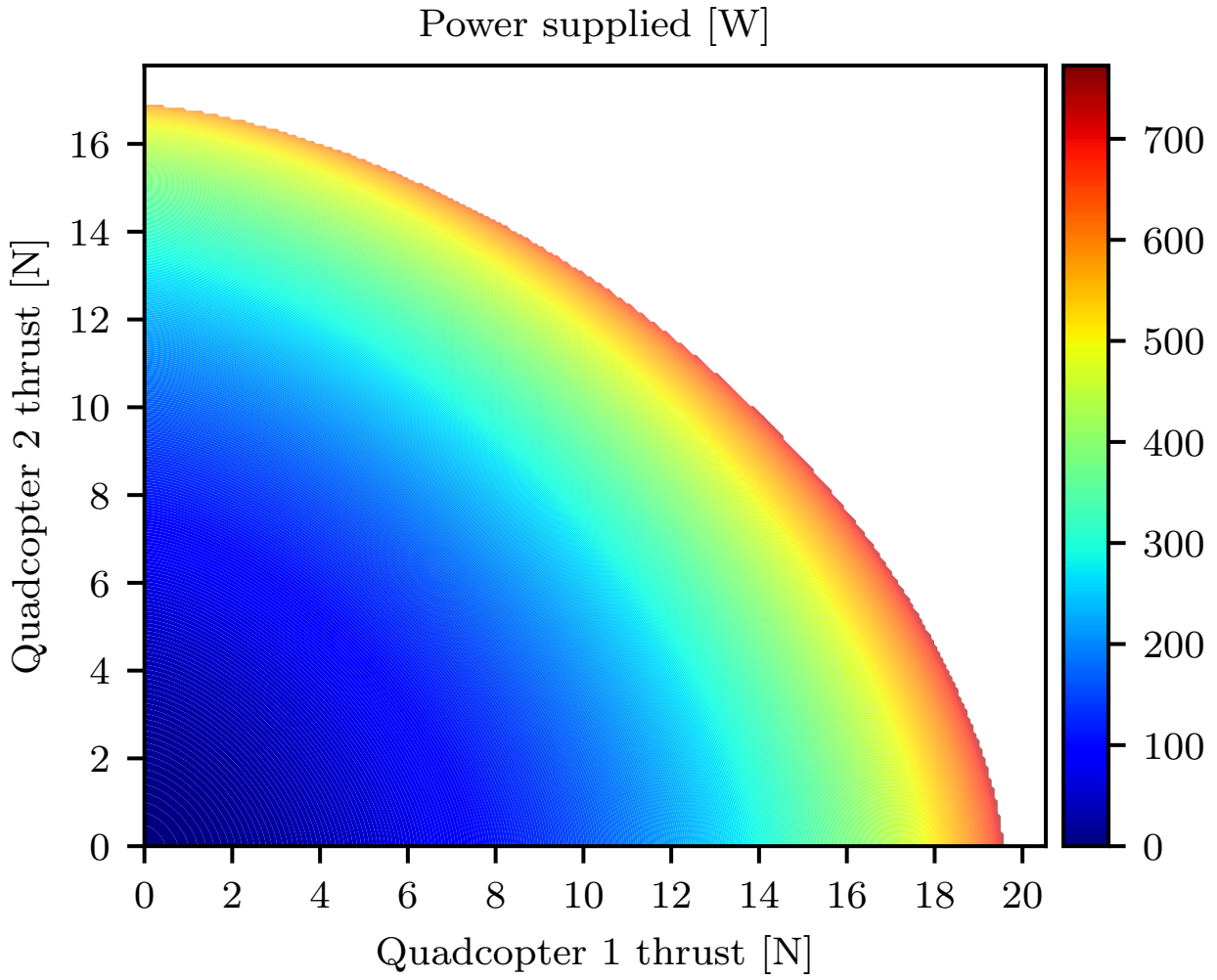

Figure 2.4: Source power P_s as a function of Quadcopter 1 thrust and Quadcopter 2 thrust. White regions indicate that the thrust combination is impossible to produce because of fundamental limitations. For this plot, the parameters are: V_s =12.6 V, 12 AWG wire ($\rho = 0.0166\,\Omega\,\mathrm{m}^{-1}$), $l_1 = 6.1\,\mathrm{m}$, $l_2 = 1.5\,\mathrm{m}$, $c_p = 4.5\,\mathrm{W/N}^{\frac{3}{2}}$.

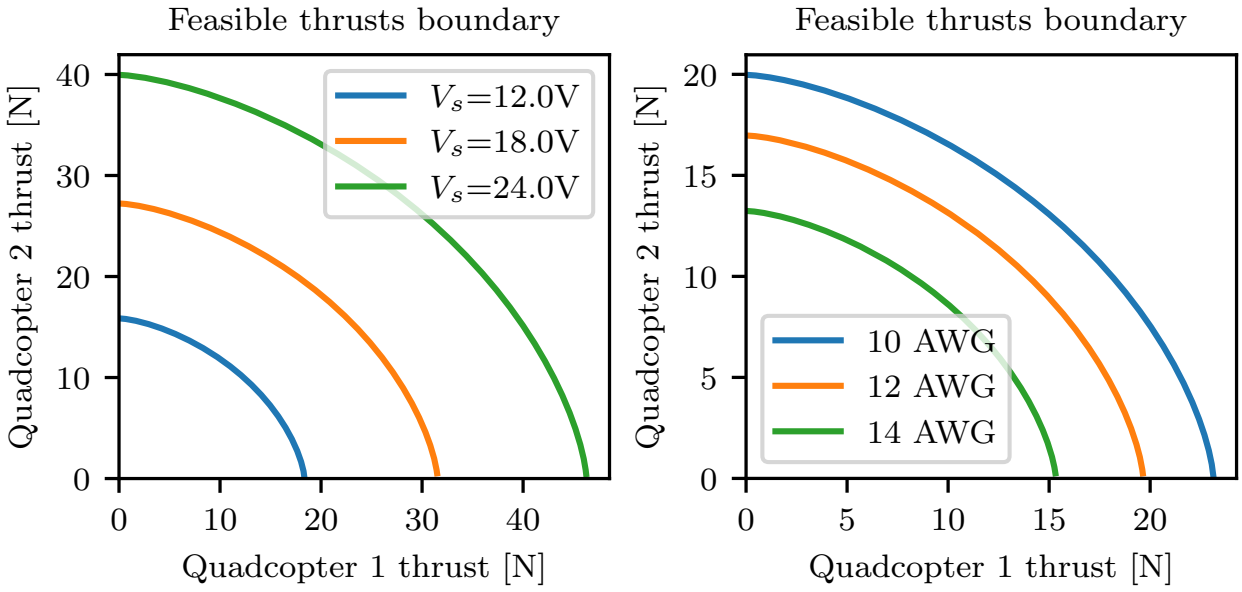

Figure 2.5: Maximum feasible thrust combinations for two quadcopters. (Left:) Different colored lines represent different source voltages V_s. The boundary becomes larger as the source voltage is increased. Specifically, the dependence is $V_s^{4/3}$. (Right:) Different colored lines represent different wire resistances. The boundary becomes larger as wire resistance per unit length ρ is decreased. Specifically, the dependence is $\rho^{-2/3}$.

Feasible thrust boundary vs. source voltage

We study the possible combinations of maximum thrusts that two tethered quadcopters can produce for various source voltages. The plot of these boundaries can be seen in Figure 2.5 (Left). The boundary is pushed outwards with increasing source voltage as $V_s^{4/3}$, see (2.13), because the resistive losses are reduced on increasing the source voltage which allows for higher power consumption before reaching the fundamental limit.

Feasible thrust boundary vs. wire size

The values of mass and resistance per unit length for different wire gauges are manufacturer dependent and are not explicitly known *a priori*. However, for a given manufacturer, we can measure the resistance and mass. With decreasing wire gauge, the mass of the tether decreases, and the resistance increases.

For the analysis in this subsection, we assume the resistance per unit length ρ of each section of the tether is the same. We also assume that the length of each tether section is fixed to a particular value. The plot of the feasible thrust boundaries for different wire gauges can be seen in Figure 2.5 (Right). The boundary is pushed outwards with decreasing

	End effector setpoint [m]	$(10, 5)$	$(20, 10)$	$(30, 15)$
	V_s [V]	18.0	36.0	54.0
One quadcopter	Optimal tether length [m]	12.87	26.08	39.13
	Minimum power [W]	**415.9**	**851.4**	**1459.6**
Two quadcopters	Optimal fraction	0.55	0.65	0.65
	Optimal intermediate setpoint [m]	$(6.26, 1.03)$	$(14.34, 3.27)$	$(21.21, 5.27)$
	Minimum power [W]	**456.0**	**736.3**	**1083.0**

Table 2.2: Optimized power consumption comparison for one tethered quadcopter vs. two tethered quadcopter systems. The final quadcopter position, tether type (ρ, λ), source voltage V_s, total tether length L are common for the two cases.

wire resistance per unit length as $\rho^{-2/3}$, see (2.13), because the resistive losses are reduced which allows for higher power consumption before reaching the fundamental limit. There is no dependence on the mass per unit length of the tether because we are studying the behavior with respect to the thrust of the quadcopters.

2.4 Horizontal Reach Power Comparison

In this section, we analyze the horizontal reach of the tethered quadcopter system for two cases: (i) One tethered quadcopter, and (ii) Two tethered quadcopters. The performance metric is the power that needs to be supplied for the system at hover, with the final (end effector) quadcopter in the tether series being at a specific desired position.

Catenary forces and the quadcopter thrust are computed as described in Section 2.2. Although adding a second quadcopter to a single tethered quadcopter system requires supporting its additional mass, the weight and tension of the tether getting distributed between the two quadcopters could result in a reduction of total power – this is because the power consumption P is dependent on the 1.5th power of the thrust $f^{3/2}$.

The approach to compare the total power consumption for the two cases is as follows:

1. Fix the tether type (mass per unit length λ and resistance per unit length ρ) and the source voltage and assume all quadcopters on the tether are identical.

2. Choose a desired end effector setpoint – the horizontal and vertical distance from the tether anchor which is at the power supply. Note the end effector setpoint for the one quadcopter case is given as (d_1, h_1) and for two quadcopters it is $(d_1{+}d_2, h_1{+}h_2)$, where d_1, h_1, d_2, h_2 are as shown in Figure 2.2.

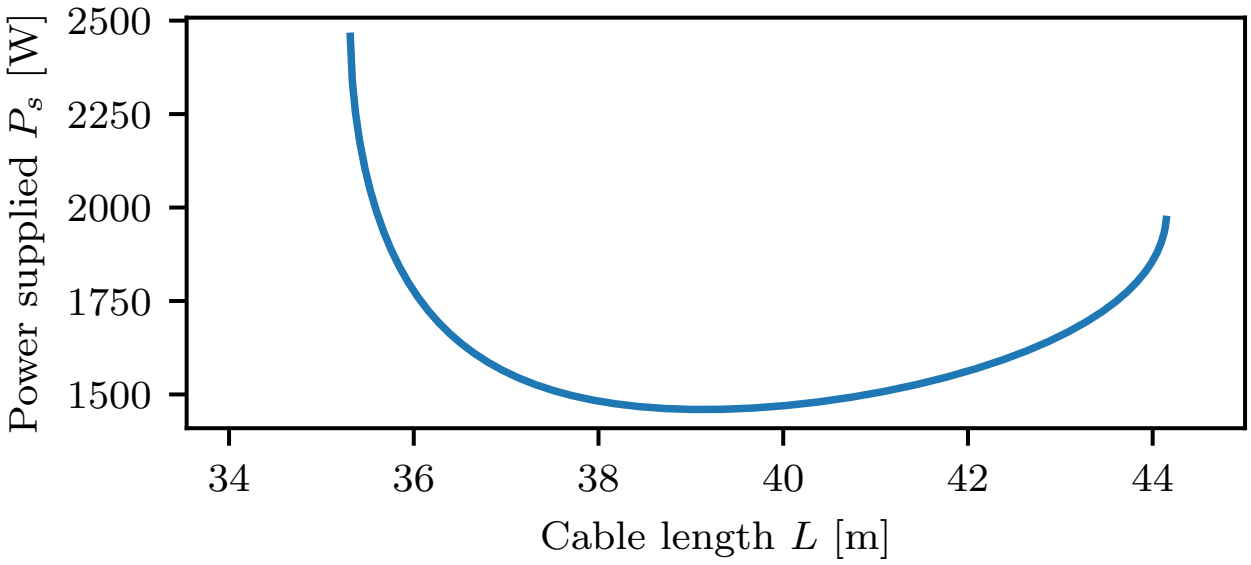

Figure 2.6: A plot of required power to be supplied to a single tethered quadcopter to hover at $(30, 15)$ m vs. tether length.

3. Consider the one tethered quadcopter case and choose an optimal tether length that minimizes the power to be supplied.

4. With the computed optimal length as the total tether length, add a second (intermediate) quadcopter and minimize power with respect to the following parameters: (i) intermediate quadcopter setpoint (from the power supply), (ii) fraction of the tether length between the power supply and intermediate quadcopter.

5. Compare the optimized power consumption values for the two cases.

Note that the power supply, the intermediate quadcopter, and the end effector quadcopter must all be in the same vertical plane, since any deviations of the intermediate quadcopter perpendicular to the vertical plane will increase the tension in that direction, leading to a higher thrust and power consumption for the intermediate quadcopter. Therefore, this is a 2D problem.

In all the problems in this analysis, we assume that the quadcopter mass is 0.7 kg, and the tether we use is 12 AWG for which $\lambda = 0.095\,\mathrm{kg\,m^{-1}}$ and $\rho = 0.0166\,\Omega\,\mathrm{m^{-1}}$. The power constant is experimentally determined to be $c_p = 4.5\,\mathrm{W/N^{\frac{3}{2}}}$.

Results for three end effector setpoints – $\{(10, 5), (20, 10), (30, 15)\}$ m are summarized in Table 2.2. The setpoints are chosen to cover a wide range of tether lengths. In the first case, the horizontal reach and tether weight is relatively low, making the one quadcopter tether system more power efficient than the two quadcopter tether system. In the second case, we

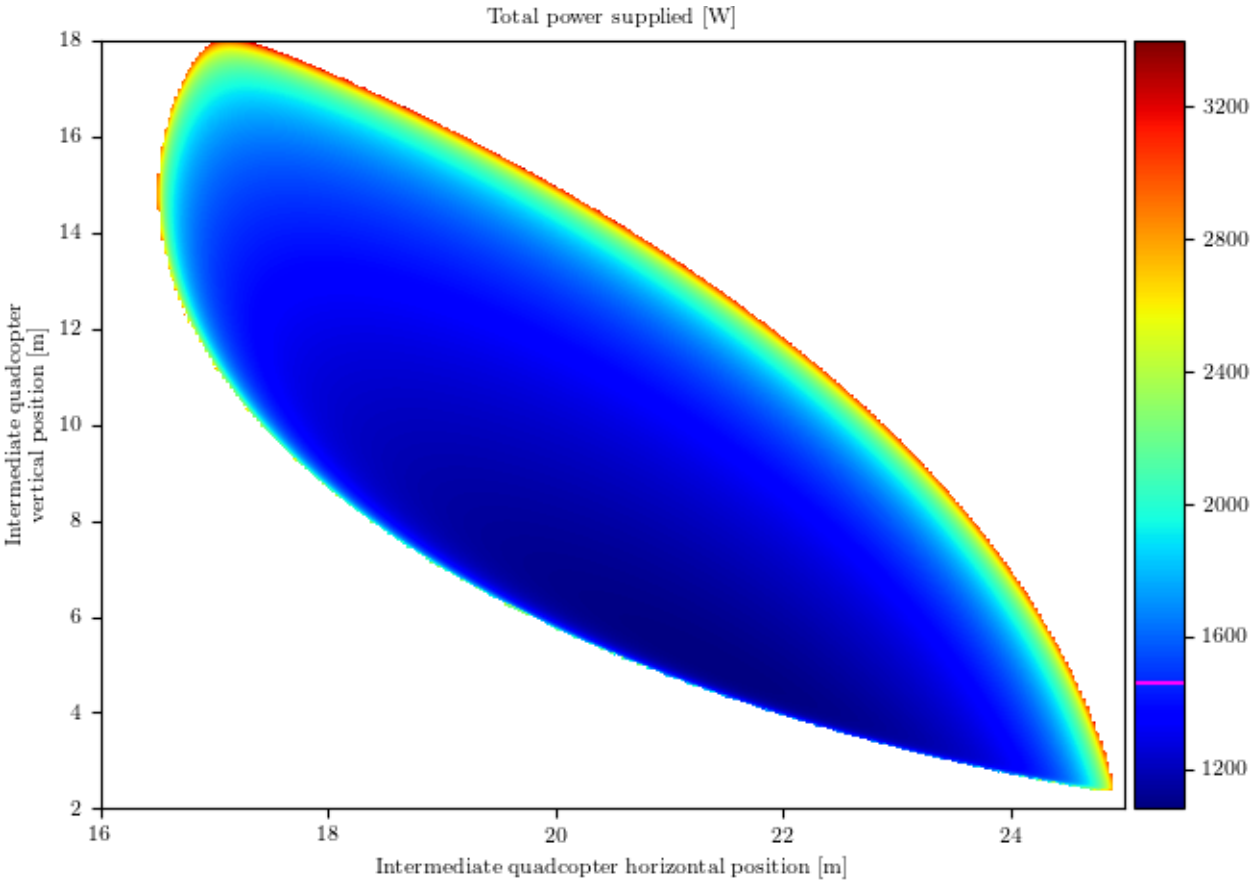

Figure 2.7: A plot of total power to be supplied to a two quadcopter tethered system vs. intermediate quadcopter horizontal and vertical setpoint. The end effector quadcopter is taken to be at $(30, 15)$ m. The plot is for the optimized fraction of tether length. Pink colored line on the colorbar shows optimized power consumption for the one quadcopter system for the same end effector setpoint.

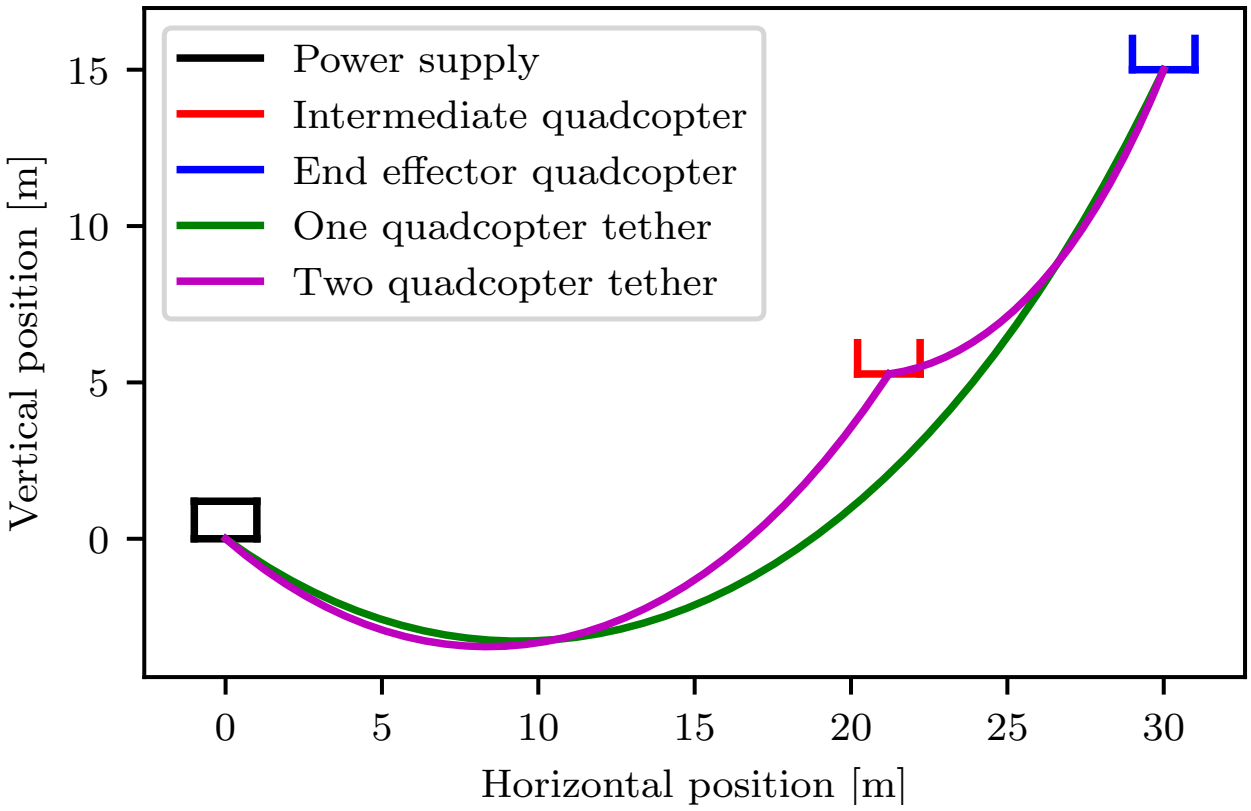

Figure 2.8: Sketch comparing one tethered quadcopter and two tethered quadcopters for end effector setpoint of $(30, 15)$ m. The two quadcopter system consumes lesser total power than one quadcopter.

require a higher horizontal reach increasing the catenary force on the end effector quadcopter. Adding an intermediate quadcopter reduces the total power consumption slightly (by 13.5%).

For the third case, the system requires a long horizontal reach and needs to lift a heavy tether (~ 4 kg). Adding the intermediate quadcopter results in the load distributed among the two quadcopters. This results in 26% lesser total power consumption for the two quadcopter system as compared to the one quadcopter system. Adding an intermediate quadcopter for such high tether lengths also frees up some thrust capacity for the end effector quadcopter, making it more maneuverable and agile. In applications such as firefighting, higher agility could be very useful in controlling the water outlet precisely and moving it rapidly.

A visual comparison of the one quadcopter and two quadcopter systems along with the tether shapes for the case with end effector setpoint $(30, 15)$ m is shown in Figure 2.8.

For end effector setpoint of $(30, 15)$ m, the plot of power consumption of one quadcopter

Figure 2.9: Snapshots of a grasping attempt using a single tethered quadrotor (setup (i)) over an obstacle – this ends up crashing the quadcopter

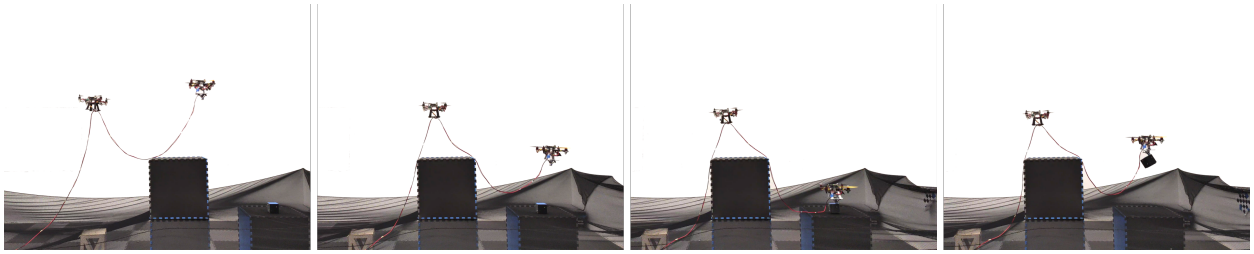

Figure 2.10: Snapshots of two quadcopters connected by single tether (setup (ii)) grasping over an obstacle

Figure 2.11: Experimental demonstrations of tethered drones for grasping over obstacles

tethered system with respect to the tether length is shown in Figure 2.6. We take the point with the minimum power consumption for step (3) in the approach. Note that a minimum always exists because for low tether lengths, the tension due to catenary force is high, and at high tether lengths, the weight of the tether is high – both resulting in higher power consumption. The plot of total power consumption of the two quadcopter tethered system with respect to the intermediate quadcopter setpoint (for the optimized fraction of tether length) is shown in Figure 2.7. Using a similar argument as for the one quadcopter system, we claim that there exists a minimum value of total power consumption at some optimal value of the intermediate quadcopter setpoint and the fraction of tether length between the power supply and intermediate quadcopter.

2.5 Experimental Demonstrations

In this section, we present experiments demonstrating potential applications for two quadcopters powered using a single tether. A two quadcopter system has the advantages of a single tethered quadcopter, such as extended flight time, and a steady power supply, while also increasing maneuverability in the horizontal direction, especially over difficult/unknown terrains. In the rest of the section, we present two experiments, comparing the following setups,

1. a single tethered quadcopter.
2. a two quadcopter system powered by a single tether

Passing Through Windows

In this experiment, we consider a window passing example with tethered quadcopters as shown in Figure 2.1. In setup *(ii)*, the first quadcopter (left) supports the second quadcopter (right) exploring on the other side of the window. Similar exploration using single tethered quadcopter are not always feasible in cluttered environments, as the obstacles could interfere with the tether.

Grasping Over Obstacles

A two quadcopter tethered system can act as an *aerial series-manipulator* in cluttered environments, as shown in Figure 2.10. We do a grasping experiment using the two setups, to grasp an object located on the other side of an obstacle, in the vertical plane as shown in Figure 2.11. Waypoints are provided to the quadcopters to reach over the obstacles and grasp the object. An electromagnet is used as the gripper for grasping the metallic object. In setup *(i)*, see Figure 2.9, a single tethered quadcopter attempts to grasp the object, however, is unable to reach the grasp location due to the limitation of the quadcopter to drag the tether over obstacles. In setup *(ii)*, the first quadcopter (left) acts an intermediate joint for the second drone (right) to help grasp the object over the obstacle as shown in Figure 2.10. A video demonstrating the experiments is provided in the media attachment.

2.6 Conclusion and Future Work

In this chapter, we have presented an analysis for a tethered multiple-quadcopter system to estimate the electrical power consumption by the quadcopters and the power supply required to deliver the desired power to the quadcopters. The analysis includes various mechanical, aerodynamic, and electrical parameters of the tethered multiple-quadcopter system. We analyzed the power supply requirement for multiple tethered quadcopters with respect to the quadcopter thrusts. We found that there exists a thrust boundary that cannot be

exceeded because of fundamental electrical limitations. We found that the thrust boundary can be pushed outward by increasing the supply voltage or decreasing the tether resistance which can be helpful to designers.

We compared the power requirements for various end effector setpoints for one tethered quadcopter and a series of two tethered quadcopters. As the end effector setpoint is pushed further from the power supply (the anchor point), it was found that the optimal two quadcopter system consumes lesser total power than the optimal one quadcopter system. Adding an intermediate quadcopter also frees up thrust capacity on the end effector quadcopter increasing its maneuverability and agility.

Lastly, we show a system with two experiments using two quadcopter tethered system and demonstrate better horizontal reachability in cluttered environments as compared to the corresponding one quadcopter system. An additional advantage offered by this system is performing tasks that need quadcopters to operate in proximity such as picking fruits or cleaning a high-rise building.

An extension to this work is to design a multiple quadcopter tether system to perform manipulation tasks in cluttered environments. Using the power analysis allows users to specify the power supply and tether sizes optimally for the specific system.

Chapter 3

Staging energy sources to extend flight time of a multirotor UAV

Energy sources such as batteries do not decrease in mass after consumption, unlike combustion fuels. We present the concept of staging energy sources, i.e. consuming energy in stages and ejecting used stages, to progressively reduce the mass of aerial vehicles in-flight which reduces power consumption, and consequently increases flight time. A flight time vs. energy storage mass analysis is presented to show the endurance benefit of staging to multirotors. We consider two specific problems in discrete staging – optimal order of staging given a certain number of energy sources, and optimal partitioning of a given energy storage mass budget into a given number of stages. We then derive results for a continuously staged case of an internal combustion engine driving propellers. Notably, we show that a multirotor powered by internal combustion has an upper limit on achievable flight time independent of the available fuel mass. Lastly, we validate the analysis with flight experiments[1] on a custom two-stage battery-powered quadcopter. This quadcopter can eject a battery stage after consumption in-flight using a custom-designed mechanism, and continue hovering using the next stage. The experimental flight times match well with those predicted from the analysis for our vehicle. We achieve a 19% increase in flight time using the batteries in two stages as compared to a single stage.

The material in this chapter is based on the following previously published work.

- Karan P Jain et al. "Staging energy sources to extend flight time of a multirotor UAV". in: *2020 IEEE/RSJ International Conference on Intelligent Robots and Systems (IROS)*. IEEE. 2020, pp. 1132–1139

[1]The explanation and experimental validation video can be found here: `https://youtu.be/CUjPCRUO66U`

3.1 Introduction

The ability to fly as a compact machine has given rise to the use of unmanned aerial vehicles (UAVs) in several applications such as surveillance, mapping, delivery, and search and rescue missions [61, 10, 8]. Multirotor UAVs are also being considered for exploration of other worlds [62, 41]. A fundamental limitation of most UAVs is their flight time – they must land when their energy source is depleted. There is a growing demand for higher endurance and range in UAVs with their increasing usage in research and industrial settings.

Innovative approaches have been explored to increase the endurance and range of UAVs. Broadly, we can classify the approaches into two types: assisted and unassisted. Assisted methods typically involve the use of fixed stations or mobile vehicles for the replacement or the charging of energy sources. Battery swapping at a fixed ground station has been presented in [22, 23], and on a mobile ground base has been shown in [24]. Flying replacement batteries to a multirotor using other multirotors is discussed in [37].

Unassisted methods typically involve increasing mechanical or electrical efficiency or the use of optimization-based methods over objectives such as flight time or range. One such approach is exploiting the efficiency of a fixed-wing and hovering ability of a multirotor by converting them into a hybrid aerial vehicle [18]. Manipulation of vehicle structure by tilting rotors to increase efficiency is shown in [17]. An online strategy for optimizing efficiency by altering flight parameters (e.g. speed) over a trajectory is presented in [20]. The analysis of a solar-powered UAV, which can potentially fly for a long time, is shown in [21]. However, such a vehicle requires a large wing-span, is sensitive to weather conditions, and is not suitable for indoor settings.

An unassisted approach which is largely unexplored for UAVs is the staging of energy sources. A possibility of ejecting depleted energy sources is mentioned in [63], which presents a modular drone consisting of drone cells, which can potentially be staged. Energy sources such as batteries are used widely on UAVs, primarily because they are easy to recharge and reuse, and do not produce exhaust, making them a good candidate for indoor settings. Electric powertrains also have fewer moving parts, making maintenance easy. Batteries, however, have a clear disadvantage as opposed to combustion fuels, in the sense that the consumed portion still remains as a mass on the vehicle. This has a significant impact because in the case of electric vehicles, battery mass accounts for a notable fraction of the total mass. We draw inspiration from multi-stage rockets [64, 65, 66] which are designed for missions that would otherwise require a much larger single-stage rocket. We note that rocket staging is about discretely staging the structure, not the fuel.

The contribution of this chapter is to analyze, explore, and experimentally validate this energy staging concept for multirotors. The design space for multirotors with various discrete staging configurations is explored by analyzing the effect on flight time with respect to the energy storage mass. Flight time performance is also analyzed for a continuously staged source – an internal combustion engine driving propellers. Using energy sources in multiple stages as opposed to a single stage is shown to benefit flight time both analytically and experimentally. Lastly, the environmental impacts and use cases of staging are assessed to

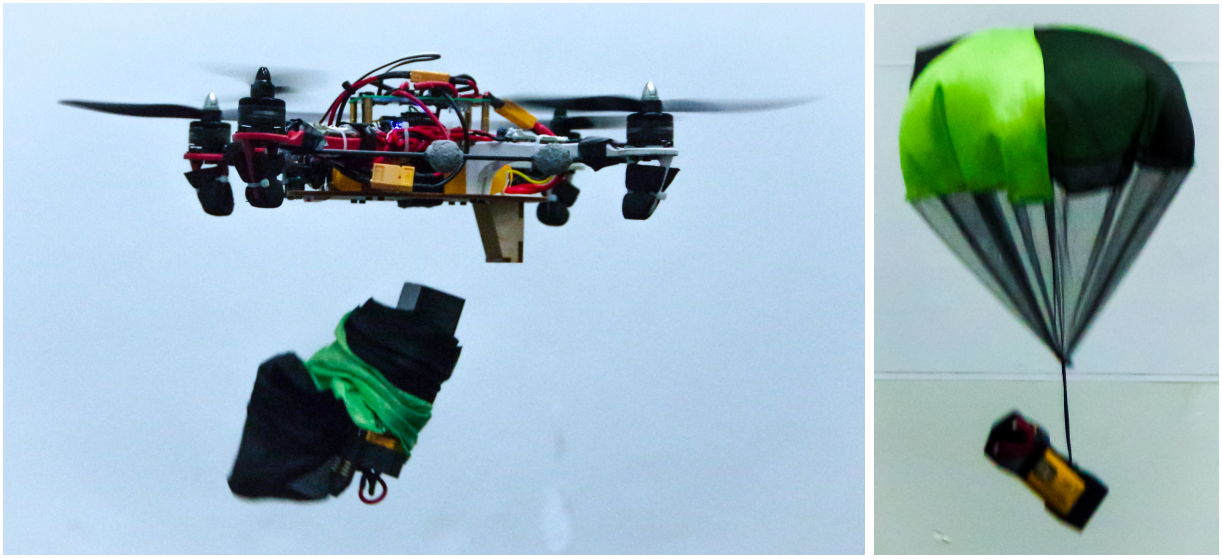

Figure 3.1: (Left:) Quadcopter dropping its first stage after use. A parachute is attached to the ejected stage to avoid damage to the battery or the surroundings. (Right:) Ejected stage with the deployed parachute.

realize specialized areas where benefits of staging can be exploited, for example in industrial settings, emergency situations, or for interplanetary exploration missions.

3.2 Staging Analysis

In this section, we present an analysis of how using an energy source in stages is beneficial for the flight time performance of hovering multirotors. A brief review is first given of the actuator disk model for power consumption of a propeller; this model is then applied to quantify the gain in flight time by discarding the used energy storage stages in-flight. This is then compared to a case where an infinite number of stages exist – where the energy source is the fuel combusted (and then exhausted) in an engine that drives rotors.

Rotor power consumption and flight time

For an actuator disk model of a propeller that is not translating in the ambient air, the aerodynamic power p_{aero} required may be computed [16] as

$$p_{\text{aero}} = \frac{f^{\frac{3}{2}}}{\sqrt{2\rho A_p}} \tag{3.1}$$

where f is the thrust produced, ρ is the density of the air, and A_p is the area swept by the rotor. This derivation assumes that the flow is inviscid, incompressible, and follows from applying conservation of mass and energy to a control volume containing the propeller. Note that translating propellers have more complex relationships, see e.g. [20].

The actual power drawn from the energy source to the system will include additional losses, including aerodynamic losses which may be captured in a propeller's figure of merit [16] as well as losses in transmission of power to the propeller (e.g. gears or electric resistance). We make the simplifying assumption that these losses are all proportional to the power drawn, so that the actual power consumption of a propeller i producing thrust f_i may be captured by

$$p_i = c_p f_i^{\frac{3}{2}} \tag{3.2}$$

where the constant c_p is a function of the propeller size, ambient air density, propeller figure of merit, and powertrain efficiency. Note that a similar relationship can be derived from the mechanical power required to drive the propeller shaft under the assumption that the thrust is proportional to the rotational speed of the propeller squared, and that the propeller torque is proportional to the propeller thrust [17].

For a symmetric quadcopter of mass m to hover, each propeller must produce a force equal to a quarter of the vehicle's weight, and the total power consumption p is

$$p = \sum_i p_i = \frac{1}{2} c_p g^{\frac{3}{2}} m^{\frac{3}{2}} \tag{3.3}$$

where the local acceleration due to gravity is given by g. Let e_b be the specific energy of the energy source, so the energy budget E for a given energy source mass m_E is $E = e_b m_E$. Then, at constant total mass m, a vehicle with energy source E can hover for a flight time of

$$T_f = \frac{E}{p} = e_b c_T m_E m^{-\frac{3}{2}} \tag{3.4}$$

where $c_T = 2c_p^{-1} g^{-\frac{3}{2}}$ is a vehicle-specific constant, and is specifically independent of the vehicle mass. In all the subsequent analysis, we assume that all energy storage stages have the same specific-energy. We note that the energy content need not be strictly proportional to the mass due to additional components such as packaging and connectors. However, for many commercial batteries, it is shown in [67] that this simplifying assumption is reasonable.

Discrete energy storage stages

A primary disadvantage of batteries for energy storage is that the storage mass does not decrease as the chemical energy is depleted (unlike, for example, a combustion engine). From (3.3), it is clear that the power consumption would be reduced if the total mass of the vehicle could be reduced, for example by ejecting parts of the battery as it is depleted.

For a vehicle with N battery stages, where the ith battery has mass m_i, the total mass of the vehicle at stage i is given by $m_d + \sum_{j=i}^{N} m_j$, where m_d is the dry mass of the vehicle,

i.e. mass of all components of the vehicle excluding energy storage (but including payload, etc.). In particular, at stage i, the mass $\sum_{j=1}^{i-1} m_j$ has been ejected. The flight time for the ith stage can be computed from (3.4) as

$$T_{f,i} = e_b c_T m_i \left(m_d + \sum_{j=i}^{N} m_j \right)^{-\frac{3}{2}} \tag{3.5}$$

with total flight time over all stages

$$T_f = \sum_i T_{f,i} = e_b c_T \sum_{i=1}^{N} m_i \left(m_d + \sum_{j=i}^{N} m_j \right)^{-\frac{3}{2}}. \tag{3.6}$$

This equation shows that achievable flight time is directly proportional to the specific energy e_b and depends on the stage masses m_i in a nonlinear fashion.

Equal staging

For a vehicle with dry mass m_d, and total energy storage mass m_b split equally over N stages, the flight time can be computed from (3.6) as

$$T_f = \frac{e_b \, c_T \, m_b}{N} \sum_{i=1}^{N} \left(m_d + \frac{i}{N} m_b \right)^{-\frac{3}{2}}. \tag{3.7}$$

Fig. 3.2 shows plots of (normalized) flight time vs. the ratio of total energy storage mass (m_b) to total initial vehicle mass ($m_d + m_b$), for various number of stages. The case of equal staging is plotted using solid curves. The normalization factor is the maximum achievable flight time for an infinitely-staged vehicle as derived in Section 3.2. Since the figure is normalized, it is valid for a multirotor with a different powertrain efficiency, or one flying on another planet with a different surface gravity and air density.

The plots in Fig. 3.2 and the results from equal staging can be used in the following ways. For a given energy storage mass, one can fix the x-axis value, and decide the number of stages they want based on their flight time requirements. On the other hand, the choice for designers might be flight time for their vehicle. In that case, they can fix the y-axis value, and then choose the number of stages based on the mass constraints.

Optimal staging order

We consider the case of having a series of N energy storage stages, of known, fixed but different masses, with the only design variable being the order in which to stage them.

Theorem 3.2.1. *The optimal flight time is achieved by staging in order of decreasing mass, so that the heaviest stage is depleted and discarded first.*

Proof. The proof follows by contradiction. Assume that an optimal staging sequence is given by $\mathcal{S}^* = \{m_1, m_2, \ldots, m_N\}$ where for some value $k \in \{1, \ldots, N\}$ the stage k is lighter than the following stage $k+1$, i.e. $m_k < m_{k+1}$. Let T^* represent the total flight time, computed with (3.6) for this sequence.

Let $\bar{\mathcal{S}} := \{m_1, \ldots, m_{k-1}, m_{k+1}, m_k, m_{k+2}, \ldots, m_N\}$ represent a modified staging order, which only interchanges the order of the original kth and $(k+1)$th stage. Let $\bar{T}$ represent the associated total flight time. We note that flight times from the first $k-1$ and the stages continuing after $k+2$ are identical. We denote the short-hand $M := m_d + \sum_{i=k+2}^{N} m_i$ as the total mass of the vehicle after discarding the first $(k+1)$ stages. Then the difference in flight times is

$$\begin{aligned}\frac{T^* - \bar{T}}{e_b c_T} =& \frac{m_k}{(M + m_k + m_{k+1})^{\frac{3}{2}}} + \frac{m_{k+1}}{(M + m_{k+1})^{\frac{3}{2}}} \\ &- \frac{m_{k+1}}{(M + m_k + m_{k+1})^{\frac{3}{2}}} - \frac{m_k}{(M + m_k)^{\frac{3}{2}}} \qquad (3.8)\\ =& \left(m_k - m_{k+1}\right) q\left(m_k + m_{k+1}\right) \\ &+ m_{k+1} q\left(m_{k+1}\right) - m_k q\left(m_k\right) \qquad (3.9)\end{aligned}$$

where we define $q(m) := (M+m)^{-\frac{3}{2}}$ for convenience. We note that

$$\frac{\partial}{\partial m} q(m) =: q'(m) = -\tfrac{3}{2}(M+m)^{-\frac{5}{2}} < 0, \qquad (3.10)$$

$$\frac{\partial^2}{\partial m^2} q(m) = \tfrac{15}{4}(M+m)^{-\frac{7}{2}} > 0. \qquad (3.11)$$

We use Lagrange's mean value theorem to relate the average slope of $q(m)$ between points $\{m_k, m_{k+1}\}$ with the average slope between points $\{m_{k+1}, m_k + m_{k+1}\}$ as

$$\begin{aligned}\frac{q\left(m_{k+1}\right) - q\left(m_k\right)}{m_{k+1} - m_k} &< q'\left(m_{k+1}\right) \\ &< \frac{q\left(m_k + m_{k+1}\right) - q\left(m_{k+1}\right)}{\left(m_k + m_{k+1}\right) - m_{k+1}}.\end{aligned} \qquad (3.12)$$

Rearranging this, and using $m_{k+1} > m_k > 0$ gives

$$\begin{aligned}&\left(m_k - m_{k+1}\right) q\left(m_k + m_{k+1}\right) \\ &+ m_{k+1} q\left(m_{k+1}\right) - m_k q\left(m_k\right) < 0.\end{aligned} \qquad (3.13)$$

Substituting this in (3.9) gives $\bar{T} > T^*$. However, this contradicts the assumption that T^* is the optimal flight time. Thus, S^* cannot be an optimal staging sequence, and the optimal staging sequence has $m_1 \geq m_2 \geq \ldots \geq m_N$, proceeding from the heaviest stage first to lightest stage last. ■

Optimal mass partitioning

Given a dry mass m_d, an energy storage mass budget m_b, and a total number of stages N to be used, it is of interest to find the optimal stage masses that add up to m_b, to maximize the flight time.

This is equivalent to maximizing T_f in (3.6) over the decision variables m_i, under the inequality constraints $m_i > 0$ and the equality constraint $\sum_i m_i = m_b$.

We define new decision variables, $x_i = m_d + \sum_{j=i}^{N} m_j$, so that $m_i = x_i - x_{i+1}$. Substituting this in (3.6), the flight time can be written in terms of the decision variables as

$$J = \sum_{i=1}^{N} \frac{x_i - x_{i+1}}{x_i^{\frac{3}{2}}} \tag{3.14}$$

where J is now our objective function to be maximized. The constants e_b and c_T are dropped because they are scaling factors which do not affect the decision variables.

This can be formulated as a constrained optimization problem as follows,

$$\begin{aligned} \max_{x_1, x_2, \cdots, x_{N+1}} \quad & J \\ \text{s.t.} \quad & x_1 = m_d + m_b, \\ & x_{N+1} = m_d, \\ & x_{i+1} < x_i \quad \text{for} \quad i = 1, 2, \cdots, N. \end{aligned} \tag{3.15}$$

Solving the above problem using the KKT conditions [68], we obtain a solution in the form of simultaneous nonlinear equations shown below,

$$\begin{aligned} \frac{1}{x_i^{\frac{3}{2}}} + \frac{2}{x_{i-1}^{\frac{3}{2}}} - \frac{3x_{i+1}}{x_i^{\frac{5}{2}}} = 0 \quad \text{for} \quad i = 2, 3, \cdots, N, \\ x_1 = m_d + m_b, \\ x_{N+1} = m_d. \end{aligned} \tag{3.16}$$

Even for the simplest case of $N = 2$, this requires the roots of a fifth-degree polynomial, for which no closed-form expression exists. Nonetheless, the simultaneous equations can be solved numerically. Plots for a few sample N values are shown in Fig. 3.2 as dashed lines to compare with the equally staged case (solid lines). For $N = 2$, 3, 4, and 5, the predicted maximum achievable flight time is higher by 10.5%, 16.9%, 21.1%, and 24.0% respectively for optimal staging as compared to equal staging.

From the discrete staging analysis, we conclude that staging can be beneficial in the following ways. First, for the same amount of energy, we can increase the flight time as compared to a single-stage vehicle. This is to be expected because as the multi-stage vehicle ejects stages, its mass and consequently power consumption is reduced. Since the total energy is the same in both cases, the flight time of the multi-stage vehicle is higher. Second, to achieve the same flight time, a multi-stage vehicle will be lighter and more compact, by a similar argument, which could make it safer. Third, in the case of any multi-stage UAV, the mass and moment of inertia reduces with every stage ejected, increasing its agility.

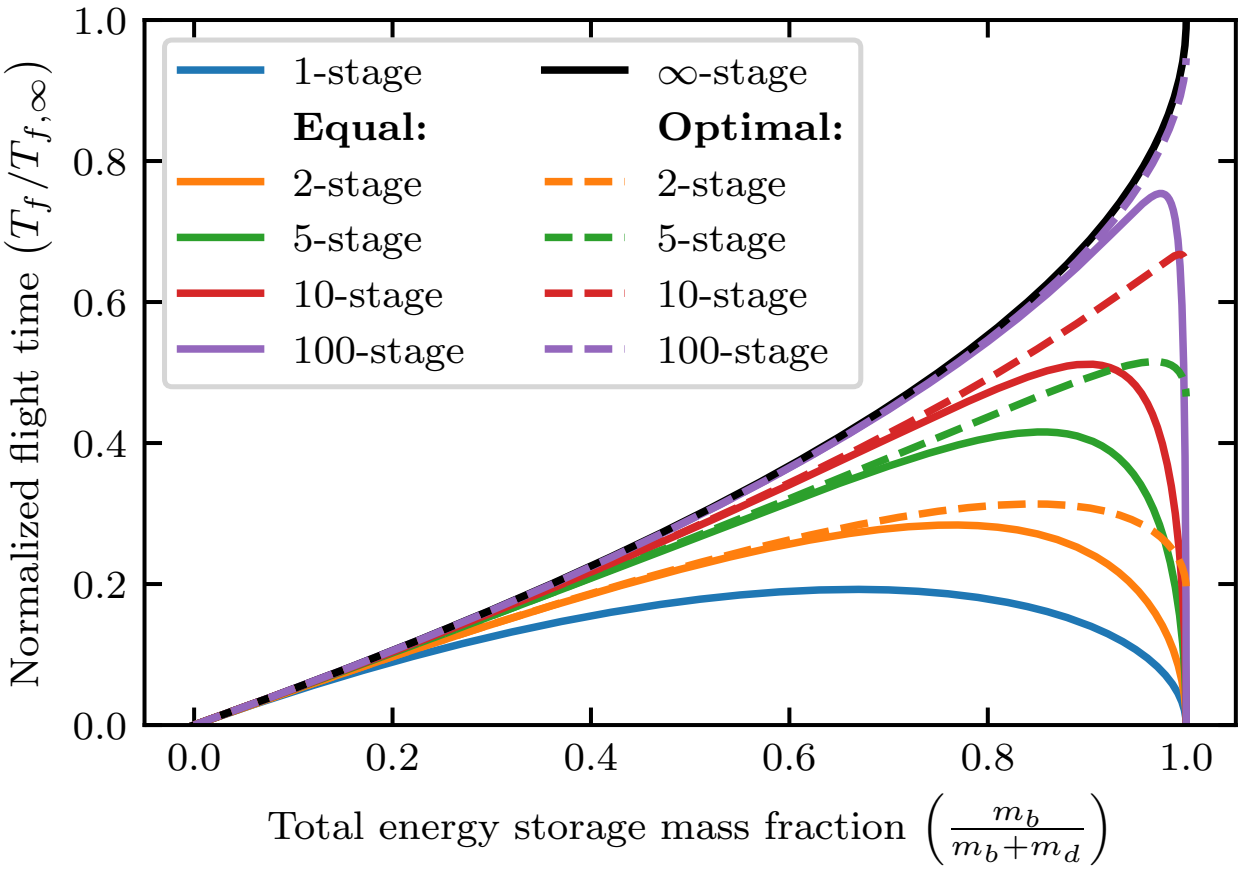

Figure 3.2: Effect of total energy storage mass on hovering flight time for various number of stages. Dry mass and total energy storage mass are respectively denoted by m_d and m_b. Note that this plot is valid only for $m_d > 0$, and the energy storage fraction reaches 1.0 in the limit $m_b \to \infty$. Solid lines are for equally staged energy sources (see Section 3.2), whereas dashed lines are for optimally staged (see Section 3.2). The flight times are normalized with respect to that for continuously staged case with infinite energy storage mass $T_{f,\infty}$ (see (3.19)). Normalization makes this plot valid for any multirotor flying in any environment.

Continuous staging

A multirotor, with its propellers driven by a combustion engine where the combustion products are exhausted, can be described as a limiting case of the above, with continuous staging.

The remaining mass of the energy storage m_E will evolve at a rate proportional to the power consumption,

$$\dot{m}_E = -\frac{1}{e_b}\dot{E} = -\frac{c_p g^{\frac{3}{2}}}{2e_b}\left(m_d + m_E\right)^{\frac{3}{2}} \tag{3.17}$$

where we've used (3.3) and again assumed a symmetric quadcopter at hover. Solving this, and substituting $m_E\left(0\right) = m_b$, and $m_E\left(T_f\right) = 0$ gives the total flight time T_f as

$$T_f = \frac{4e_b}{c_p g^{\frac{3}{2}}\sqrt{m_d}}\left(1 - \left(1 + \frac{m_b}{m_d}\right)^{-\frac{1}{2}}\right). \tag{3.18}$$

This flight time value can also be derived by taking the limit as $N \to \infty$ in (3.7).

Note that the flight time is, as may be expected, monotonically increasing in the initial fuel mass m_b. However, there exists a natural upper limit to achievable flight time, even for arbitrarily large quantities of fuel:

$$T_f < T_{f,\infty} = \lim_{m_b \to \infty} T_f = \frac{4e_b}{c_p g^{\frac{3}{2}}\sqrt{m_d}} = \frac{2e_b c_T}{\sqrt{m_d}}. \tag{3.19}$$

This reveals a fundamental limit of rotor propulsion. Even under the best case of continuous staging, achievable flight time has an upper limit no matter how much fuel is used, for a specific vehicle (fixed c_p and m_d), energy source (fixed e_b) and environment (fixed g). In practice, other constraints would act to limit achievable performance, e.g. thrust and structural limitations.

We also note that as the dry mass is reduced, the flight time increases, with the limit $T_f \to \infty$ as $m_d \to 0$.

3.3 Experimental Hardware Design

In this section, we explain the design of the quadcopter used in our experiments, the battery staging mechanism, and the battery switching circuit.

Vehicle design

The quadcopter is designed to have enough payload capacity for carrying useful sensors such as surveillance cameras, or environmental sensors. Its dry mass is 565 g, and it can generate a maximum thrust of 27 N. Its arm length is 165 mm, and it uses four 203 mm diameter propellers. We stack a battery switching circuit on top of the quadcopter for staging. The quadcopter is powered by two batteries. The first-stage battery is placed at the bottom of the

quadcopter that can be ejected when depleted, and the second-stage battery is placed at the center of the quadcopter which always stays onboard. Copper plates mounted at the bottom serve as input leads from the first-stage battery. Fig. 3.1 shows a picture of the quadcopter. We use two types of batteries – a "heavy" 3S 2.2 Ah lithium polymer (LiPo) battery weighing 190 g, and a "light" 3S 1.5 Ah LiPo battery weighing 135 g. We use the heavy battery in both the first and second stages for experimental comparison between staged and unstaged cases. To verify the optimal order of staging, we use the heavy and light battery in the two possible permutations.

Staging mechanism

The staging mechanism is shown in Fig. 3.3. The mechanism is placed on the lower section of the quadcopter frame. In order for the first-stage battery to engage with the mechanism, we have an attachment on one end of the battery. This attachment has a bolt, and two spring-loaded contacts, which are electrically connected to the output leads of the first-stage battery. On the side of the quadcopter frame, a "detaching" motor is installed, which has a nut fixed on its shaft. Next to the motor are two copper plates that serve as input leads from the first-stage battery. The staging mechanism adds a total of 45 g mass to the quadcopter – 30 g to the first-stage battery and 15 g to the quadcopter frame. This corresponds to a mass increase of 8%.

To connect the first-stage battery, we engage the bolt from the battery with the nut on the motor shaft. This connects the spring-loaded contacts to the input leads. To disconnect the battery, we command the motor to unscrew the bolt. When the bolt is completely disengaged from the nut, the battery loses support and thus drops, and then softly lands using an attached parachute.

Battery switching circuit

The design of our battery switching circuit is inspired by [37]. Since our system is flying, we cannot afford to cut the power supply when switching from the first battery to the second battery. The two batteries need to be connected in parallel for some time to achieve this. We connect diodes in series with each of the batteries to avoid reverse currents due to the voltage difference between the batteries.

A normally closed relay is connected in series with the first battery. By opening the switch, we can draw power from the first battery even when it is at a lower voltage than the second battery. This is necessary to completely consume the first battery, before starting the use of the second battery. The relay coil is connected across the first battery input leads in series with a MOSFET. The gate terminal of the MOSFET is connected to a GPIO pin on the flight controller to control the relay. Fig. 3.4 shows a schematic diagram of the battery switching circuit. The circuit weighs 60 g. We note that this circuit is built on a prototype board and can potentially be made much lighter using smaller electronics on a PCB.

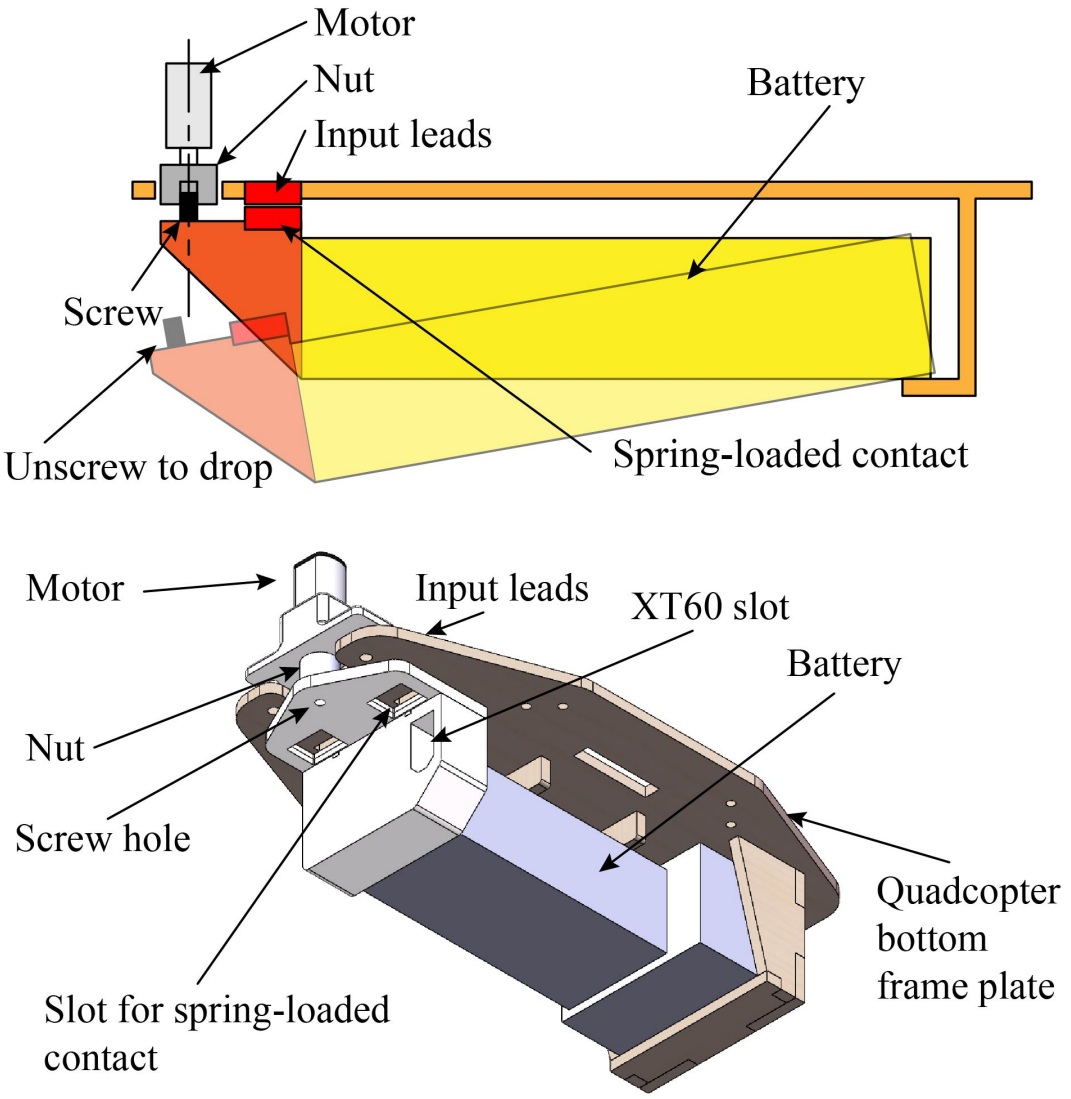

Figure 3.3: (Top:) Schematic of the battery-dropping mechanism. (Bottom:) CAD model of the mechanism.

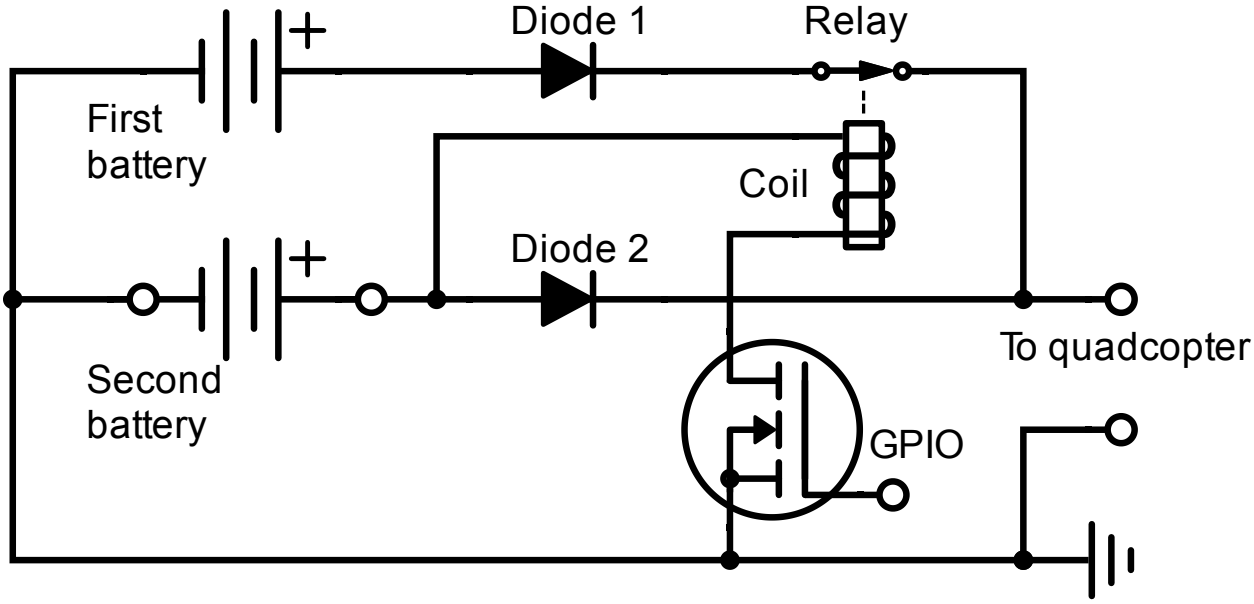

Figure 3.4: Schematic of the battery switching circuit.

3.4 Experimental Validation

We validate the staging analysis by first predicting the flight times for our quadcopter with and without staging. We then conduct hovering flight experiments for single-stage and two-stage cases. The flight time for the two-stage case is shown to be higher. The optimal order of staging is also validated using the heavy and light batteries in two different orders. All experimental flight times are also compared with the predictions from the analysis and are shown to match well, validating the analysis. An experiment with the quadcopter ejecting a stage while traversing a circular trajectory is also conducted to show that the effect on maneuvering is negligible. This can be seen in the video attachment.

Flight time prediction from analysis

We use the results from equal staging (Section 3.2) since we use the same type of battery (heavy) for both stages. The values of specific energy and c_T are determined empirically from flight experiments on the quadcopter, which respectively are $e_b = 130\,\mathrm{Wh\,kg^{-1}}$ and $c_T = 6.2 \times 10^{-3}\,\mathrm{kg^{\frac{3}{2}}\,W^{-1}}$. Using Eq. (3.7) with $m_b = 380\,\mathrm{g}$ and $m_d = 595\,\mathrm{g}$ (includes additional 30 g from the first-stage battery), we predict flight times of 19.1 min for the single-stage case, and 22.8 min for the two-stage case.

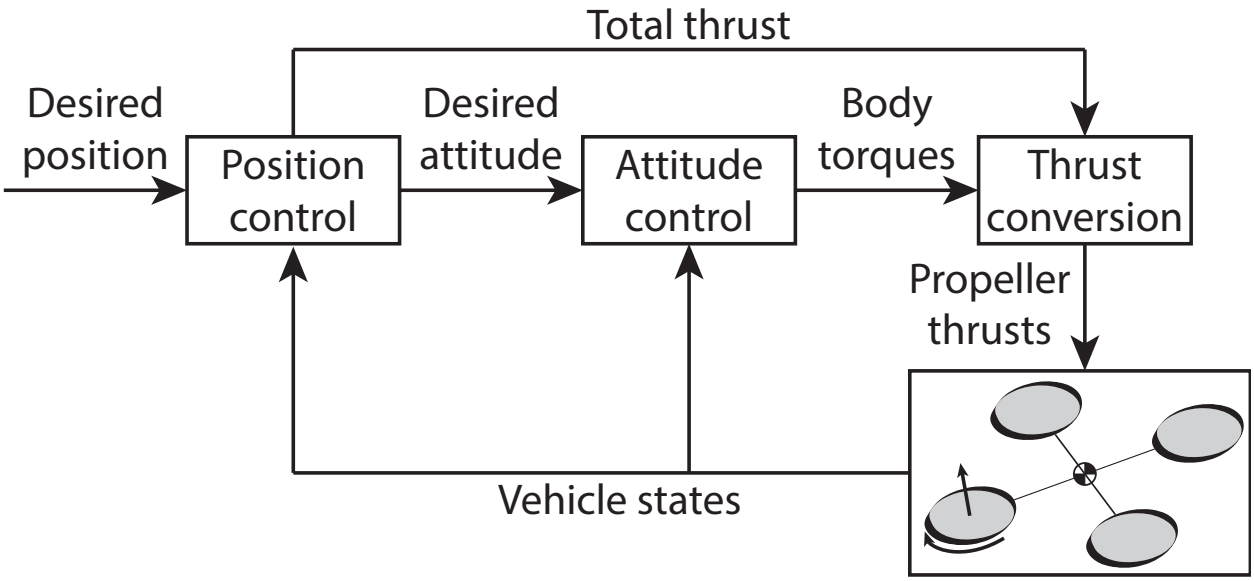

Figure 3.5: Block diagram of the quadcopter controller.

Experimental setup

The quadcopter used in our experiments is localized via sensor fusion of a motion capture system and an onboard rate gyroscope [38]. Experimental data from the motion capture system, voltage sensor, and the current sensor is logged via radio for post-processing. We control the quadcopter using a cascaded position and attitude controller shown in Fig. 3.5. The measured battery voltage is used to decide on commands for battery switching, stage ejection, and landing.

Demonstration

The benefit of staging batteries is demonstrated by conducting two types of experiments (shown in the video attachment): one without staging (single-stage), and the other with staging (two stages). We conduct three flight experiments for each type. All of our experiments consume the batteries from a fully charged state of 4.2 V per cell to a fully discharged state of 3.0 V per cell. For the 3 cell batteries that we use, the corresponding voltages are 12.6 V and 9.0 V.

In the single-stage experiments, the quadcopter hovers using the two batteries simultaneously until both the batteries are completely discharged. In the three single-stage experiments, the quadcopter hovered for an average time of 19.16 min, with a standard deviation of 0.18 min.

Figure 3.6: Sequence of images from the two-stage flight experiment. From left to right: (a) Quadcopter hovers using only first-stage battery. (b) First-stage battery is depleted. Quadcopter starts using second-stage battery. The detaching motor is simultaneously activated to disengage the bolt. First stage is about to fall. (c) First stage is ejected and falls towards the ground. (d) Quadcopter continues hovering using the second-stage battery, with reduced mass and power consumption. **Note:** We have not attached a parachute in this case to clearly show how the staging works. The first stage fall is broken softly by a net below the quadcopter. In real-life settings, it is advised to use some fall breaking mechanism to not damage the energy source or any property (for e.g. by using a parachute as shown in Fig. 3.1). All reported experimental flight times and plots use a parachute in the two-stage case.

In the two-stage experiments, the quadcopter initially hovers using the first battery. Once the first battery is discharged, the second battery is connected to the quadcopter by closing the relay in the switching circuit. The first stage is then detached by activating the detaching motor in the staging mechanism. Hovering continues until we completely consume the second battery. Fig. 3.6 shows a sequence of snapshots from the two-stage experiment. In the three two-stage experiments, the quadcopter hovered for an average time of 22.80 min, with a standard deviation of 0.17 min.

Validation of optimal order

We experimentally validate the optimal order of staging result from Section 3.2 by conducting flight experiments on the same quadcopter using the heavy and light batteries. These batteries had an experimentally determined specific energy of $e_b = 120\,\mathrm{Wh\,kg^{-1}}$.

Using (3.6) with same c_T as before, and $m_d = 595\,\mathrm{g}$, we predict flight times of 19.0 min with $m_1 = 135\,\mathrm{g}$ and $m_2 = 190\,\mathrm{g}$ (light battery on first-stage), and 19.3 min with $m_1 = 190\,\mathrm{g}$ and $m_2 = 135\,\mathrm{g}$ (heavy battery on first-stage). As expected from the analysis of optimal order, we get a higher flight time when the heavier battery is ejected first.

Three flight experiments were conducted for each order. We observed an average flight time of 19.00 min when the light battery was ejected first, with a standard deviation of 0.14 min. When the heavy battery was ejected first, the average flight time was 19.47 min,

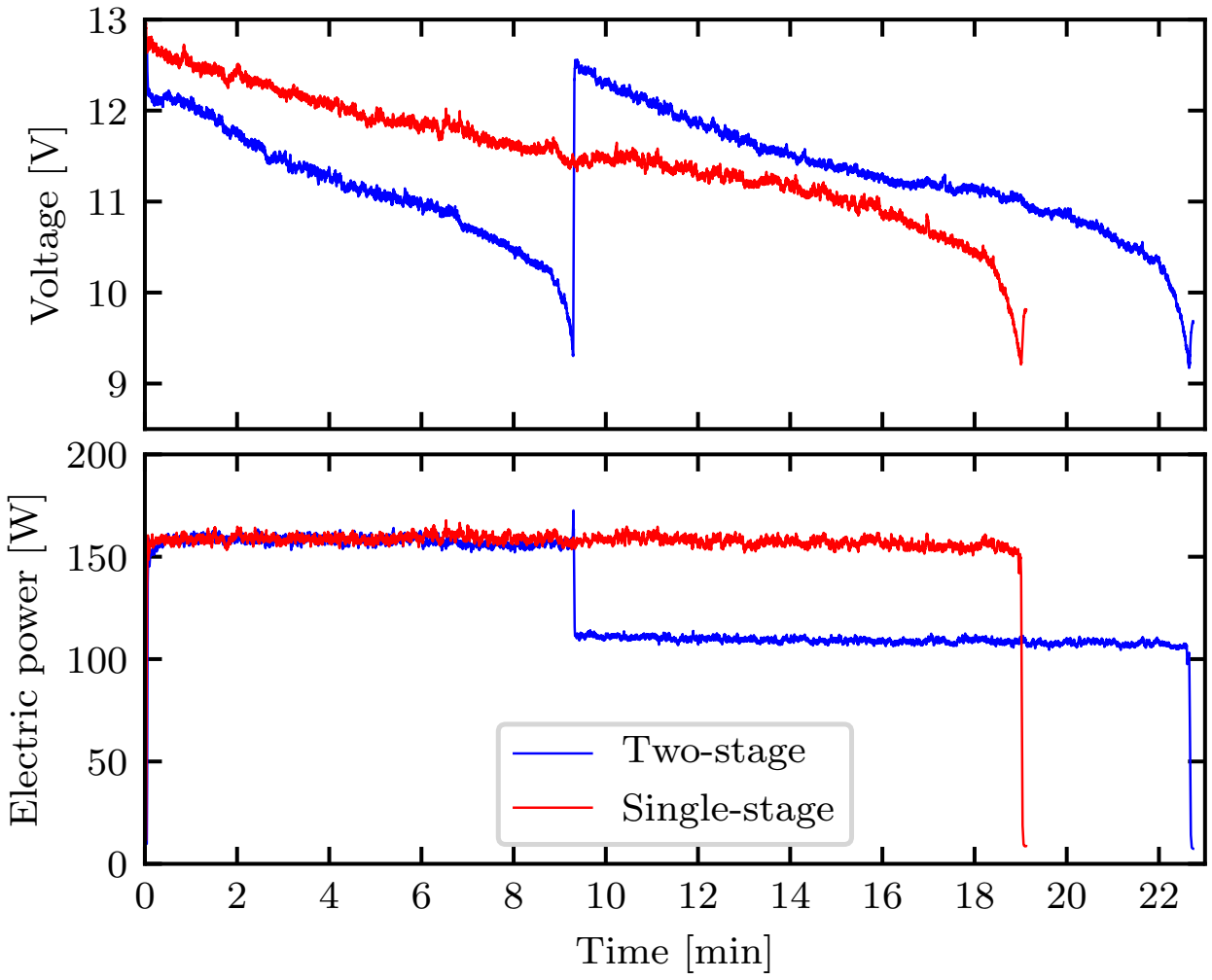

Figure 3.7: Input voltage and power vs. time measured at the electrical input to the quadcopter in typical experiments with the heavy batteries.

with a standard deviation of 0.32 min. These experiments are in agreement with the predictions, validating the optimal staging order analysis.

Discussion

The plots of input voltage and power vs. time for sample experiments from the single-stage and two-stage case are shown in Fig. 3.7. We see the characteristic LiPo battery discharge curve [69] in each of the voltage vs. time plots.

We observe that power input to the quadcopter remains approximately constant, as long

as its mass is not changing. For the single-stage experiments, the mass is constant for the entire experiment. For the two-stage experiments, the power input remains approximately constant until the first battery is completely discharged. Once we detach the first stage, the quadcopter mass is lower and the power consumption settles to a lower value corresponding to the reduced mass.

An important observation here is that energy consumption (calculated from power vs. time data) is similar for the single-stage and two-stage experiments with the heavy batteries. This is expected since we have the same total energy in all cases. The average energy consumption in the single-stage experiments is 1.819×10^5 J and in the two-stage experiments is 1.761×10^5 J. We note that the values mentioned here are the electrical energy utilized by the quadcopter. In the single-stage experiments, we are using two batteries in parallel which, in essence, halves the internal resistance, as compared to the two-stage experiments, where we are using one battery at a time. This increases the electrical efficiency, and thus the quadcopter is able to utilize more output energy for the same input energy in the single-stage experiments.

The flight time predictions match the experimental values within 5%. This validates that the assumptions used in the staging analysis are, in fact, realistic.

To be fair in comparing the flight times, we scale up the flight time of the single-stage experiments by a factor to account for the additional mass of the staging mechanism. This factor is obtained from the staging analysis by taking a ratio of the flight times with $m_d = 550\,\text{g}$ to flight time with $m_d = 595\,\text{g}$. Using $m_b = 380\,\text{g}$, the factor equals 1.07. The scaled single-stage flight time is 20.56 min. This shows that using the battery in stages is beneficial for flight time, even with the additional mass of the staging mechanism.

For an illustration, we compute the battery mass required for a single-stage vehicle to give us the same flight time as is obtained with two stages. Using Eq. (3.7) with $T_f = 22.8\,\text{min}$, $m_d = 550\,\text{g}$ (we exclude staging mechanism's mass), $N = 1$, and e_b and c_T same as before, we calculate $m_b = 525\,\text{g}$. So a single-stage vehicle would need an additional 145 g of battery to achieve the same flight time as a two-stage vehicle. Even considering the additional mass added by the staging mechanism, we save about 100 g or about 18% of the dry mass by using just one additional stage.

As a consequence of the increased flight time, the advantage of our proposed staging approach is a single flight, and hence a single continuous stream of data from sensors. Furthermore, any additional flight time could potentially lead to using just one multirotor instead of two or more with identical sensors, which is cost effective.

We note that the potential gains of using more stages are even higher, with certain flight times not achievable by a single-stage vehicle, as seen in Fig. 3.2. Since higher flight times can be achieved via staging without adding as much battery mass as required for a single stage, usually none or minimal changes to the vehicle's structure and powertrain would be required. Moreover, after each battery ejection, the inertia of the vehicle reduces, thereby increasing its agility.

3.5 Environmental Impact and Use Cases

It is important to note that there are potentially severe environmental effects to take into consideration when utilizing staged batteries, which limit their utility to special cases. Batteries ejected in mid-flight pose an immediate safety risk due to their momentum and kinetic energy when they reach the ground. Use of parachutes, as in the proof-of-concept in this chapter, reduces this risk but does not eliminate it, and moreover may make it harder to predict where the battery reaches the ground as external disturbances from the wind have a larger effect. Another major concern is the environmental impact of negligent disposal of batteries, including the substantial risk of impact ignition for batteries and the long-term pollution from the battery [70]. Moreover, most batteries are designed to be re-usable, meaning that discarding them without recovery would be wasteful.

For these reasons, application of staged batteries will likely be confined to specialized environments and circumstances. Examples may include long-duration surveillance of, e.g., industrial sites, where discarded batteries can be periodically collected for re-use and there is no danger of injuring third parties; use in emergencies such as in the event of a natural disaster, where the immediate value of longer-duration flight (such as transmitting warnings) out-weighs the longer-term impacts; or in extreme environments such as for space exploration missions on other celestial bodies.

3.6 Conclusion and Future Work

In this chapter, we have introduced the concept of staging energy sources for UAVs, specifically considering multirotors for our analysis. The idea is to discard the energy sources that cannot supply power anymore. This reduces the mass of the vehicle, thereby reducing power consumption. This, in turn, increases the overall flight time of the vehicle.

We presented a model to predict the flight time of a multi-stage multirotor with given physical parameters related to the energy source and power consumption. We then analyzed two specific cases of optimal staging. First, given N energy storage stages of fixed, known masses, we proved that flight time can be maximized by staging them in order of decreasing mass, with the heaviest stage being depleted and ejected first. Second, given an energy storage mass budget, finding the optimal way of partitioning it into N stages to maximize the flight time. This problem does not have a closed-form solution. Numerical results were presented and compared with the equal staging case.

We also presented an analysis for continuous staging of an internal combustion engine driving propellers. We observed that there is a fundamental limit on flight time when using I.C. engines, even when using an unlimited amount of fuel.

The staging analysis and optimal order of staging were validated experimentally by conducting flight experiments on a custom-designed two-stage quadcopter with a staging mechanism to detach a used battery in-flight. Experimental flight times matched well (within 5%) with the predicted flight times. The two-stage case showed a 19% higher flight time for

the same battery mass than the single-stage case (or 11% after correcting for the additional mass of the staging mechanism). We then discussed the environmental impact of discarding used stages, and specialized areas where the staging concept can be utilized.

Future work may include the use of additional stages to further increase the flight time. This would entail a more intricate design for ejection of each stage individually and for seamless switching between multiple energy sources. Another extension could be the planning of locations for stage ejections in an industrial setting, so that collection of these ejected stages can be localized and potentially automated.

Chapter 4

Unlimited endurance for eVTOL aircraft using Flying Batteries

We present an approach for unlimited endurance for eVTOL aircraft via mid-air docking and in-flight battery switching and recharging. A main vehicle flying using a primary battery has a docking platform attached to it. A 'flying battery' can dock with, and transfer power to the main vehicle. We analyze the flight time performance from an energy storage perspective for a self-contained hovering eVTOL and for an eVTOL using flying batteries, and show that on satisfying certain conditions on the recharging rate and onboard battery capacity, the eVTOL using flying batteries can fly for an unlimited duration. We then present a stochastic docking model which can be used as a design tool to choose parameters for the docking platform, with the objective of maximizing the probability of success of a mission. The generalized analysis and stochastic docking model are experimentally validated on a custom hardware instantiation in an indoor flight space. The combined mass of the main vehicle and one flying battery is 1.080 kg. We perform an 80-minute flight experiment involving repeated docking, battery switching plus recharging, and undocking, which is shown in the video attachment. At the end of the experiment, the primary battery on the main vehicle is nearly fully charged. Importantly, unlimited endurance is not associated with a large increase in overall mass or size, leaving the main vehicle in fundamentally the same safety class.

The material in this chapter is based on the following previously published work and its extension.

- Karan P Jain and Mark W Mueller. "Flying batteries: In-flight battery switching to increase multirotor flight time". In: *2020 IEEE International Conference on Robotics and Automation (ICRA)*. IEEE. 2020, pp. 3510–3516

4.1 Introduction

Electric vertical take-off and landing (eVTOL) aircraft are frequently employed in mapping, delivery, monitoring, and search and rescue missions [6, 7, 8, 9], among many other appli-

cations. This is owing to their ability to hover, and take off from, and land on, a small space, as opposed to fixed-wing aircraft that require long runways. However, they inherently have lower endurance and range as compared to fixed-wing aircraft [11]. An active area of research is to increase the endurance of eVTOLs, some of which will be discussed in the following section.

Related Work

Innovative approaches have been explored to increase the endurance and range of eVTOLs. Broadly, we can classify the approaches into two types: self-contained and externally assisted. Self-contained methods typically involve increasing mechanical or electrical efficiency or the use of optimization-based methods over objectives such as flight time or range. One such approach is exploiting the efficiency of a fixed-wing and hovering ability of eVTOLs by converting them into a hybrid aerial vehicle [18]. Manipulation of vehicle structure by tilting rotors to increase efficiency is shown in [17]. Tilting the propellers of an eVTOL in forward flight direction to reduce drag area and hence power consumption is shown in [19]. An online strategy for optimizing efficiency by altering flight parameters (e.g. speed) over a trajectory is presented in [20]. The analysis of a solar-powered aerial vehicle, which can potentially fly for a long time, is shown in [21]. However, such a vehicle requires a large wing span, is sensitive to weather conditions, and is not suitable for indoor settings.

Externally assisted methods typically involve the use of fixed stations or mobile vehicles for the replacement or the charging of energy sources. Battery swapping at a fixed ground station has been presented in [22, 23], and on a mobile ground base has been shown in [24]. One limitation of ground-based swapping stations is an interruption to the mission. For example, if an eVTOL's mission is monitoring a target, then going to a ground station for battery replacement could result in a mission failure.

Currently, unlimited flight time has been demonstrated either by tethering the eVTOL to a power source [25], or by power beaming via a LASER [27]. Tethering the eVTOL limits its range due to the tether length. Power beaming via LASER has a limited range (typically up to a kilometer [31]) and requires line of sight, so increasing the range of the eVTOL would entail having several LASER sources along the path which could be quite expensive because of the high fixed cost of installation of several LASERs and high variable cost due to low efficiency (typically less than 20% [32]).

A spare battery having the ability to *fly* to the aerial vehicle will enable an uninterrupted mission. This capability can be enhanced if the spare battery can be removed in flight after discharging so that another spare battery can take its place and continue providing energy. Moreover, this would allow a system to operate for long-distance flights without the disruption of stopping the flight, potentially a crucial feature to applications such as urban air mobility [2]. This is discussed in our original work [37] where we present the concept of a 'flying battery' – a secondary battery mounted on a small aerial vehicle. While a main eVTOL vehicle performs some long-duration task mid-air, a flying battery can fly towards the main vehicle and dock on it. The main vehicle can then get powered by the flying battery

Figure 4.1: A flying battery (above) about to dock on the main vehicle (below).

and charge its onboard battery simultaneously. Once the flying battery is depleted, it can undock, and another fully charged flying battery can dock in its place, making this process repeatable. This process removes energetic constraints on the flight time and is achieved while the main vehicle is airborne, so there is no interruption to the mission.

Fig. Figure 4.1 shows our experimental implementation, where a flying battery approaches the main vehicle to dock on it.

Contributions

In this work we build upon our original work on flying batteries [37] and have the following contributions:

- We present a flight time analysis to predict the flight time added by the flying batteries, and evaluate specific constraints on the recharging rate and the energy content of the primary battery that are necessary for an unlimited flight duration.

- We develop a stochastic docking model as a design tool to choose parameters for the docking mechanism and trajectory that maximizes the probability of success of a mission. Monte Carlo simulations are done to characterize this success probability theoretically. This is then experimentally validated for various docking mechanism designs.
- We experimentally validate that flying batteries enable unlimited endurance from an energy storage perspective. The battery switching circuit design is updated to include a charging circuit to recharge the primary battery (onboard the main vehicle). The recharging rate is chosen based on the constraints from the flight time analysis to unlock unlimited endurance. Moreover, the mechanical design of the docking mechanism is modified based on the stochastic model to improve the reliability of the system and the probability of success of docking.

4.2 Flight time analysis

In this section, we review the analysis from [37] for the flight time of a single battery-powered hovering eVTOL which shows that there exists a fundamental limit to the flight time. We then show an analysis for the flight time of an eVTOL using flying batteries – modular batteries that can attach and detach from the eVTOL, and show that an unlimited flight time is possible if designed correctly.

Flight time of a single eVTOL

We present an analysis of a fundamental limitation of hovering eVTOLs. Specifically, we show that the achievable flight time only increases up to a certain point, as more battery is used on a vehicle.

We model the aerodynamic power consumption p_i of an individual propeller i to be related to its thrust f_i as

$$p_i \propto f_i^{\frac{3}{2}}. \tag{4.1}$$

This can be derived from actuator disk theory [16], or from mechanical analysis of hub torque and rotational speed [17].

Assuming constant specific energy e_b, the total available energy E_{batt} in a battery will be e_b times the battery's mass.

Let m_0 be the "dry" mass (mass of all components of the eVTOL, excluding the battery), and let ϕ be the fraction of the *total* vehicle mass that is the battery mass so that the total vehicle mass is $\frac{1}{1-\phi}m_0$ and the battery mass is $\frac{\phi}{1-\phi}m_0$.

For a hovering eVTOL, the individual propeller thrusts scale proportionally with the vehicle's total mass. The electric power draw p_{elec} can be written as,

$$p_{\text{elec}} = k_p \left(\frac{1}{1-\phi} m_0\right)^{3/2}, \tag{4.2}$$

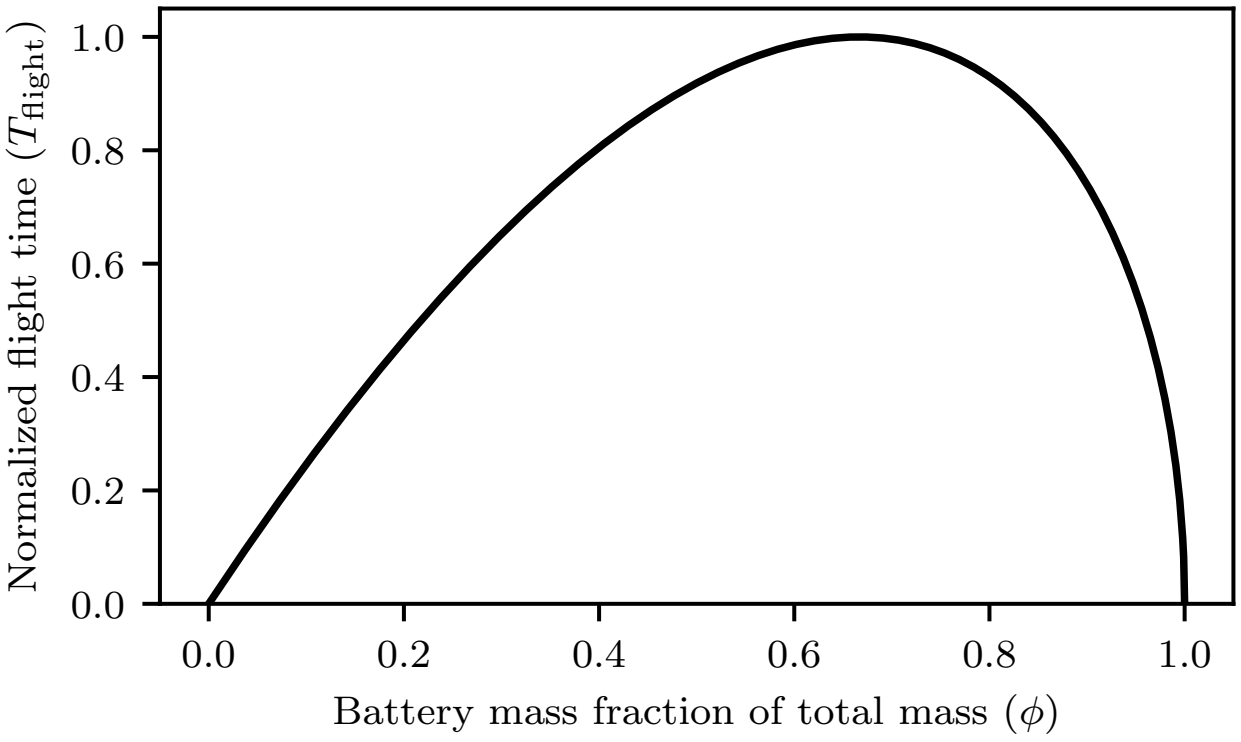

Figure 4.2: Effect of battery mass on normalized hovering flight time. After the peak at $\phi = \frac{2}{3}$, a larger battery reduces flight time.

where the power consumption coefficient k_p is determined by propeller design, gravitational acceleration, and powertrain efficiency. We assume these parameters are constant for a given vehicle.

The available flight time t_{flight} can then be related to the vehicle mass m_0, and battery mass fraction:

$$t_{\text{flight}} = \frac{E_{\text{batt}}}{p_{\text{elec}}} = \frac{e_b \frac{\phi}{1-\phi} m_0}{k_p \left(\frac{1}{1-\phi} m_0\right)^{3/2}} \propto \frac{\phi\sqrt{1-\phi}}{\sqrt{m_0}}. \tag{4.3}$$

This relationship is plotted in Figure 4.2, showing that vehicles with relatively small batteries expect to see a strong improvement in total flight time with increasing battery mass, until a peak where the battery takes up two-thirds of the vehicle's mass. We note that the location of this peak is independent of the specific energy e_b and the power consumption coefficient k_p. This large fraction makes structural design difficult and may lead to potential safety concerns.

A similar analysis for combustion-powered VTOL aircraft is presented in [35]. Although

these vehicles eject used fuel via exhaust, reducing the mass of the vehicle and power consumption continuously, they still face a similar fundamental limit on endurance. Their flight time cannot be increased arbitrarily by adding more fuel.

This analysis motivates our proposed system – by creating a system that enables the eVTOL to "shed" a discharged battery, and replace it with a fully charged battery, the eVTOL is able to exceed the flight-time limitation imposed by (4.3).

Flight time of a eVTOL using flying batteries

As discussed in the previous section, eVTOLs face a fundamental limit on flight time that cannot be exceeded by adding more batteries. However, if the system can swap a discharged battery with a charged one, this limitation can be overcome. In this section, we evaluate constraints on various parameters of the system such as recharging rate and battery energy content to allow the main vehicle to have unlimited endurance.

Let the main vehicle's total mass (without the flying battery) be m_{mv}, and the mass of the primary battery (battery onboard the main vehicle) be $m_{\text{mv,batt}}$. The primary battery is to power the main vehicle during the time the discharged flying battery is being replaced by a fully charged flying battery.

Similarly, let the flying battery's total mass be m_{fb}, and the mass of the secondary battery (battery onboard the flying battery, which powers it and also the main vehicle on docking) be $m_{\text{fb,batt}}$.

We assume the specific energy e_b is the same for both batteries. So the energy content in the primary battery E_{mv} and the secondary battery E_{fb} are respectively given by,

$$E_{\text{mv}} = e_b m_{\text{mv,batt}}, \quad E_{\text{fb}} = e_b m_{\text{fb,batt}}. \tag{4.4}$$

The power consumption coefficients of the main vehicle and the flying battery are $k_{\text{p,mv}}$ and $k_{\text{p,fb}}$ respectively. We assume the power consumption by the flying battery during its flight to dock with the main vehicle is close to its power consumption in hover,

$$p_{\text{fb}} = k_{\text{p,fb}} m_{\text{fb}}^{3/2}. \tag{4.5}$$

Similarly, the power consumption of the main vehicle during hover in individual flight, and when it is docked with the flying battery, is given by

$$p_{\text{mv}} = k_{\text{p,mv}} m_{\text{mv}}^{3/2} \tag{4.6}$$

$$p_{\text{mv,docked}} = k_{\text{p,mv}} \left(m_{\text{mv}} + m_{\text{fb}}\right)^{3/2}. \tag{4.7}$$

Let the upper bound of the time it takes for the flying battery to take off and dock with the main vehicle be t_{dock}, and the upper bound of the time it takes for it to undock and land be t_{undock}. The total energy consumption by the flying battery to power itself then has an upper bound of

$$E_{\text{fb,self}} = p_{\text{fb}} \left(t_{\text{dock}} + t_{\text{undock}}\right). \tag{4.8}$$

We estimate the energy consumed by the main vehicle during the phase it is being powered by the primary battery. The power consumption is assumed to be the same as that in the docked configuration (4.7) (where the main vehicle also carries the flying battery), because during docking and undocking, the downwash from the flying battery leads to the main vehicle producing a higher thrust, which is upper bounded by the weight of the main vehicle plus the weight of the flying battery [38]. The time that the main vehicle remains in this state is upper bounded by the sum of times it takes for a discharged flying battery to undock and the time it takes for a fully charged flying battery to dock since there can be some overlap in the two processes.

$$E_{\text{mv,self}} = p_{\text{mv,docked}} \left(t_{\text{undock}} + t_{\text{dock}} \right) \tag{4.9}$$

This gives us the first design constraint of the system – the energy in the primary battery must be higher than the energy it consumes when the main vehicle is powered by the primary battery,

$$E_{\text{mv}} \geq E_{\text{mv,self}}. \tag{4.10}$$

The flying battery, once docked, is drained by two processes: (i) powering the main vehicle and (ii) recharging the primary battery. The energy to be added back to the primary battery is given by (4.9). Thus, the time that the main vehicle can fly with the flying battery is calculated as,

$$\begin{aligned} t_{\text{mv,docked}} &= \frac{E_{\text{fb}} - E_{\text{fb,self}} - E_{\text{mv,self}}/\eta_{\text{rech}}}{p_{\text{mv,docked}}} \\ &= \frac{E_{\text{fb}} - E_{\text{fb,self}}}{p_{\text{mv,docked}}} - \frac{t_{\text{undock}} + t_{\text{dock}}}{\eta_{\text{rech}}}, \end{aligned} \tag{4.11}$$

where η_{rech} is the efficiency of the recharging process.

This poses the second constraint – the recharging rate p_{rech} of the primary battery should be fast enough to replenish the lost energy in the time the flying battery is docked,

$$p_{\text{rech}} \geq \frac{E_{\text{mv,self}}}{\eta_{\text{rech}} t_{\text{mv,docked}}}. \tag{4.12}$$

Using equations (4.4), (4.5), (4.7), (4.8), and (4.11), we can rewrite the above as,

$$p_{\text{rech}} \geq \frac{p_{\text{mv,docked}}^2}{\eta_{\text{rech}} \left(\frac{e_b m_{\text{fb,batt}}}{t_{\text{dock}} + t_{\text{undock}}} - k_{\text{p,fb}} m_{\text{fb}}^{3/2} \right) - p_{\text{mv,docked}}}. \tag{4.13}$$

The takeaway from (4.13) is that the recharging rate has an increasing trend as the power consumption of the main vehicle in the docked configuration increases, as the sum of time to dock and time to undock increases, and as the recharging efficiency decreases.

If the denominator in (4.13) is negative, then the primary battery cannot be recharged fast enough to allow for an unlimited flight time.

If we can arrive at a finite, positive value for the recharging rate, for which an appropriate charging circuit can be designed, then the flying batteries approach lifts the fundamental flight time limit, so that the system's endurance is no longer limited by energy storage constraints.

For a mission of duration t_{mission}, we can estimate the total number of dockings N_{dock} (or flying batteries to be stationed for a long-range mission) as,

$$N_{\text{dock}} \approx \left\lceil \frac{t_{\text{mission}}}{t_{\text{mv,docked}} + t_{\text{dock}} + t_{\text{undock}}} \right\rceil . \tag{4.14}$$

In practice, the docking procedure would have a non-zero probability of failure due to uncertainties in the state estimates (which we will evaluate in Section 4.4), and other factors such as wind. For most cases, it should be possible to evaluate the probability of success of docking, either via a model or empirically. Let this probability be Prob(docking success). Then we can evaluate the probability of success of the long-duration mission, as the probability of successfully docking N_{dock} times in a row,

$$\text{Prob(mission success)} = (\text{Prob(docking success)})^{N_{\text{dock}}} \tag{4.15}$$

This can be used to design the system to ensure that it has a desired probability of success for the respective mission.

4.3 Docking mechanism and approach

Mid-air docking of multirotors has been performed using a variety of mechanisms. Robotic hands, a winch, and a rod were used by [71] to dock vehicles vertically aligned. Lateral docking using magnets has been demonstrated in [72]. We use a mechanical guide structure in the form of a landing platform on the main vehicle and landing legs on the flying battery as shown in Figure 4.3. This enables a fast docking procedure along with an easy undocking process. This design achieves the following objectives:

- *No active components:* The mechanism does not consume power and uses the weight of the flying battery for docking. This makes it lightweight and leads to a simple undocking process – regular take-off.
- *Docks vertically aligned:* The flying battery does not produce any thrust when docked. Ensuring that the center of mass of the system in the docked configuration is at the geometric center of the propellers (in the horizontal plane) prevents imbalanced thrusts. This prevents additional power consumption since it grows superlinearly with thrust as per (4.1).
- *Allows efficient power transfer:* We desire a secure and efficient electrical contact after docking to power the main vehicle from the flying battery.

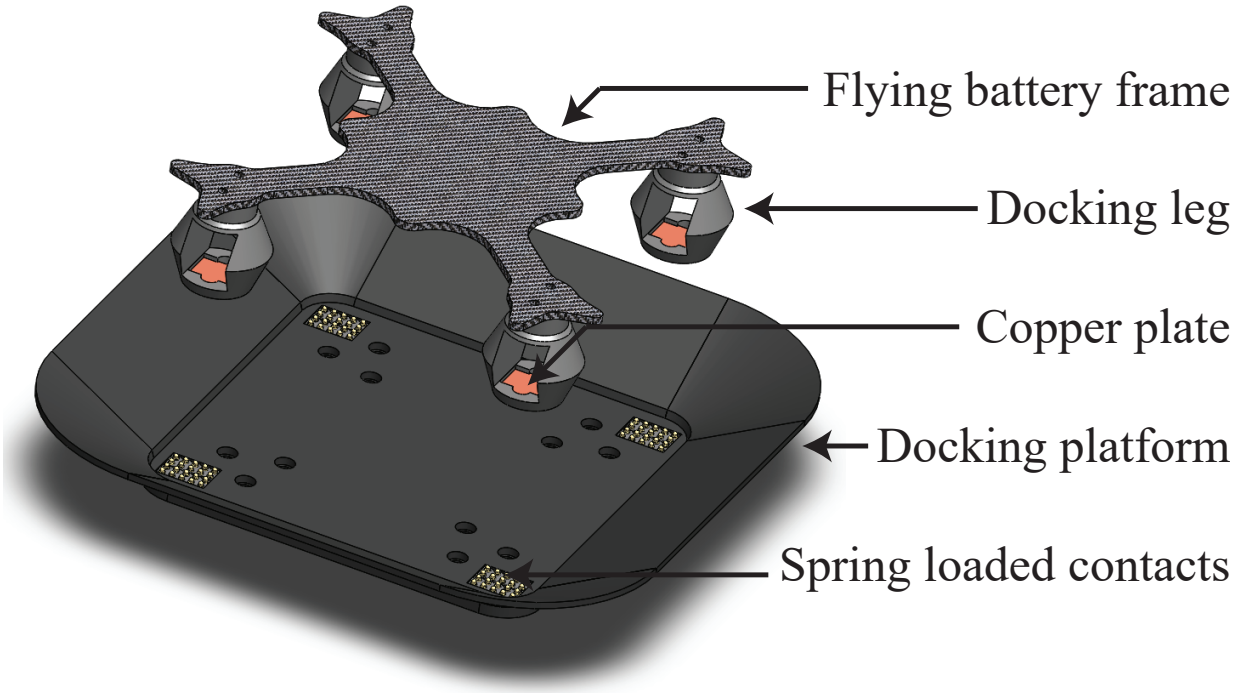

Figure 4.3: Design of the docking mechanism with electrical connectors. The docking platform is mounted on the main vehicle, as can be seen in Figure 4.7.

The docking platform and the legs include electrical connectors which can allow the transfer of power from a flying battery to the main vehicle. The docking mechanism allows some lateral play between the vehicles to facilitate smooth docking and undocking, but this play is limited sufficiently to ensure that the electrical connections are not broken due to vibrations and dynamic motions.

The docking platform is designed to be larger than the flying battery so that it is forgiving to small position and yaw errors when the flying battery lands on it. The extra width of the docking platform is defined as the radius of forgiveness r_f. This can be seen in Figure 4.4.

We note here that even though our docking mechanism lacks any fixing or clamping mechanism, the main vehicle can still perform agile maneuvers in the docked configuration because of the nature of relative forces that act on the two vehicles. We expand on this in Appendix A.

Docking trajectory

The docking trajectory is chosen to be quasi-static to ensure that the docking has a high probability of success. It is described as follows:

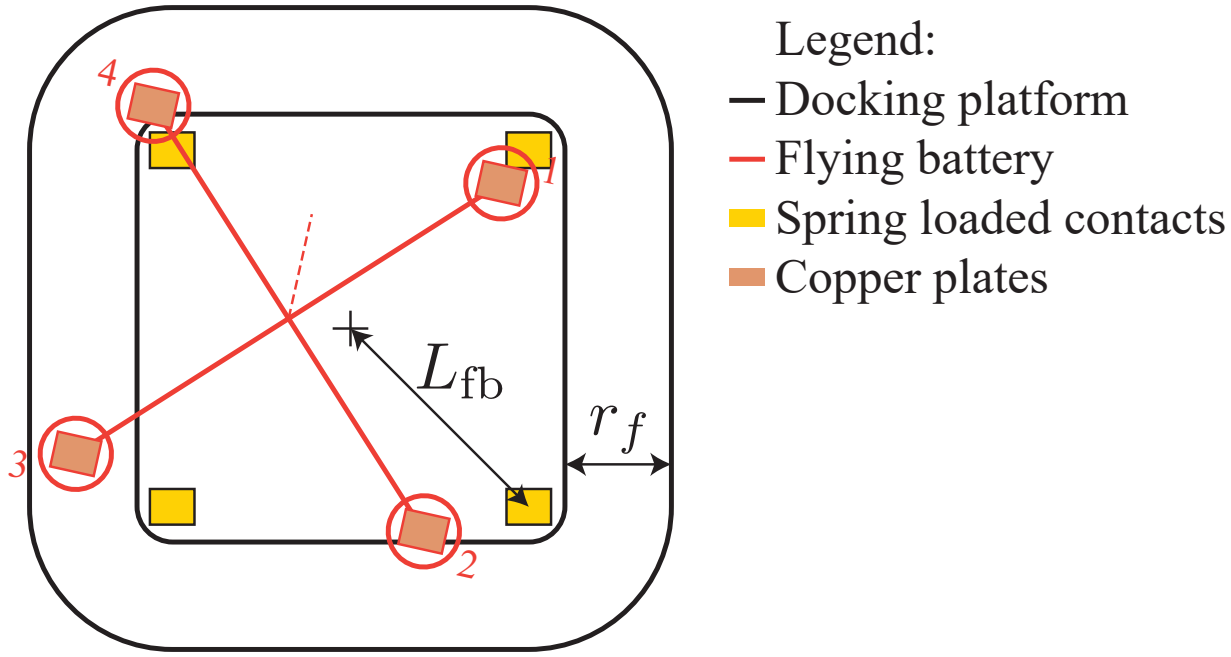

Figure 4.4: Illustration showing a typical landing position of the flying battery on the docking platform of the main vehicle, before being guided into the correct position. In this figure, since all the docking legs are within the bounds of the docking platform, this landing is a successful docking.

1. The main vehicle hovers at a fixed desired position.
2. The flying battery approaches the main vehicle from above to align vertically when viewed from the top.
3. The flying battery begins to descend towards the main vehicle.
4. The flying battery waits for the drop condition to be satisfied given by (4.17).
5. Once the drop condition is satisfied, the motors on the flying battery turn off, and it falls freely onto the docking platform on the main vehicle.

The drop condition depends on the relative position and velocity of the two vehicles. The position and velocity states of the vehicles are shown in Figure 4.5. We compute some nominal parameters – specifically, the estimated time to land from the drop $\bar{t}_{\text{drop}}$, the estimated landing position of the flying battery with respect to the main vehicle in the x

and y direction, $\bar{p}_{1,\text{land}}$ and $\bar{p}_{2,\text{land}}$ respectively.

$$\begin{aligned} \bar{t}_{\text{drop}} &= \sqrt{\frac{2(p_{3,\text{fb}} - p_{3,\text{mv}})}{g}}, \\ \bar{p}_{1,\text{land}} &= (p_{1,\text{fb}} - p_{1,\text{mv}}) + (v_{1,\text{fb}} - v_{1,\text{mv}})\bar{t}_{\text{drop}}, \\ \bar{p}_{2,\text{land}} &= (p_{2,\text{fb}} - p_{2,\text{mv}}) + (v_{2,\text{fb}} - v_{2,\text{mv}})\bar{t}_{\text{drop}}. \end{aligned} \tag{4.16}$$

Based on these parameters, the flying battery is commanded to dock and drop if the position and velocity of the two vehicles satisfy the following conditions.

$$\begin{aligned} p_{3,\text{fb}} - p_{3,\text{mv}} &\leq h_c, \\ |\psi_{\text{fb}} - \psi_{\text{mv}}| &\leq \psi_c, \\ |v_{\text{i,fb}} - v_{\text{i,mv}}| &\leq v_c, \quad i = 1, 2, 3 \\ \bar{p}^2_{1,\text{land}} + \bar{p}^2_{2,\text{land}} &\leq r_c^2, \end{aligned} \tag{4.17}$$

where h_c is the cutoff height for the drop, ψ_c is the cutoff yaw, v_c is the cutoff velocity, and r_c is the cutoff radius.

We will discuss a principled approach for choosing the size of the docking platform, based on a stochastic model for docking, to have an appropriate probability of success, without adding too much weight to the system in Section 4.4.

4.4 Stochastic docking model

In this section, we present a stochastic model to characterize the docking success rate with respect to various design parameters, such as the dropping height, and the radius of forgiveness of the docking platform. This can be used to design the system such that it meets a desired probability of success for a mission, which can be evaluated using (4.15).

Predictions from the model are made via Monte Carlo simulations. These are then validated against several drop experiments done for different docking platform designs and different drop heights in Section 4.6.

Multicopter dynamics

Using Newton-Euler equations, the continuous time nonlinear dynamics of a multicopter under disturbances can be written as (see [73]),

$$\begin{aligned} \dot{\boldsymbol{p}} &= \boldsymbol{v}, \\ \dot{\boldsymbol{v}} &= \frac{1}{m} f_T \mathbf{R} \boldsymbol{e}_3 + g + \boldsymbol{d}_a, \\ \dot{\mathbf{R}} &= \mathbf{R}\mathbf{S}(\boldsymbol{\omega}), \\ \dot{\boldsymbol{\omega}} &= \mathbf{J}^{-1}(\boldsymbol{\tau} - \mathbf{S}(\boldsymbol{\omega})\mathbf{J}\boldsymbol{\omega}) + \boldsymbol{d}_\alpha, \end{aligned} \tag{4.18}$$

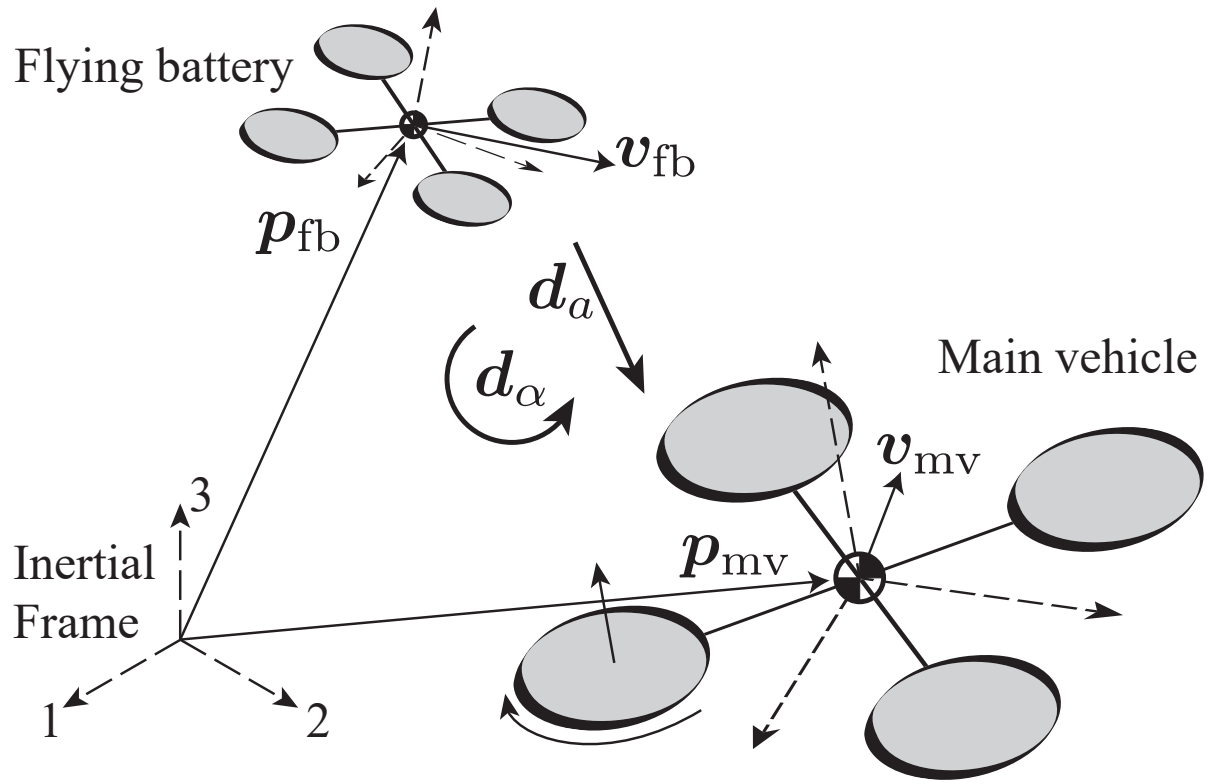

Figure 4.5: Illustration showing a typical proximity flight of the flying battery and the main vehicle along with position and velocity states, and the disturbances on the vehicles.

where $\boldsymbol{p}$ is the position of the multicopter, $\boldsymbol{v}$ is its velocity, $\mathbf{R}$ is its attitude represented as a rotation matrix, and ω is its angular velocity in its body-fixed frame. The mass of the vehicle is denoted by m, its moment of inertia tensor by $\mathbf{J}$, and the acceleration due to gravity by g. The control inputs are the thrust of the vehicle f_T, and the torque produced by it $\boldsymbol{\tau}$, also in the body-fixed frame. Lastly, the disturbance in the translational and rotational dynamics are denoted by $\boldsymbol{d}_a$ and $\boldsymbol{d}_\alpha$ respectively.

This model given by (4.18) can be linearized about the hover state to give,

$$\dot{\boldsymbol{x}}(t) = \boldsymbol{A}_c\boldsymbol{x}(t) + \boldsymbol{B}_c\boldsymbol{u}(t) + \boldsymbol{d}_c(t), \tag{4.19}$$

where $\boldsymbol{x} = \left(\boldsymbol{p}^T, \boldsymbol{v}^T, \boldsymbol{\delta}^T, \boldsymbol{\omega}^T\right)^T$ is the state of the vehicle, with $\boldsymbol{\delta} = (\phi, \theta, \psi)^T$ being the linearized attitude representation, chosen to be Euler angles in the yaw-pitch-roll format for convenience. The disturbances are denoted by $\boldsymbol{d}_c$.

State uncertainty model

We use a Linear Quadratic Gaussian (LQG) controller for our vehicles and get an estimate for the uncertainty in the states of the vehicle from the steady state solution to the LQG controller. In this model, we augment the states of the flying battery and the main vehicle as,

$$\boldsymbol{x} = \begin{bmatrix} \boldsymbol{x}_{\text{fb}} \\ \boldsymbol{x}_{\text{mv}} \end{bmatrix} \tag{4.20}$$

Since we are running our controller and estimator on a digital system, we use the discrete-time version of the dynamics in (4.19), given by,

$$\boldsymbol{x}(t + \Delta t) = \boldsymbol{A}\boldsymbol{x}(t) + \boldsymbol{B}\boldsymbol{u}(t) + \boldsymbol{d}(t). \tag{4.21}$$

The disturbance is assumed to be a zero-mean, normally distributed process noise $\boldsymbol{d}$ with a known variance $\boldsymbol{\Sigma_d}(\boldsymbol{p}_{\text{des,fb}} - \boldsymbol{p}_{\text{des,mv}})$, i.e. it is assumed to be a function of the nominal relative position of the two vehicles [38]. Note that this is still consistent with the LQG controller's assumption that the process noise is independent of the state, because we are not using the true position states in the function, but the nominal desired positions that we expect the vehicles to hover at before docking.

The measurement model is given by,

$$\boldsymbol{z}(t) = \boldsymbol{H}\boldsymbol{x}(t) + \boldsymbol{w}(t), \tag{4.22}$$

where $\boldsymbol{H}$ is the measurement model matrix, $\boldsymbol{z}$ is the measurement, and $\boldsymbol{w}$ is a zero-mean, normally distributed measurement noise with a known variance $\boldsymbol{\Sigma_w}$.

Finally, from the steady state LQG framework [74], we have the following equations that tell us about the steady state uncertainties in the state,

$$\begin{aligned} \boldsymbol{P}_{\text{p}} = \boldsymbol{\Sigma_d} + \boldsymbol{A}\boldsymbol{P}_{\text{p}}\boldsymbol{A}^T - \\ \boldsymbol{A}\boldsymbol{P}_{\text{p}}\boldsymbol{H}^T \left(\boldsymbol{H}\boldsymbol{P}_{\text{p}}\boldsymbol{H}^T + \boldsymbol{\Sigma_w}\right)^{-1} \boldsymbol{H}\boldsymbol{P}_{\text{p}}\boldsymbol{A}^T \end{aligned} \tag{4.23}$$

$$\boldsymbol{P}_{\text{m}} = \boldsymbol{P}_{\text{p}} - \boldsymbol{P}_{\text{p}}\boldsymbol{H}^T \left(\boldsymbol{H}\boldsymbol{P}_{\text{p}}\boldsymbol{H}^T + \boldsymbol{\Sigma_w}\right)^{-1} \boldsymbol{H}\boldsymbol{P}_{\text{p}} \tag{4.24}$$

where (4.23) is the implicit Ricatti equation and is used to compute $\boldsymbol{P}_{\text{p}}$, and the steady state uncertainty in the state is given by $\boldsymbol{P}_{\text{m}}$ computed from (4.24).

Landing model

We have the following design parameters in our model: h_c, ψ_c, v_c, r_c as described in Section 4.3, and radius of forgiveness of the docking plate r_f which is the width of each flange of the docking platform in top view, as shown in Figure 4.4.

In the LQG framework [74], the state estimator is unbiased, i.e. the value of the state estimate is the mean of the true state,

$$\hat{\boldsymbol{x}} = E[\boldsymbol{x}]\,. \tag{4.25}$$

The variance of the state is given by the steady state LQG state estimation error variance. Since we have the assumption of normal distribution on the process noise and measurement noise, and all transformations are linear, the true state is normally distributed as,

$$\boldsymbol{x} \sim \mathcal{N}(\hat{\boldsymbol{x}}, \boldsymbol{P}_{\mathrm{m}})\,. \tag{4.26}$$

The state estimation error, $\boldsymbol{e} = \hat{\boldsymbol{x}} - \boldsymbol{x}$, is also normally distributed as,

$$\boldsymbol{e} \sim \mathcal{N}(\boldsymbol{0}, \boldsymbol{P}_{\mathrm{m}})\,. \tag{4.27}$$

The flying battery is commanded to dock when the state estimates of the two vehicles simultaneously satisfy all the conditions given in (4.17).

The true dropping time of the flying battery is given by,

$$t_{\mathrm{drop}} = \frac{\sqrt{2p_{3,\mathrm{rel}}g + v_{3,\mathrm{rel}}^2} + v_{3,\mathrm{rel}}}{g}, \tag{4.28}$$

where $p_{3,\mathrm{rel}} = (p_{3,\mathrm{fb}} - p_{3,\mathrm{mv}})$, and $v_{3,\mathrm{rel}} = (v_{3,\mathrm{fb}} - v_{3,\mathrm{mv}})$.

The true landing position of the flying battery with respect to the main vehicle is then given by,

$$\begin{aligned} p_{1,\mathrm{land}} &= (p_{1,\mathrm{fb}} - p_{1,\mathrm{mv}}) + (v_{1,\mathrm{fb}} - v_{1,\mathrm{mv}})\, t_{\mathrm{drop}}, \\ p_{2,\mathrm{land}} &= (p_{2,\mathrm{fb}} - p_{2,\mathrm{mv}}) + (v_{2,\mathrm{fb}} - v_{2,\mathrm{mv}})\, t_{\mathrm{drop}}. \end{aligned} \tag{4.29}$$

Lastly, we can compute the position of the docking legs of the flying battery and check whether they are within the docking platform bounds, using the geometry of the system as shown in Figure 4.4.

The Monte Carlo simulation is described in Algorithm 1.

In this work, we only study the effect of the cutoff drop height h_c and the radius of forgiveness of the docking platform r_f on the probability of success of docking, as these were found to be the parameters that most affected the docking success probability. The other parameters (ψ_c, v_c, r_c) were found to have a negligible effect on the docking success probability in the range of values we explored. Doing the Monte Carlo simulations for various drop heights and radii of forgiveness, we get a plot as shown in Figure 4.6. The docking condition parameters for these simulations are,

$$r_c = 0.01\,\mathrm{m}, \quad v_c = 0.05\,\mathrm{m\,s^{-1}}, \quad \psi_c = 2^\circ. \tag{4.30}$$

These parameters were chosen empirically for our system (which is an instantiation of this generalized analysis) by evaluating the tradeoff between the success rate of docking and the time it takes to dock t_{dock}.

We observe that there exists an optimal cutoff drop height that maximizes the probability of success. This is because of the following reasons:

Algorithm 1 Monte Carlo simulation to characterize the probability of docking success

Input: $r_c, \psi_c, v_c, h_c, r_f$
Output: Prob(docking success)
dock_success_count = 0
dock_attempt_count = 0
for $k = 0$ to N_{sim} **do**
    Sample true states from (4.26)
    Sample state estimation errors from (4.27)
    Evaluate state estimates using $\hat{\boldsymbol{x}} = \boldsymbol{x} + \boldsymbol{e}$
    if (state estimate satisfies (4.17)) **then**
        dock_attempt_count++
        Compute the time of drop from (4.28)
        Compute the landing position from (4.29)
        Compute positions of the docking legs (see Figure 4.4)
        if (docking legs inside docking platform bounds) **then**
            dock_success_count++
return dock_success_count / dock_attempt_count

- At low drop heights, the two vehicles are very close to each other during docking, which results in a very high process noise variance because of the downwash. This is expected to increase the variance in the relative position and velocity, resulting in higher uncertainty in the relative position on landing, and a lower probability of success.

- At high drop heights, the dropping time is higher. Since the velocity error due to uncertainty adds up during the drop, there is a higher uncertainty in the landing position, resulting in a lower probability of success.

The two factors above are expected to trade off such that the combined effects due to them are minimized at an optimal dropping height, resulting in a maximized probability of success.

We also observe that the optimal cutoff drop height increases as the radius of forgiveness of the docking platform increases. We hypothesize that this is due to the slightly higher kinetic energy required to slide from various landing positions since there is a larger area to land on.

The trend of the probability of success with respect to the cutoff radius, velocity, and yaw angle for docking is observed to be much weaker than for the cutoff drop height and radius of forgiveness. These are thus omitted for brevity. Moreover, tightening those parameters leads to a stricter condition for docking, resulting in a lower probability of meeting those conditions simultaneously in flight. This is experimentally observed to result in a higher average time to dock t_{dock}, which is undesirable, as it results in higher power consumption and increases the required recharging rate for unlimited endurance.

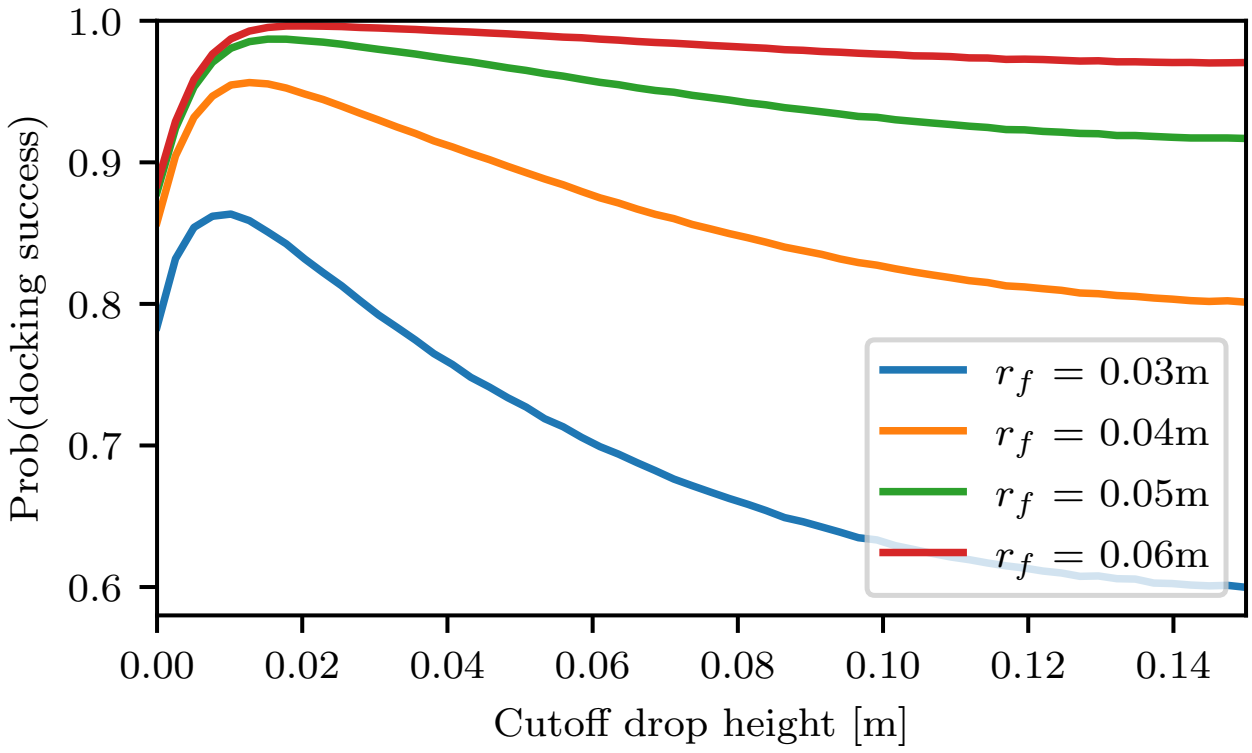

Figure 4.6: Probability of successful docking vs. cutoff drop height h_c for different docking platform radius of forgiveness r_f.

With this model, we can pick a radius of forgiveness that meets our desired probability of success of docking mission, or desired probability of success of mission from (4.15). Although the probability of success increases monotonically with the radius of forgiveness, we note that designing with a higher radius of forgiveness increases the mass of the docking platform and the main vehicle, and would lead to a higher power consumption. Thus we cannot design an arbitrarily large docking platform and the tradeoff of probability of success with the mass of the docking platform needs to be evaluated.

4.5 Experimental Hardware Design

In this section, we use our design methodology developed in the previous sections to instantiate an experimental system, where the combined mass of the main vehicle and one flying battery is on the order of 1 kg. For this system, we explain the design of the vehicles, the mid-air docking mechanism, and the battery switching and recharging circuit.

Table 4.1: Specifications of vehicles used in experiments

Parameter	Main vehicle	Flying battery
Propeller diameter	203 mm	76 mm
Arm length	165 mm	58 mm
Mass	750 g	330 g
Maximum thrust	27 N	8 N

Vehicle design

Main vehicle

The main vehicle is designed to have enough payload capacity for carrying useful sensors such as surveillance cameras, or environmental sensors. The battery switching and charging circuit and docking platform are stacked on top of the main vehicle. Spring-loaded connectors are mounted on the docking platform to serve as input leads to the vehicle from the secondary battery. Voltage sensors are connected across both the primary and the secondary battery, and a current sensor is connected at the input to the main vehicle. The primary battery is a 3S 1.5 Ah Lithium Polymer (LiPo) battery, which weighs 135 g.

Flying battery

The flying battery is a small aerial vehicle that is designed to have sufficient payload capacity to carry the secondary battery for the main vehicle. The docking legs for the flying battery are designed to minimize blockage of the propeller airflow to minimally affect the payload capacity. Copper plates of dimensions similar to the spring-loaded connectors are installed on the legs to serve as the secondary battery output leads. The flying battery is powered by the same "secondary" battery that powers the main vehicle after docking. The secondary battery is a 3S 2.2 Ah LiPo battery, which weighs 190 g.

Table 4.1 summarizes the specifications of the two vehicles.

Docking mechanism

The design methodology of the docking mechanism has been explained in Section 4.3. We choose a docking platform with a radius of forgiveness of $r_f = 0.04\,\text{m}$. This is to have a high probability of success of docking, while not adding too much mass to the main vehicle. The docking platform and the docking legs can be seen on the respective vehicles in Figure 4.7.

Battery switching and recharging circuit

We design a circuit to enable seamless switching of power source between the primary battery and secondary battery. We also add a charging circuit which enables the secondary

Figure 4.7: *Top:* Main vehicle with the docking platform and spring-loaded connectors. *Bottom:* Flying battery with the docking legs and copper plate connectors.

battery to simultaneously power the main vehicle, and recharge the primary battery in-flight. The parameters such as recharging rate follow from the flight time analysis presented in Section 4.2.

Since our system is flying, we cannot afford to cut the power supply during this switch. The two batteries need to be connected in parallel for some time to achieve this, and this is only safe within a voltage difference of 0.2 V per cell for LiPo batteries. This would often not be the case in our application because we intend to utilize the secondary battery from a fully charged state (4.2 V per cell) to a completely discharged state (3.0 V per cell). We solve this by connecting diodes in series with each of the batteries to avoid reverse currents. We utilize smart bypass diodes because they have a much lower voltage drop than conventional P-N junction or Schottky diodes. At our operating current of about 16 A, the voltage drop is less than 0.1 V.

A relay is connected in series with the primary battery. In normal operating conditions, it is set to power the main vehicle. By switching the relay, we can draw power solely from the secondary battery even when it is at a lower voltage than the primary battery. We also have a charging circuit connected to the other node of the relay, so we are able to simultaneously recharge the primary battery during this phase of operation. A voltage boost converter with an output of 15 V is connected to the input leads of the charging circuit to ensure that the charging voltage is always above the primary battery voltage. The charging current is set to 2.0 A based on (4.13) to ensure that the amount of charge added is higher than the amount of charge consumed.

The relay coil is connected across the secondary battery input leads in series with a MOSFET. This ensures that the switch does not open without a secondary battery, and allows us to use a GPIO pin on the flight controller to control the switch. Figure 4.8 shows a schematic diagram of the battery switching and charging circuit.

4.6 Experimental validation

In this section, we validate the stochastic docking model covered in Section 4.4. We then ensure that our design meets the constraints covered in Section 4.2 along with a high safety factor. Lastly, we validate the use of our design by conducting a long-duration flight experiment involving repeated docking, battery switching and recharging, and undocking and show that the primary battery voltage is approximately the same at the beginning and the end of the experiment.

Validation of stochastic docking model

The stochastic docking model is validated by doing experiments on several different docking platform designs with varying radii of forgiveness and drop heights.

The results are shown in Figure 4.10. We observe a similar trend as predicted by the model where there the probability of docking success increases, reaches an optimal drop-

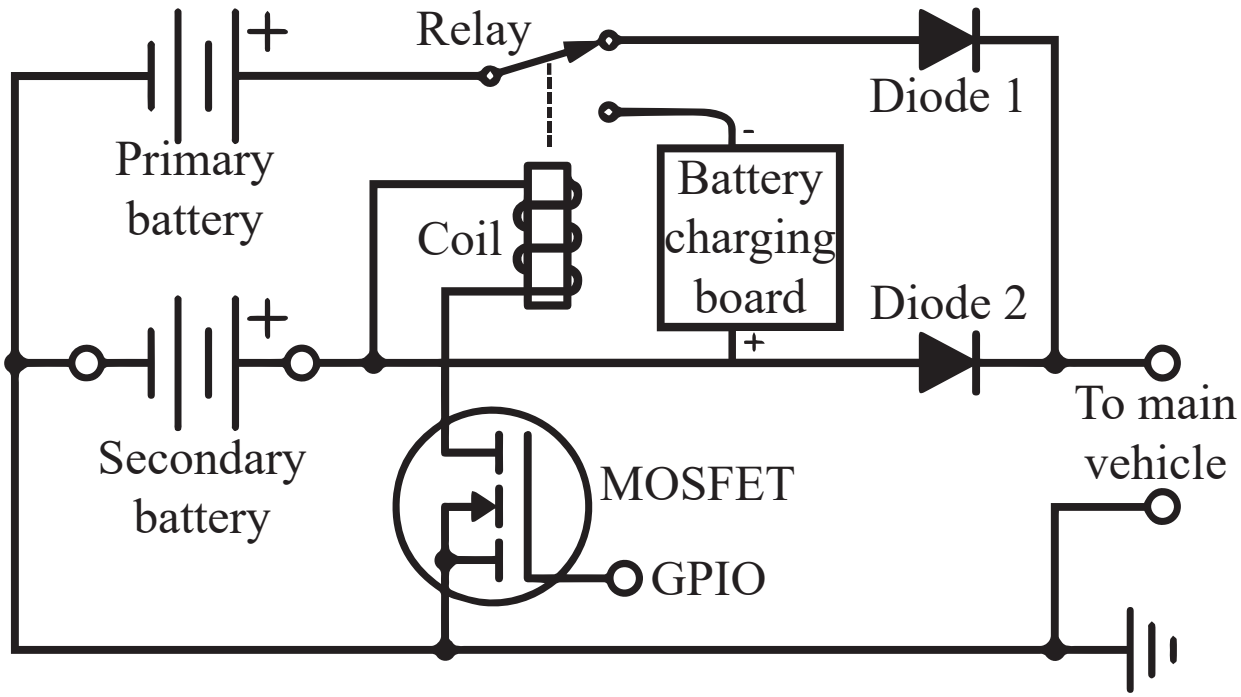

Figure 4.8: Schematic of the battery switching and charging circuit.

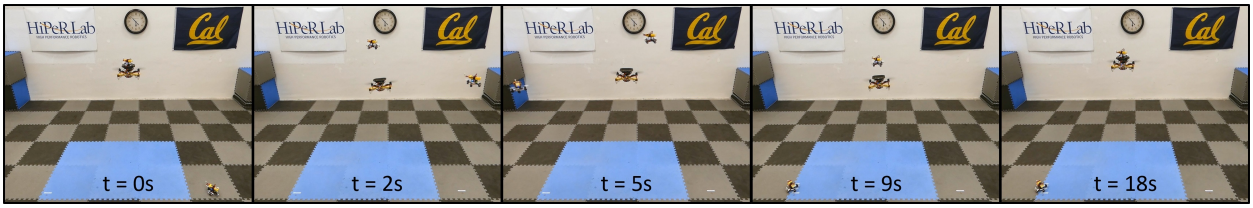

Figure 4.9: Steps (4)-(6) of the demonstration. From left to right, (a) main vehicle hovers with a flying battery docked on it, (b) the first flying battery is depleted, so it undocks and another fully charged flying battery takes off, (c) the second flying battery moves towards the main vehicle to dock and the first flying battery begins landing, (d) the second flying battery descends to dock on the main vehicle, (e) the second flying battery is docked on the main vehicle (which continues to hover) and the first flying battery has landed - we now manually replace the discharged flying battery with a fully charged one.

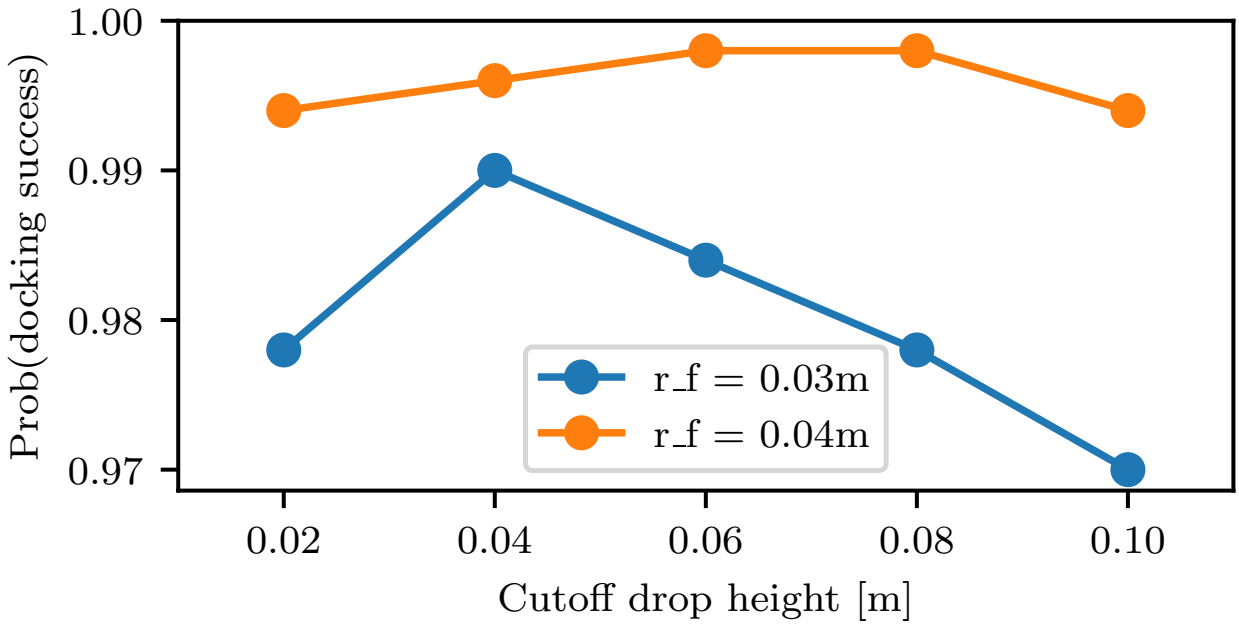

Figure 4.10: Experimental probability of successful docking vs. cutoff drop height h_c for different docking platform radius of forgiveness r_f. Validated with 500 tests for each data point.

ping height, and then decreases. We also see that the success probability value and the optimal drop height is higher for the docking platform with a higher radius of forgiveness ($r_f = 0.04\,\text{m}$).

Predictions from flight time analysis

In this section, we predict the time that each flying battery can power the main vehicle for, using (4.11). We also compute relevant values in the two constraints, (4.10) and (4.13), and reason about why we choose the specific primary battery and recharging rate.

The power consumption coefficients, as defined in (4.2), are determined empirically for the main vehicle and the flying battery. The computed values are,

$$k_{\text{p,mv}} = 164.3\,\text{W/kg}^{3/2}, \quad k_{\text{p,fb}} = 1050.0\,\text{W/kg}^{3/2}. \tag{4.31}$$

Based on empirical data, the highest time to take off and dock, and the highest time to undock and land respectively, as observed from flight experiments is,

$$t_{\text{dock}} = 28.5\,\text{s}, \quad t_{\text{undock}} = 7.0\,\text{s}. \tag{4.32}$$

The energy content of the primary and secondary batteries are read from the datasheet as,

$$E_{\text{mv}} = 59\,940\,\text{J}, \quad E_{\text{fb}} = 87\,912\,\text{J}. \tag{4.33}$$

Now we follow the steps as described in Section 4.2. We start by computing the power consumption of the flying battery in hover,

$$p_{\text{fb}} = 199.05\,\text{W} \tag{4.34}$$

The power consumption of the main vehicle in the docked configuration, and while rejecting the downwash of the flying battery is approximately,

$$p_{\text{mv,docked}} = 184.41\,\text{W}. \tag{4.35}$$

The upper bound of the energy consumption of the flying battery to power itself is,

$$E_{\text{fb,self}} = 7066.28\,\text{J}. \tag{4.36}$$

The upper bound of the energy consumption of the main vehicle when using the primary battery is,

$$E_{\text{mv,self}} = 6546.56\,\text{J}. \tag{4.37}$$

Clearly, the first constraint (4.10) is satisfied. We keep a high safety factor here, to account for the situation in which no flying battery comes to dock with the main vehicle. In this case, we want enough energy in the primary battery to either wait for another flying battery to come and dock with it, or land at an appropriately safe location.

The efficiency of the battery charging circuit is calculated from experiments to be $\eta_{\text{rech}} = 0.87$. With this, the amount of time a flying battery can power the main vehicle can be calculated from (4.11),

$$t_{\text{mv,docked}} = 397.6\,\text{s} = 6.63\,\text{min}. \tag{4.38}$$

The minimum recharging rate from the second constraint is calculated to be,

$$p_{\text{rech}} \geq 18.93\,\text{W}. \tag{4.39}$$

As mentioned in Section 4.5 we set the charging current to 2.0 A. Given that we are using a 3S battery which is at 11.1 V on average, this gives us an average charging power of $p_{\text{rech}} = 22.20\,\text{W}$, which satisfies the constraint to obtain unlimited flight time. The safety factor here is 1.17, to account for a slightly longer time to dock in a worst-case scenario. Note that the safety factor for a real-world system would have to be higher to account for higher uncertainty in the docking time, etc.

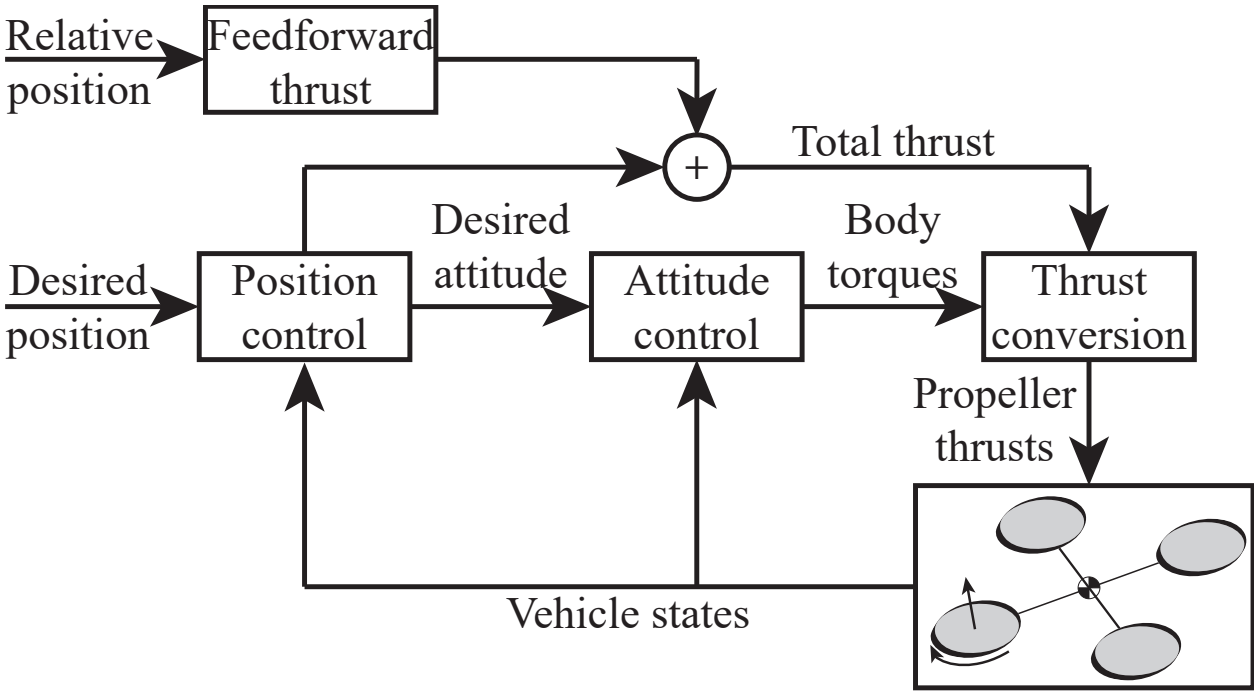

Figure 4.11: Block diagram of the aerial vehicle controller. The flying battery does not have the feedforward thrust component.

Flight experiment setup

The vehicles used in our experiments are localized via sensor fusion of a motion capture system and an onboard rate gyroscope. Experimental data from the motion capture system, voltage sensors, and current sensor are logged via radio for post-processing.

Revisiting the measurement model from Section 4.4, in our case the vehicle pose measurements are coming from a motion-capture system which measures the position and attitude of the vehicles. Note that if we use an onboard sensing scheme (e.g. [39]), the measurement model would change because the system will be measuring and estimating relative states instead of absolute states like we do with the motion-capture system. However, the stochastic docking model would still be valid. We emphasize that in this work, our objective is to develop the design tool to choose the system parameters by modeling the probability of success as a function of the system parameters and uncertainty, and show that we can design a system with a desired probability of mission success, which has no limit on endurance due to energy storage constraints. Hence, we evaluate and instantiate this system with the motion-capture system being used for localization to prove that unlimited endurance and range is possible for an eVTOL.

We control the vehicles using a cascaded PID position and attitude controller shown in Figure 4.11. The integral action on the position and yaw helps prevent steady state errors and ensures that the vehicles are correctly vertically aligned. Additionally, feedforward thrust for the main vehicle to reject aerodynamic disturbances is directly added to the total thrust based on the relative location of the flying battery with respect to the main vehicle.

Aerodynamic disturbance rejection

We use the following key results from [38] and Appendix B:

1. The effect of mutual aerodynamic disturbances is primarily seen on the quadcopter that flies lower. The quadcopter that flies above is negligibly affected.

2. The predominant component of the aerodynamic forces is along the direction of the downwash. Forces perpendicular to the direction of the downwash can be ignored.

3. The aerodynamic torques disturb the bottom quadcopter in a way that tends to vertically align it with the top quadcopter. This is advantageous in our maneuver. Hence, we do not attempt to reject the torques.

We chose to fly the flying battery above the main quadcopter owing to result (1). The main quadcopter has sufficient thrust capacity to reject the disturbances caused by the flying battery's airflow. Based on results (2) and (3), the only disturbance that we correct for is the vertical force. This is done by applying a feedforward thrust based on the relative location of the two quadcopters.

The feedforward thrust map is created by flying the two quadcopters at various relative separations. A PID controller is used for position control which outputs a desired total thrust force. The feedforward thrust map is created from previous runs' controller integral actions, specifically creating a map of the required feedforward force for different positions.

Demonstration

To demonstrate the ability and flight time benefit of our design, we conduct the following experiment:

1. The main vehicle takes off with a fully charged primary battery and hovers at a specific desired position.

2. A fully charged flying battery is commanded to dock on the main vehicle.

3. Once docked, the main vehicle switches its power source to the secondary battery and continues hovering. The secondary battery also recharges the primary battery in this phase.

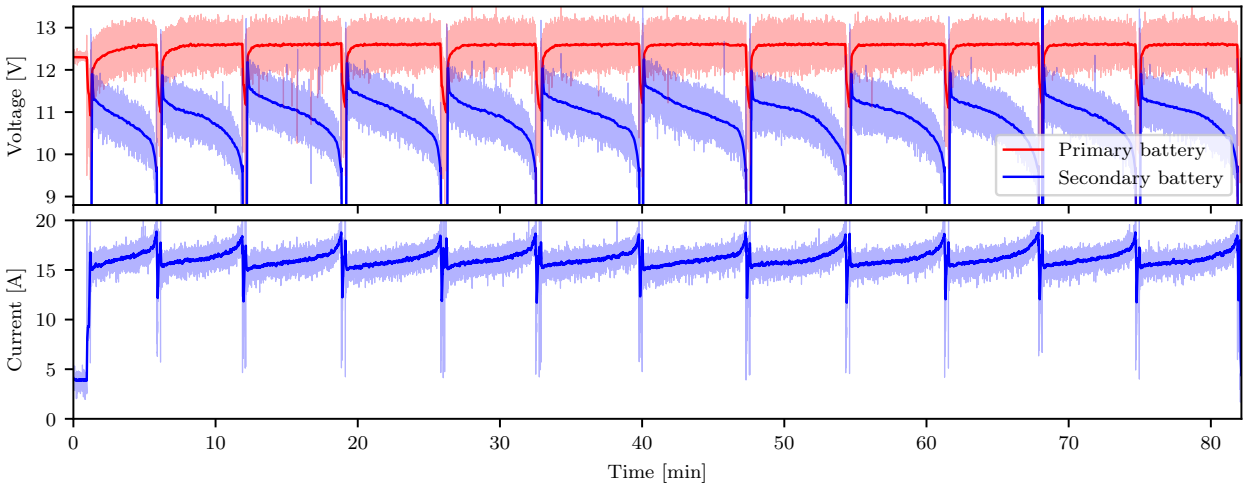

Figure 4.12: Voltage of primary and secondary battery, and current consumption vs. time for the main vehicle. Faint lines show the raw data and filtered data is plotted as dark lines for ease of visualization. Figure 4.13 shows a zoomed-in version of one flying battery discharge cycle.

4. Once the secondary battery is completely discharged, the main vehicle switches back to the primary battery.

5. The flying battery is commanded to undock and land. Simultaneously, another fully charged flying battery takes off.

6. The second flying battery docks on the main vehicle and we again switch the power source to the secondary battery.

7. During this period, we manually replace the discharged flying battery with a fully charged one.

8. This process is repeated until the desired mission is completed. In our case, we choose the mission to be a hovering flight of 80 min, to have enough number of flying batteries docking, powering the main vehicle, and undocking, to establish the reliability of the system.

Figure 4.9 shows steps (4)-(6) of the procedure. Note that the hovering time of the main vehicle flying alone without the flying batteries is 9.36 min.

The footage from the long-duration flight experiment can be seen in the video attachment.

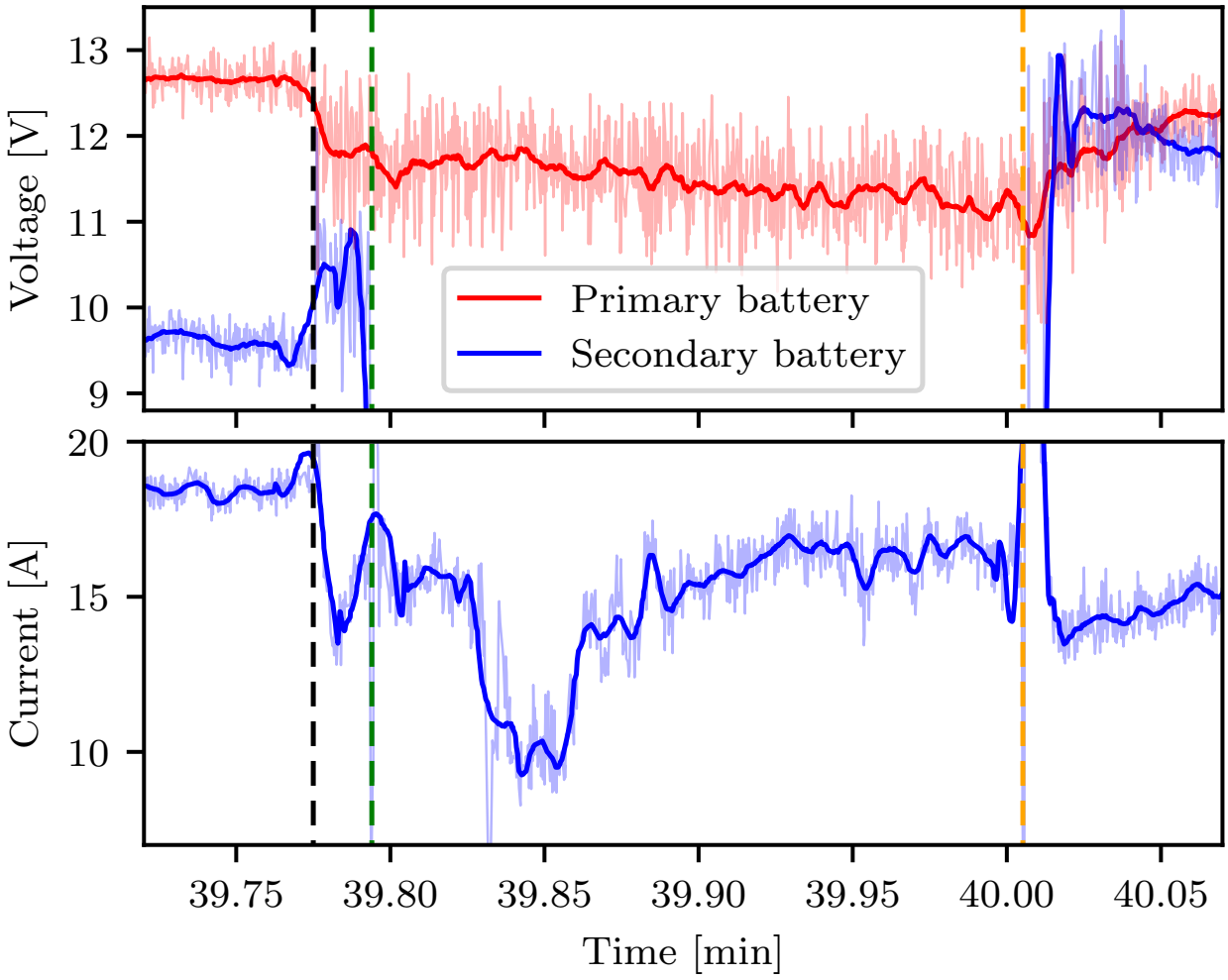

Figure 4.13: Zoomed version of Figure 4.12 showing the primary and secondary battery voltage, and current consumption of the main vehicle during undocking and docking. Dotted lines mark the following events: (i) black: main vehicle switches to primary battery, (ii) green: flying battery undocks, (iii) orange: another flying battery docks. Note how the (raw) voltage reading of the secondary battery drops to zero between (ii) and (iii). This is because the secondary battery voltage sensor is onboard the main vehicle, and there is no docked flying battery for this duration.

Discussion

The plots of input voltage and current vs. time of the main vehicle for the duration of the entire demonstration are shown in Figure 4.12. We see the characteristic LiPo battery discharge curve [69] several times in the voltage vs. time plot. Each shows the complete energy consumption of one secondary battery. The current vs. time plot shows that current input to the vehicle increases as the voltage decreases. This is expected because the power consumption of the vehicle must remain approximately constant to hover continuously.

A typical cycle of undocking, docking, and flying battery discharge, is shown in Figure 4.13. We see that when the main vehicle switches back to the primary battery, the primary battery voltage reading drops due to a voltage drop across the internal resistance of the battery and the resistance of the circuit. After one second of switching to the primary battery, the flying battery undocks. The secondary battery voltage reading drops to zero during this phase. The flying battery moves out and lands. In this part, the main vehicle is flying without any additional mass or aerodynamic disturbance forces and hence we observe a dip in the current and power consumption. A few seconds later, another fully charged flying battery flies on top of the main vehicle and begins descending to dock. We observe an increase in power consumption because of aerodynamic disturbance rejection. Lastly, the flying battery docks on the main vehicle. The secondary battery voltage reading jumps to about 12.6 V, which is the fully charged voltage of a 3S battery. The main vehicle switches to start consuming the secondary battery and recharge the primary battery over a period of approximately 6.5 min. After the flying battery is nearly fully discharged (except for the reserve charge for the flying battery to undock and land), the main vehicle switches back to the primary battery, and the cycle repeats. The observed flight time in the docked configurations over several trials has an average of 385.9 s with a standard deviation of 41.2 s, which matches well with the predicted flight time of 397.6 s.

The reliability of the docking contact under maneuvering, as analyzed in Appendix A, was tested by flying the main vehicle with the flying battery in an oscillating motion with peak lateral accelerations of $12\,\mathrm{m\,s^{-2}}$ and peak roll angles of 50° without losing contact. This is shown in the video attachment.

The flying battery concept is thus validated by flying the main vehicle for our desired mission duration (chosen to be 80 min for the sake of demonstration), and showing that the primary battery is nearly fully charged at the end of the mission. This ability of unlimited flight time comes without increasing the mass of the main vehicle by a huge factor, resulting in a safer, more useful vehicle.

4.7 Conclusion

In this chapter, we have introduced the concept and design of flying batteries – a small aerial vehicle that can carry a secondary battery for a main vehicle, dock on it, allow it to switch its power supply from the primary battery to the secondary battery and back, recharge the

primary battery, and undock from it.

We presented an analysis for the flight time of a single eVTOL, and an eVTOL using flying batteries for hovering flight, and explored power and energy constraints that need to be satisfied in order to enable unlimited endurance for an eVTOL aircraft.

A systematic approach based on a stochastic model was explored to choose the radius of forgiveness of the docking platform and the cutoff height for dropping, to maximize the probability of success of docking.

A mid-air docking mechanism using no active components was designed in the form of docking legs on the flying battery which mate with a docking platform on the main quadcopter, with parameters derived from the stochastic docking model. A custom circuit was designed to seamlessly switch the power source of the main vehicle in-flight, and recharge its primary battery. This was achieved using diodes to avoid batteries rapidly discharging into each other, a relay to turn the primary supply off or on, spring-loaded connectors and copper plates for electrical connection to draw power from the secondary battery, and a battery charging board that takes input from the flying battery and delivers output to the primary battery.

An empirical model was utilized to provide a feedforward thrust from the main vehicle to reject the aerodynamic disturbance forces due to the downwash of the flying battery.

Lastly, we demonstrated the ability of the system to dock, switch power sources, recharge the primary battery, and undock multiple times in a single flight in an indoor flight experiment using a motion-capture system for localization. This unlocked the potential to fly the main vehicle for an unlimited duration. We specifically demonstrated a 80 min flight which is about 8.5× the solo flight time of the main vehicle and showed that the primary battery is nearly fully charged at the end of the flight implying that the main vehicle can keep hovering for as long as it desires.

We would like to highlight that in this system, nearly all of the energy for hovering comes from the flying batteries. The primary battery onboard the main vehicle is only to power the main vehicle during the time when we are switching from one flying battery to another, or in emergency situations where a flying battery is not available and it needs to land. This is the salient feature of the system – the power for the main vehicle comes from batteries that are detachable so that the system is not carrying any dead weight of discharged batteries, and the discharged portion is always replaceable with a charged one. Essentially, *this is a battery swapping system, where the swapping is done by ejecting a discharged flying battery (which can safely land with its reserves) and docking a fully charged flying battery.*

All of this is done while keeping the main vehicle in essentially the same safety class. This can be extremely useful in, for example, emergency deliveries where the delivery aerial vehicle cannot afford to land, or in urban aerial mobility applications that require a long-distance flight.

Future Work

An extension to this work would be to analyze the tradeoff between the probability of success of docking and the mass of the docking platform. Both the parameters increase with increasing radius of forgiveness of the docking platform. However, increased mass implies a higher recharging rate (4.13) required for unlimited flight time, which has an upper limit that depends on the battery.

Another extension would be to only use onboard sensing for the vehicles, rather than relying on an external motion-capture system as done in the demonstrations in this work. Absolute localization may be performed via sensor fusion of an inertial measurement unit and GPS [75]. A camera mounted on the main vehicle and markers pasted on the flying batteries may be used for computer vision-based localization [39, 76, 77] as it offers high precision relative localization suitable for the sensitive docking maneuver.

Chapter 5

Docking two multirotors in midair using relative vision measurements

Modular robots have been rising in popularity for a variety of applications, and autonomous midair docking is a necessary task for real world deployment of these robots. We present a state estimator based on the extended Kalman filter for relative localization of one multirotor with respect to another using only onboard sensors, specifically an inertial measurement unit and a camera-marker pair. Acceleration and angular velocity measurements along with relative pose measurements from a camera on the first multirotor looking at a marker on the second multirotor are used to estimate the relative position and velocity of the first multirotor with respect to the second, and the absolute attitude of the first multirotor. We also present a control architecture to use these onboard state estimates to control the first multirotor at a desired setpoint with respect to the second. The performance of the estimator and control architecture are experimentally validated[1] by successfully and repeatably performing midair docking – a task that requires relative position precision on the order of a centimeter.

The material in this chapter is based on the following work uploaded to arXiv.

- Karan P Jain, Minos Park, and Mark W Mueller. "Docking two multirotors in midair using relative vision measurements". In: *arXiv preprint arXiv:2011.05565* (2020)

5.1 Introduction

Modular and cooperative flying robots have started seeing increasing use in applications such as lifting objects [78, 79], assisting each other such as for flight time extension [37], or demonstrating aesthetic aerial transformation [80]. These multiple small robots offer several advantages over a few larger robots. The individual units are usually simple in design. The failure of a few of these units does not affect the high-level objective, offering redundancy.

[1]The explanation and experimental validation video can be found here: `https://youtu.be/m9YqOm3VtTM`

Lastly, they can move through tight, cluttered spaces easily as individual units and then group up at the desired location.

A critical aspect of having these modular robots to work in real life settings is autonomous assembly and dismantling. For flying robots, this translates to autonomous midair docking and undocking. Current literature explores docking via various methods such as using a robotic arm and winch [71], using magnets [81], or using mechanical structures, [37, 82].

Midair docking is a sensitive task that requires a coarse global localization to roughly get the vehicles close to each other and a fine relative localization for the actual docking task. In this chapter, we focus on the precise relative localization aspect. A combination of inertial measurement units and computer vision based sensors is usually the most popular choice for this task. For example, it has been used for autonomous relative navigation or docking of aircrafts [83, 84], relative position sensing for an underwater vehicle [85], and even considered for docking spacecrafts [86, 87].

In this work, we present a complete 6 degree of freedom (DoF) localization of one multirotor with respect to another, using only onboard sensors. Specifically, we derive a state estimation algorithm based on the extended Kalman filter (EKF) that takes, as input, inertial measurements (acceleration and angular velocity) and relative pose (position and orientation) measurements. These measurements are then used to estimate the relative position and velocity of one multirotor with respect to another, and its absolute attitude with respect to the inertial frame. We also present a control architecture to experimentally validate the relative localization algorithm using an onboard camera on the first quadcopter and a marker (which provides full 6 DoF information on detection) on the second, and control the first quadcopter using just the onboard estimates. Lastly, we successfully demonstrate midair docking using these onboard estimates – a task that requires a position precision on the order of a centimeter. Figure 5.1 shows pictures of two quadcopters during a docking maneuver where the lower quadcopter is using purely onboard sensing.

The chapter is organized as follows. Section 5.2 covers basic multirotor dynamics and the architecture of our control system. In Section 5.3, we derive the equations for the relative state estimation algorithm using the EKF formulation. Section 5.4 explains the design and selection of various hardware components used in our experiments. Lastly, in Section 5.5, we experimentally validate the state estimator and present results from successful midair docking experiments.

5.2 System Dynamics and Architecture

In this section, we briefly describe the dynamics of a multirotor, and provide details about the architecture of the system. We introduce the relevant states of the system and their governing equations, and how we can use onboard sensors to estimate these states. The dynamics that we show here are specific to a multirotor, but the estimation algorithm that we present is indifferent to these dynamics and can be applied to any aerial vehicle.

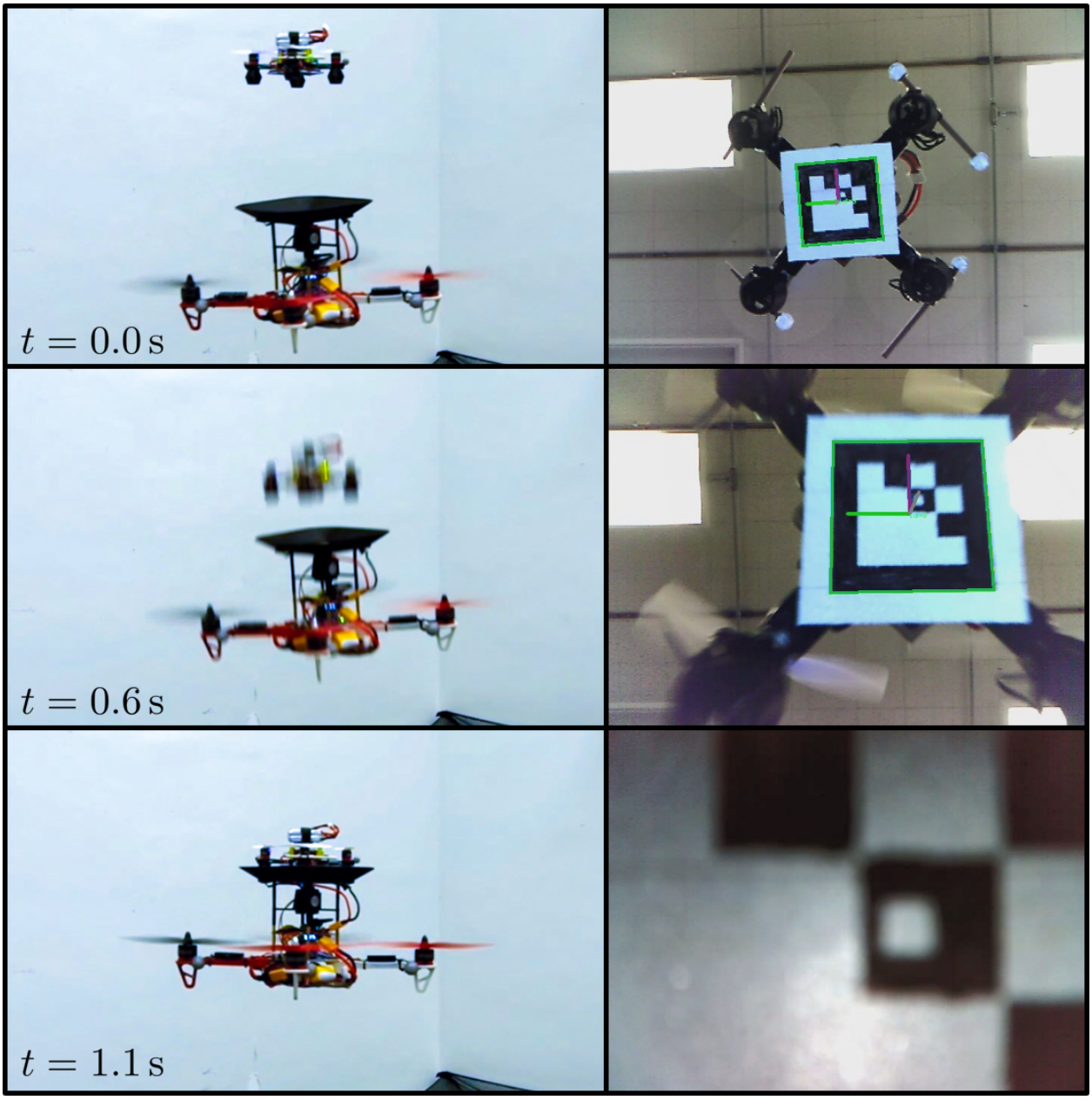

Figure 5.1: Offboard (left) and onboard (right) sequence of images of the docking procedure. From top to bottom: (i) the two quadcopters flying in proximity; (ii) passive quadcopter is commanded to stop its motors to dock since it is within docking range; (iii) the two quadcopters are docked.

Notation

We represent scalars with non-bold symbols such as m, vectors with lowercase bold symbols such as $\mathbf{g}$, and matrices with uppercase bold symbols such as $\mathbf{R}$. A vector $\mathbf{v}$ in a certain frame F is denoted by $\mathbf{v}^{\mathrm{F}}$.

One can go from any frame to any other frame via a rigid body transformation – a rotation and a translation. Rotations from frame F_1 to frame F_2 are represented by the rotation matrix $\mathbf{R}^{\mathrm{F}_2\mathrm{F}_1}$. To transform a vector from one frame to another, the following relation is used

$$\mathbf{v}^{\mathrm{F}_2} = \mathbf{R}^{\mathrm{F}_2\mathrm{F}_1}\mathbf{v}^{\mathrm{F}_1}. \tag{5.1}$$

The displacement vector going from origin of frame F_1 to origin of frame F_2 is given by $\mathbf{s}_{\mathrm{F}_2\mathrm{F}_1}$. This vector can be represented in any frame of our choice, say F, as $\mathbf{s}^{\mathrm{F}}_{\mathrm{F}_2\mathrm{F}_1}$.

Quadcopter Dynamics

A typical multirotor can be modeled as a rigid body with six degrees of freedom. The body-fixed frame is denoted by Q. The inertial frame of reference (or Earth frame) is denoted by E. The position, velocity, and acceleration of this multirotor with respect to the inertial frame are denoted by $\mathbf{s}_{\mathrm{QE}}, \dot{\mathbf{s}}_{\mathrm{QE}}, \ddot{\mathbf{s}}_{\mathrm{QE}} \in \mathbb{R}^3$.

The attitude of the multirotor is represented by the rotation matrix $\mathbf{R}^{\mathrm{EQ}} \in \mathrm{SO}(3)$. It evolves as a function of the angular velocity $\boldsymbol{\omega}^{\mathrm{Q}}$ and angular acceleration $\dot{\boldsymbol{\omega}}^{\mathrm{Q}}$,

$$\dot{\mathbf{R}}^{\mathrm{EQ}} = \mathbf{R}^{\mathrm{EQ}}\mathbf{S}(\boldsymbol{\omega}^{\mathrm{Q}}) \tag{5.2}$$

where $\mathbf{S}(\cdot)\colon \mathbb{R}^3 \to \mathfrak{so}(3)$ produces the skew-symmetric form of the vector argument, and $\mathfrak{so}(3)$ represents the Lie algebra of the rotation group. Specifically, if $\mathbf{a} = (a_1, a_2, a_3)$ then

$$\mathbf{S}(\mathbf{a}) = \begin{bmatrix} 0 & -a_3 & a_2 \\ a_3 & 0 & -a_1 \\ -a_2 & a_1 & 0 \end{bmatrix}. \tag{5.3}$$

The external forces and torques acting on the system directly relate to the translational and rotational accelerations, and can be expressed via the Newton-Euler equations,

$$\begin{aligned} \ddot{\mathbf{s}}_{\mathrm{QE}} &= \frac{\mathbf{f}}{m_{\mathrm{Q}}} + \mathbf{g} \\ \dot{\boldsymbol{\omega}}^{\mathrm{Q}} &= \mathbf{J}_{\mathrm{Q}}^{-1}\left(\boldsymbol{\tau}^{\mathrm{Q}} - \mathbf{S}(\boldsymbol{\omega}^{\mathrm{Q}})\mathbf{J}_{\mathrm{Q}}\boldsymbol{\omega}^{\mathrm{Q}}\right) \end{aligned} \tag{5.4}$$

where $m_{\mathrm{Q}}, \mathbf{J}_{\mathrm{Q}}$ are the multirotor's mass and (body-fixed) moment of inertia respectively, $\mathbf{f}$ is the sum of forces acting on the multirotor (except weight due to gravity $\mathbf{g}$), and $\boldsymbol{\tau}^{\mathrm{Q}}$ is the sum of external torques acting on the vehicle (expressed in the multirotor's frame).

The total force $\mathbf{f}$ can be broken down into the propeller forces $\mathbf{f}_p$ and disturbance forces $\mathbf{f}_d$. Similarly, the total torques $\boldsymbol{\tau}$ are a result of moments produced by the propellers $\boldsymbol{\tau}_p$ and

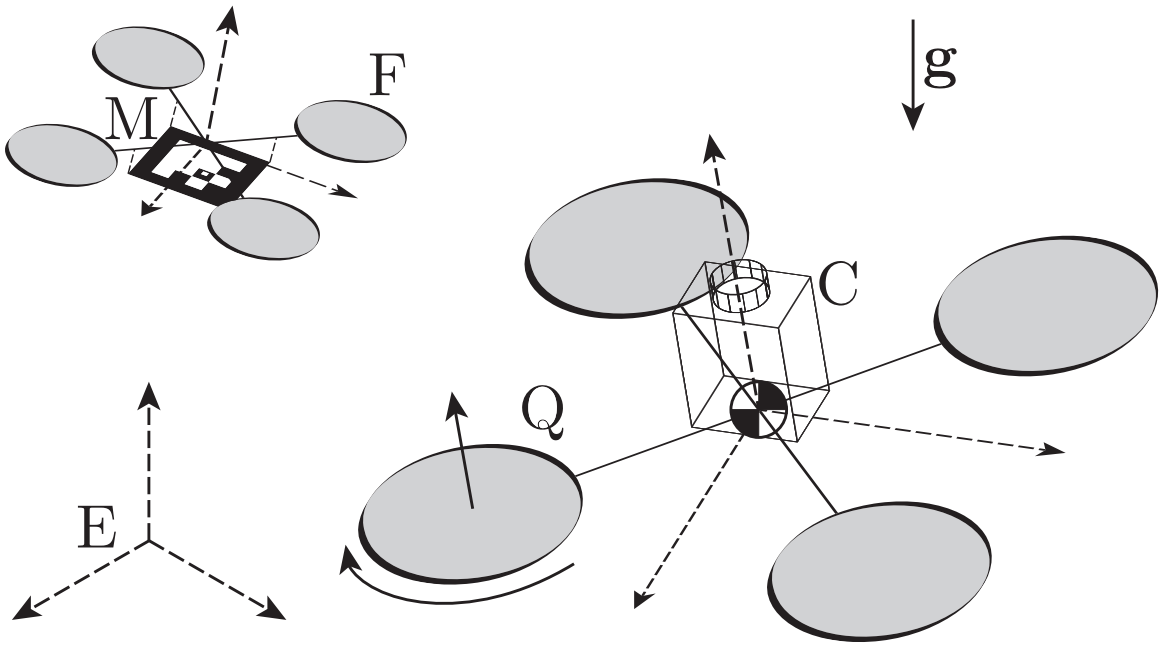

Figure 5.2: Schematic of a docking flight and relevant reference frames

disturbance torques $\boldsymbol{\tau}_d$. The disturbance forces and torques are usually hard to characterize and heavily depend upon the application in which the multirotor is being used. They might also come up due to modeling errors, aerodynamic effects, misaligned actuators, among other factors. In our case, we have two multirotors flying in proximity which results in aerodynamic interference as analyzed in [38].

System Architecture

We describe the estimation and control architecture for docking two quadcopters midair using relative pose measurements from a camera looking at a marker. We have a "passive" quadcopter which is supposed to hover in one place, carrying a marker with it that can be seen by the "active" quadcopter. The active quadcopter carries a camera and its objective is to localize itself with respect to the passive quadcopter so that it can dock with it. Figure 5.2 shows a diagram of a typical flight during midair docking, along with all the frames of reference.

There are five frames of interest – the inertial or Earth-fixed frame E, the frame fixed to the active quadcopter Q, the camera frame (mounted on the active quadcopter) C, the frame fixed to the passive quadcopter F, and the marker frame (pasted on the passive quadcopter) M.

Whenever the passive quadcopter's marker is not in the Field of View (FoV) of the active quadcopter's camera, both the quadcopters are localized using sensor fusion of a motion capture system and an onboard rate gyroscope [35].

When the marker appears in the camera's FoV, we manually switch the active quadcopter to only use onboard sensing – inertial measurements from an IMU and relative pose from vision. The active quadcopter also rejects aerodynamic disturbances from the passive quadcopter's airflow by generating an additional thrust calculated from a feedforward map based on its relative position from the passive quadcopter. The docking maneuver used is as presented in [37]. The passive quadcopter continues using offboard sensing (from motion capture) for localization. A block diagram for the described sensing and control scheme is shown in Figure 5.3.

5.3 Relative State Estimation

For estimation and control during midair docking, the states that we need to estimate are the relative position and velocity of the active quadcopter with respect to the passive quadcopter, and the absolute attitude of the active quadcopter. So the states that we are interested in are $\mathbf{s}^{\mathrm{E}}_{\mathrm{QF}}, \dot{\mathbf{s}}^{\mathrm{E}}_{\mathrm{QF}}, \mathbf{R}^{\mathrm{EQ}}$. We follow the approach shown in [88] to derive the prediction and measurement update steps.

Prediction model

We use the inertial measurements from the active quadcopter's IMU to predict the states forward in time. Specifically, our estimator does not use the Newton-Euler equations of dynamics (5.4). This makes the estimator agnostic to the dynamics of the vehicles, and can work without the knowledge of unknown disturbance forces and torques.

Symbols with a tilde denote measurements. The accelerometer measures the proper acceleration of the vehicle, and the measurement $\widetilde{\mathbf{a}}$ is related to the vehicle's acceleration in the inertial frame as,

$$\widetilde{\mathbf{a}} = (\mathbf{R}^{\mathrm{EQ}})^{-1} \left(\ddot{\mathbf{s}}^{\mathrm{E}}_{\mathrm{QE}} - \mathbf{g}^{\mathrm{E}} \right) + \boldsymbol{\nu}_{\mathbf{a}} \tag{5.5}$$

where $\boldsymbol{\nu}_{\mathbf{a}}$ denotes the sensor noise. We assume that the accelerometer is located at the vehicle's center of mass, so the measurement is unaffected by the vehicle's rotational motion.

The rate gyroscope measurement $\widetilde{\boldsymbol{\omega}}$ is given as,

$$\widetilde{\boldsymbol{\omega}} = \boldsymbol{\omega}^{\mathrm{Q}} + \boldsymbol{\nu}_{\boldsymbol{\omega}} \tag{5.6}$$

where $\boldsymbol{\nu}_{\boldsymbol{\omega}}$ represents the sensor noise.

From the above equations, we derive the following,

$$\begin{aligned} \ddot{\mathbf{s}}^{\mathrm{E}}_{\mathrm{QE}} &= \mathbf{R}^{\mathrm{EQ}} \widetilde{\mathbf{a}} + \mathbf{g}^{\mathrm{E}} - \mathbf{R}^{\mathrm{EQ}} \boldsymbol{\nu}_{\mathbf{a}} \\ \boldsymbol{\omega}^{\mathrm{Q}} &= \widetilde{\boldsymbol{\omega}} - \boldsymbol{\nu}_{\boldsymbol{\omega}} \end{aligned} \tag{5.7}$$

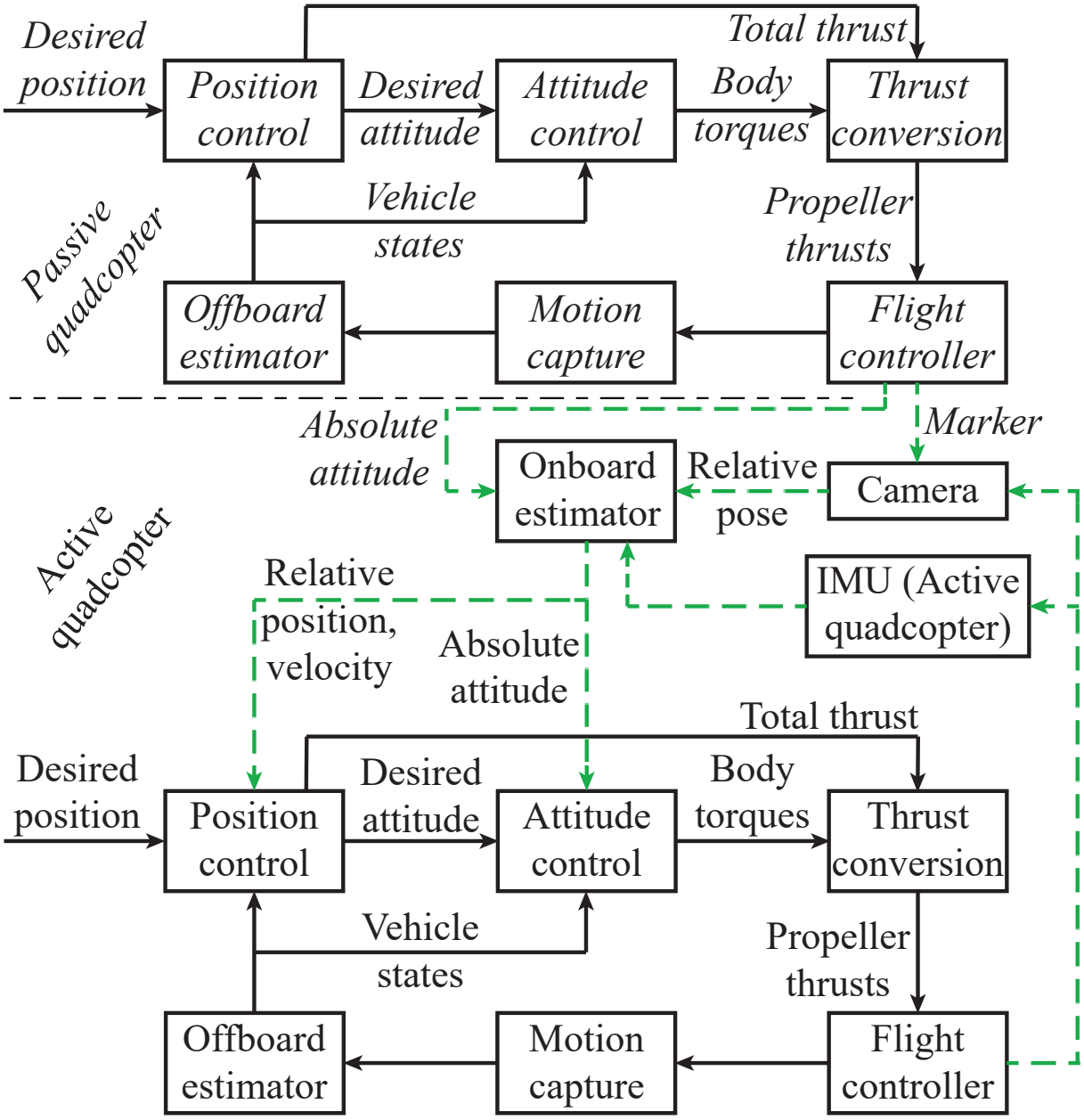

Figure 5.3: Control block diagram for the two quadcopters. All associations with the passive quadcopter are italicized. Black (solid) flow lines show the estimation and control scheme for both quadcopters using offboard sensing. Green (dashed) lines show the estimation scheme for the active quadcopter using onboard sensing, when the marker is in the FoV of the camera.

which are used in the prediction step of the estimation.

The accelerometer and rate gyroscope are assumed to output regular measurements at high frequencies.

Measurement model

The camera (C) is mounted rigidly on the active quadcopter (Q) and the marker (M) is pasted on the passive quadcopter (F). Therefore, the quantities $\mathbf{R}^{\mathrm{CQ}}$, $\mathbf{R}^{\mathrm{MF}}$, $\mathbf{s}^{\mathrm{C}}_{\mathrm{QC}}$, and $\mathbf{s}^{\mathrm{F}}_{\mathrm{FM}}$ are fixed and known from the design.

Whenever the camera has the marker in its FoV, it outputs a relative position and orientation measurement of the marker with respect to the camera. This can be written as a function of known quantities and system states as,

$$\widetilde{\mathbf{s}^{\mathrm{C}}_{\mathrm{MC}}} = -\mathbf{R}^{\mathrm{CQ}}(\mathbf{R}^{\mathrm{EQ}})^T \left(\mathbf{s}^{\mathrm{E}}_{\mathrm{QF}} + \mathbf{R}^{\mathrm{EF}}\mathbf{s}^{\mathrm{F}}_{\mathrm{FM}}\right) + \mathbf{s}^{\mathrm{C}}_{\mathrm{QC}} + \boldsymbol{\nu}_{\mathbf{s}} \tag{5.8}$$

$$\widetilde{\mathbf{R}^{\mathrm{MC}}} = \mathbf{R}^{\mathrm{MF}}(\mathbf{R}^{\mathrm{EF}})^T\mathbf{R}^{\mathrm{EQ}}\mathbf{R}^{\mathrm{QC}}\exp(\mathbf{S}(\boldsymbol{\nu}_{\mathbf{R}})) \tag{5.9}$$

where $\boldsymbol{\nu}_{\mathbf{s}}$ is the noise in relative position measurement, and $\boldsymbol{\nu}_{\mathbf{R}}$ is the noise rotation vector [89] for relative attitude measurement. The operation $\exp(\cdot) : \mathfrak{so}(3) \to \mathrm{SO}(3)$ is the matrix exponential, and takes any element in the Lie algebra of the rotation group to the rotation group (SO(3)) itself.

The relative pose measurements from the camera are available at a lower frequency than the inertial measurements. The availability of these measurements is capped at the camera's frame rate, and also depends on marker detection which might be irregular.

EKF implementation

Following the method shown in [90], we implement the extended Kalman filter (EKF) with a nine-dimensional state vector. All estimated states' symbols are denoted with a hat. The state vector consists of the active quadcopter's relative position $\widehat{\mathbf{s}^{\mathrm{E}}_{\mathrm{QF}}}$ and relative velocity $\widehat{\dot{\mathbf{s}}^{\mathrm{E}}_{\mathrm{QF}}}$ with respect to the passive quadcopter, and a three-dimensional representation of the absolute attitude error $\widehat{\boldsymbol{\delta}^{\mathrm{EQ}}}$, along with a reference orientation $\widehat{\mathbf{R}^{\mathrm{EQ}}_{\mathrm{ref}}}$. The resulting attitude is computed using,

$$\widehat{\mathbf{R}^{\mathrm{EQ}}} = \widehat{\mathbf{R}^{\mathrm{EQ}}_{\mathrm{ref}}}\exp\left(\mathbf{S}\left(\widehat{\boldsymbol{\delta}^{\mathrm{EQ}}}\right)\right) \tag{5.10}$$

For convenience of notation, we will represent the states as $\left(\widehat{\mathbf{s}^{\mathrm{E}}_{\mathrm{QF}}}, \widehat{\dot{\mathbf{s}}^{\mathrm{E}}_{\mathrm{QF}}}, \widehat{\boldsymbol{\delta}^{\mathrm{EQ}}}\right) = \left(\widehat{\mathbf{p}}, \widehat{\mathbf{v}}, \widehat{\boldsymbol{\delta}}\right)$. The estimated states are predicted forward in time using,

$$\widehat{\mathbf{p}}_p(t+\Delta t) = \widehat{\mathbf{p}}(t) + \widehat{\mathbf{v}}(t)\Delta t \tag{5.11}$$

$$\widehat{\mathbf{v}}_p(t+\Delta t) = \widehat{\mathbf{v}}(t) + \left(\widehat{\mathbf{R}^{\mathrm{EQ}}_{\mathrm{ref}}}(t)\exp\left(\mathbf{S}\left(\widehat{\boldsymbol{\delta}}(t)\right)\right)\widetilde{\mathbf{a}}(t) + \mathbf{g}^{\mathrm{E}}\right)\Delta t \tag{5.12}$$

$$\widehat{\boldsymbol{\delta}}_p(t+\Delta t) = \widehat{\boldsymbol{\delta}}(t) + \left(\widetilde{\boldsymbol{\omega}}(t) - \tfrac{1}{2}\mathbf{S}(\widetilde{\boldsymbol{\omega}}(t))\widehat{\boldsymbol{\delta}}(t)\right)\Delta t \tag{5.13}$$

where the IMU data is assumed to be constant over the sampling time Δt. Note that the attitude error is set to zero after each step, which makes (5.13) valid.

The covariance of the estimated state $\mathbf{P}_{\mathbf{xx}} \in \mathbb{R}^{9\times 9}$ is updated using the standard EKF equations,

$$\mathbf{P}_{\mathbf{xx},p}(t+\Delta t) = \mathbf{A}(t)\mathbf{P}_{\mathbf{xx}}(t)\mathbf{A}(t)^T + \mathbf{W} \tag{5.14}$$

where the matrix $\mathbf{A}(t)$ is given by,

$$\mathbf{A}(t) = \begin{bmatrix} \mathbf{I} & \mathbf{I}\Delta t & \mathbf{0} \\ \mathbf{0} & \mathbf{I} & \mathbf{S}\Big(\widehat{\mathbf{R}^{\text{EQ}}_{\text{ref}}}(t)\widetilde{\mathbf{a}}(t)\Big)\Delta t \\ \mathbf{0} & \mathbf{0} & \mathbf{I} - \frac{1}{2}\mathbf{S}(\widetilde{\boldsymbol{\omega}}(t))\Delta t \end{bmatrix} \tag{5.15}$$

where $\mathbf{I}$ is the identity matrix and $\mathbf{W} = \text{diag}(\mathbf{0}, \sigma^2_{\mathbf{a}}\mathbf{I}, \sigma^2_{\boldsymbol{\omega}}\mathbf{I})$ consists the (isotropic) noise variances of the accelerometer and rate gyroscope respectively.

We set $t \leftarrow t + \Delta t$ for the remainder of the section for ease of notation. We perform a post-prediction update to the state and covariance to reset the attitude error state to zero,

$$\begin{aligned} \widehat{\mathbf{x}}_{p_+}(t) &= (\widehat{\mathbf{p}}_p(t), \widehat{\mathbf{v}}_p(t), \mathbf{0}) \\ \widehat{\mathbf{R}^{\text{EQ}}_{\text{ref}}}_{p_+}(t) &= \widehat{\mathbf{R}^{\text{EQ}}_{\text{ref}}}(t)\exp\Big(\mathbf{S}\Big(\widehat{\boldsymbol{\delta}}_p(t)\Big)\Big) \\ \mathbf{P}_{\mathbf{xx},p_+}(t) &= \mathbf{T}\Big(\widehat{\boldsymbol{\delta}}_p(t)\Big)\mathbf{P}_{\mathbf{xx},p}(t)\Big(\mathbf{T}\Big(\widehat{\boldsymbol{\delta}}_p(t)\Big)\Big)^T \end{aligned} \tag{5.16}$$

where, to keep the covariance aligned with the reference attitude, we use

$$\mathbf{T}(\boldsymbol{\delta}) = \text{diag}\left(\mathbf{I}, \mathbf{I}, \exp\left(-\tfrac{1}{2}\mathbf{S}(\boldsymbol{\delta})\right)\right). \tag{5.17}$$

We then set $\widehat{\mathbf{x}}(t) = \widehat{\mathbf{x}}_{p_+}(t)$, $\widehat{\mathbf{R}^{\text{EQ}}_{\text{ref}}}(t) = \widehat{\mathbf{R}^{\text{EQ}}_{\text{ref}}}_{p_+}(t)$, and $\mathbf{P}_{\mathbf{xx}}(t) = \mathbf{P}_{\mathbf{xx},p_+}(t)$. If a relative pose measurement is available, we use the standard EKF formalism [91] to perform the measurement update. We assume that the absolute attitude of the passive quadcopter $\mathbf{R}^{\text{EF}}$ is given to us.

We use (5.8) and (5.9) to derive the update equations. We define a reference relative orientation,

$$\widehat{\mathbf{R}^{\text{MC}}_{\text{ref}}} = \mathbf{R}^{\text{MF}}(\mathbf{R}^{\text{EF}})^T\widehat{\mathbf{R}^{\text{EQ}}_{\text{ref}}}(\mathbf{R}^{\text{CQ}})^T \tag{5.18}$$

which is essentially, our best guess for the relative orientation measurement that we would get.

We now write the actual relative orientation measurement in terms of the reference measurement, and an attitude measurement error vector $\widetilde{\boldsymbol{\sigma}}$ (which contains measurement noise) as,

$$\widetilde{\mathbf{R}^{\text{MC}}} = \widehat{\mathbf{R}^{\text{MC}}_{\text{ref}}}\exp(\mathbf{S}(\widetilde{\boldsymbol{\sigma}})) \tag{5.19}$$

We substitute (5.9) and (5.18) in (5.19) to write,

$$\begin{aligned} \exp(\mathbf{S}(\widetilde{\boldsymbol{\sigma}})) &= \mathbf{R}^{\text{CQ}}\exp(\mathbf{S}(\boldsymbol{\delta}))(\mathbf{R}^{\text{CQ}})^T\exp(\mathbf{S}(\boldsymbol{\nu}_{\mathbf{R}})) \\ &= \exp(\mathbf{S}(\mathbf{R}^{\text{CQ}}\boldsymbol{\delta}))\exp(\mathbf{S}(\boldsymbol{\nu}_{\mathbf{R}})) \end{aligned} \tag{5.20}$$

Note that the above is an exact expression, but cannot be simplified further. We linearize it about $\boldsymbol{\delta} = \mathbf{0}$, and $\boldsymbol{\nu}_{\mathbf{R}} = \mathbf{0}$,

$$\widetilde{\boldsymbol{\sigma}} = \mathbf{R}^{\mathrm{CQ}}\boldsymbol{\delta} + \boldsymbol{\nu}_{\mathbf{R}} \tag{5.21}$$

We consider $\widetilde{\boldsymbol{\sigma}}$ as our measurements which can be derived from the actual relative orientation measurement and the reference value from (5.19) as,

$$\widetilde{\boldsymbol{\sigma}}(t) = \mathrm{rot}^{-1}\Big(\widehat{\mathbf{R}^{\mathrm{MC}}_{\mathrm{ref}}}^{T}(t)\ \widetilde{\mathbf{R}^{\mathrm{MC}}}(t)\Big) \tag{5.22}$$

where $\mathrm{rot}^{-1}(\cdot)\colon \mathrm{SO}(3) \to \mathbb{R}^3$ is an operation that takes a rotation group element as input and outputs the corresponding rotation vector [89] for that element. It is the inverse of the $\exp(\mathbf{S}(\cdot))$ operation.

The EKF equations are derived by linearizing the measurements with respect to the state,

$$\begin{aligned}\mathbf{H}(t) &= \frac{\partial\begin{bmatrix}\widetilde{\mathbf{s}^{\mathrm{C}}_{\mathrm{MC}}}(t)^{T} & \widetilde{\boldsymbol{\sigma}}(t)^{T}\end{bmatrix}^{T}}{\partial \mathbf{x}}\Bigg|_{\mathbf{x}=\widehat{\mathbf{x}}(t)} \\ &= \begin{bmatrix}-\mathbf{R}^{\mathrm{CQ}}\widehat{\mathbf{R}^{\mathrm{EQ}}_{\mathrm{ref}}}^{T}(t) & \mathbf{0} & \mathbf{R}^{\mathrm{CQ}}\widehat{\mathbf{R}^{\mathrm{EQ}}_{\mathrm{ref}}}^{T}(t)\mathbf{S}(\widehat{\mathbf{p}}(t) + \mathbf{R}^{\mathrm{EF}}\mathbf{s}^{\mathrm{F}}_{\mathrm{FM}}) \\ \mathbf{0} & \mathbf{0} & \mathbf{R}^{\mathrm{CQ}}\end{bmatrix}\end{aligned} \tag{5.23}$$

The relative position measurement update is then done as,

$$\begin{aligned}\mathbf{K}(t) &= \mathbf{P}_{\mathbf{xx}}(t)\mathbf{H}(t)^{T}\big(\mathbf{H}(t)\mathbf{P}_{\mathbf{xx}}(t)\mathbf{H}(t)^{T} \\ &\qquad + \mathrm{diag}\left(\boldsymbol{\Sigma}_{\mathbf{s}}, \boldsymbol{\Sigma}_{\mathbf{R}}\right)\big)^{-1} \\ \widehat{\mathbf{x}}_m(t) &= \widehat{\mathbf{x}}(t) + \mathbf{K}(t)\mathbf{e}_m(t) \\ \mathbf{P}_{\mathbf{xx},m}(t) &= \left(\mathbf{I} - \mathbf{K}(t)\mathbf{H}(t)\right)\mathbf{P}_{\mathbf{xx}}(t) \\ \widehat{\mathbf{R}^{\mathrm{EQ}}_{\mathrm{ref}\,m}}(t) &= \widehat{\mathbf{R}^{\mathrm{EQ}}_{\mathrm{ref}}}(t)\end{aligned} \tag{5.24}$$

where $\boldsymbol{\Sigma}_{\mathbf{s}}$ and $\boldsymbol{\Sigma}_{\mathbf{R}}$ are the covariance matrices of relative position measurement and relative orientation measurement, estimated experimentally. The innovation $\mathbf{e}_m(t)$ is given by,

$$\mathbf{e}_m(t) = \begin{bmatrix}\widetilde{\mathbf{s}^{\mathrm{C}}_{\mathrm{MC}}}(t) + \mathbf{R}^{\mathrm{CQ}}\widehat{\mathbf{R}^{\mathrm{EQ}}_{\mathrm{ref}}}^{T}(t)\left(\widehat{\mathbf{p}}(t) + \mathbf{R}^{\mathrm{EF}}\mathbf{s}^{\mathrm{F}}_{\mathrm{FM}}\right) - \mathbf{s}^{\mathrm{C}}_{\mathrm{QC}} \\ \widetilde{\boldsymbol{\sigma}}(t)\end{bmatrix} \tag{5.25}$$

We employ a final correction step to reset the attitude error and update the reference orientation and state covariance,

$$\begin{aligned}\widehat{\mathbf{x}}(t) &= (\widehat{\mathbf{p}}_m(t), \widehat{\mathbf{v}}_m(t), \mathbf{0}) \\ \widehat{\mathbf{R}^{\mathrm{EQ}}_{\mathrm{ref}}}(t) &= \widehat{\mathbf{R}^{\mathrm{EQ}}_{\mathrm{ref}\,m}}(t)\exp\Big(\mathbf{S}\Big(\widehat{\boldsymbol{\delta}}_m(t)\Big)\Big) \\ \mathbf{P}_{\mathbf{xx}}(t) &= \mathbf{T}\Big(\widehat{\boldsymbol{\delta}}_m(t)\Big)\mathbf{P}_{\mathbf{xx},m}(t)\Big(\mathbf{T}\Big(\widehat{\boldsymbol{\delta}}_m(t)\Big)\Big)^{T}\end{aligned} \tag{5.26}$$

The state estimator then continues to absorb the next set of IMU measurements.

5.4 Hardware Design

In this section, we explain the design of the midair docking mechanism, the quadcopters, and the vision system used in our experiments.

Docking mechanism

We use a midair docking mechanism whose design and working has been demonstrated in [37]. This design uses a mechanical guide structure in the form of a docking platform on the active quadcopter, and docking legs on the passive quadcopter as can be seen in Figure 5.1.

Particularly, this mechanism does not use active components which allows for low weight and complexity. It also allows for a margin of error of a few centimeters during the docking process. Lastly, the quadcopters dock vertically aligned with this mechanism. This enables an easy undocking process – the passive quadcopter can do a regular take-off from the docking platform.

Vehicle design

We use Crazyflie 2.0 flight control boards [92] for both quadcopters. Figure 5.1 shows pictures of the two vehicles.

Active quadcopter

The active quadcopter is designed to have sufficient payload capacity to carry useful sensors such as surveillance cameras or environmental sensors. It uses a 3S 2.2 Ah lithium-ion polymer (LiPo) battery to power itself, and weighs 825 g including the battery. Its arm length is 165 mm and it uses propellers of diameter 203 mm. A lightweight camera is mounted on the quadcopter, facing upwards, to allow onboard sensing and localization. The docking platform is stacked on top of the quadcopter, and has a hole in it for the camera to have a clear view.

Passive quadcopter

The passive quadcopter is designed to have enough payload capacity to carry a package of about 150 g. The docking legs are attached below each of the motors to minimize propeller airflow blockage, so that payload capacity is not affected. It uses a 2S 0.8 Ah LiPo battery to power itself, and weighs 160 g including the battery. Its arm length is 58 mm and it uses propellers of diameter 76 mm. It carries a marker that is pasted below its frame which can be detected by a camera.

Vision system

To perform a relative vision-based localization, we require a camera, a marker which can be easily detected by the camera, and an algorithm that can extract position and orientation information from the marker image. For this purpose, we use ArUco marker [93, 94], part of the OpenCV [95] Contrib library. To see and detect the markers, we use a JeVois-A33 Smart Machine Vision Camera [96]. It is light-weight (17 g), has a 60° FoV, and is equipped with an onboard processor which can run the ArUco detection algorithm at 30 Hz.

Since the multirotors fly in proximity during the docking process, it is possible for a part of the marker to go outside the FoV of the camera, due to movements caused by aerodynamic disturbances. When this happens, the algorithm does not detect the marker. To mitigate this, we embed a smaller ArUco marker inside the original marker pasted on the passive quadcopter, which is verified to always remain in the FoV of the camera via repeated docking experiments.

The lighting condition for a camera facing upwards looking at a marker facing downwards are not favorable in indoor or outdoor flight, since light sources are usually on ceilings in indoor environments, and in the sky in outdoor settings. To improve marker detection, retroreflective tape is pasted on the white portions of the marker. An LED is attached near the camera's lens. This enables more robust marker detection because of the retroreflected LED light from the marker.

5.5 Experimental Validation

The feasibility of using relative vision to localize a vehicle with respect to another for a sensitive docking maneuver is verified experimentally. This section covers characterization of sensor noise standard deviations, the overall system setup for the experiments, and finally some results from the docking experiments using relative vision.

Sensor Noise Characterization for EKF

The flight controller on the vehicles has an IMU which returns accelerometer and rate gyroscope data at 500 Hz. We estimate the sensor noise standard deviations for the IMU, $\sigma_{\mathbf{a}}$ and $\sigma_{\boldsymbol{\omega}}$, from in-flight data.

$$\sigma_{\mathbf{a}} = 0.5\,\mathrm{m\,s^{-2}} \quad \text{and} \quad \sigma_{\boldsymbol{\omega}} = 0.1\,\mathrm{rad\,s^{-1}} \tag{5.27}$$

The noise covariance in the relative position and orientation measurements are estimated from static tests where the camera and marker are placed at various fixed positions with respect to each other. The marker side length is 42 mm. The relative orientation noise covariance remained approximately constant for the various separations. The relative position noise covariance was found to be dependent on the distance along the optical axis z between

the camera and the marker. Specifically, the values were estimated to be,

$$\mathbf{\Sigma_s} = \text{diag}\left(0.2^2, 0.2^2, 0.3^2\right)\left(\frac{z}{1.0\,\text{m}}\right)^2 \text{m}^2 \tag{5.28}$$

$$\mathbf{\Sigma_R} = \text{diag}\left(0.35^2, 0.35^2, 0.05^2\right)\text{rad}^2 \tag{5.29}$$

We would like to note that the off-diagonal terms were not exactly zero, but were much smaller than the diagonal terms and hence neglected.

We see that the closer the marker is with respect to the camera, the lower is the position measurement noise covariance. We also note that the position measurement performance of the camera is better perpendicular to the optical axis, than along it. This is because the horizontal position is calculated from the position of the marker in the image plane, whereas the vertical position (along the optical axis) is calculated from the size of the marker in the image plane. Similarly, the orientation measurements are more precise about the optical axis as it is directly seen as a rotation in the image plane, whereas the other two orientation measurements are calculated from the projected side lengths of the marker in the image plane. The camera measures the relative pose of the marker at approximately the frame rate, which is set to 30 Hz. The marker does go undetected in certain frames due to motion blur from vibrations and fast relative motion. However, this irregularity is not found to affect the localization and docking performance much.

Experimental Setup

The motion-capture system measures the absolute position and orientation of each of the vehicles and runs at 200 Hz. The flight controller of the active quadcopter is connected to the camera via a serial port (UART) and transmits IMU data to the camera at 500 Hz. The EKF is run on the camera's processor at 500 Hz, predicting the states forward using the IMU data, and doing the relative pose measurement updates at around 30 Hz based on the marker detection. The passive quadcopter's attitude is sent to the active quadcopter via a radio at approximately 100 Hz, which is used in the EKF. The state estimates are sent from the camera to the flight controller at 500 Hz, which are then used for closed-loop control. During closed-loop control of the active quadcopter via onboard sensing, we continue recording motion capture measurements as ground truth, to evaluate the performance of the onboard state estimator.

Results

The experiment that we conduct involves the active quadcopter flying to a particular location, using offboard sensing, and the passive quadcopter flying to about 0.6 m vertically above the active quadcopter, again using offboard sensing. Once the passive quadcopter's marker is in the FoV of the active quadcopter's camera, we close the loop and start using purely onboard sensing for flying the active quadcopter. A docking command is then issued to the active quadcopter where it starts to ascend and close the vertical gap between itself and the passive

quadcopter. Once the docking platform is within 15.0 cm vertically from the docking legs of the passive quadcopter, and their geometric centers are within 2.5 cm in the horizontal plane (based on the onboard estimate), the passive quadcopter is commanded to stop its motors and fall freely onto the docking platform. The docking platform is forgiving to small position and yaw errors and thus the passive quadcopter slides into the platform and docks with the active quadcopter. Simultaneously, the active quadcopter automatically switches back to using offboard sensing, since the marker is no longer visible at such a close distance, and updates its mass and moment of inertia.

For undocking, the passive quadcopter is simply commanded to start hovering at the previous desired position, and the active quadcopter is commanded to go vertically downwards by the original vertical separation.

The experiment was verified for repeatability by successfully performing docking using onboard sensing five times. The experimental footage can be seen in the video attachment. Figure 5.1 shows a sequence of snapshots of the docking procedure. We can see that the marker is detected even when the two quadcopters are flying very close (a green border is shown around the detected marker), but remains undetected in the docked configuration.

We show plots of estimated position and attitude from the EKF, and the motion-capture values for a sample experiment during the docking maneuver in Figure 5.4.

The estimation error (difference between onboard estimate and ground truth) in position is always within 10 cm, and reduces to less than 2 cm when the vehicles get close enough for docking. The attitude estimation error for yaw is within 5 deg which is noticeably higher than the estimation error in roll and pitch. The reason for this is that the yaw rotation (about gravity) is mostly observed purely via the marker, whereas the roll and pitch rotations are observed via both the marker and the accelerometer measurement which remains mostly nearly parallel to gravity during flight.

5.6 Conclusion

We have developed a relative state estimation algorithm based on EKF formulation to localize one "active" multirotor with respect to another "passive" multirotor, using just onboard sensors. Specifically, the active multirotor uses its accelerometer, rate gyroscope, and an onboard camera looking at a marker on the passive multirotor to determine its relative position and velocity with respect to the passive multirotor, and its absolute orientation with respect to an inertial frame. Notably, the estimator requires no knowledge of the physical parameters of the vehicles such as mass, moment of inertia, or aerodynamic properties. We also presented a control architecture that can use these relative state estimates to control the active quadcopter at a desired setpoint with respect to the passive quadcopter. The performance of estimator and control architecture was experimentally validated via repeatable midair docking experiments where we were able to successfully dock the multirotors – a task requiring position precision on the order of a centimeter.

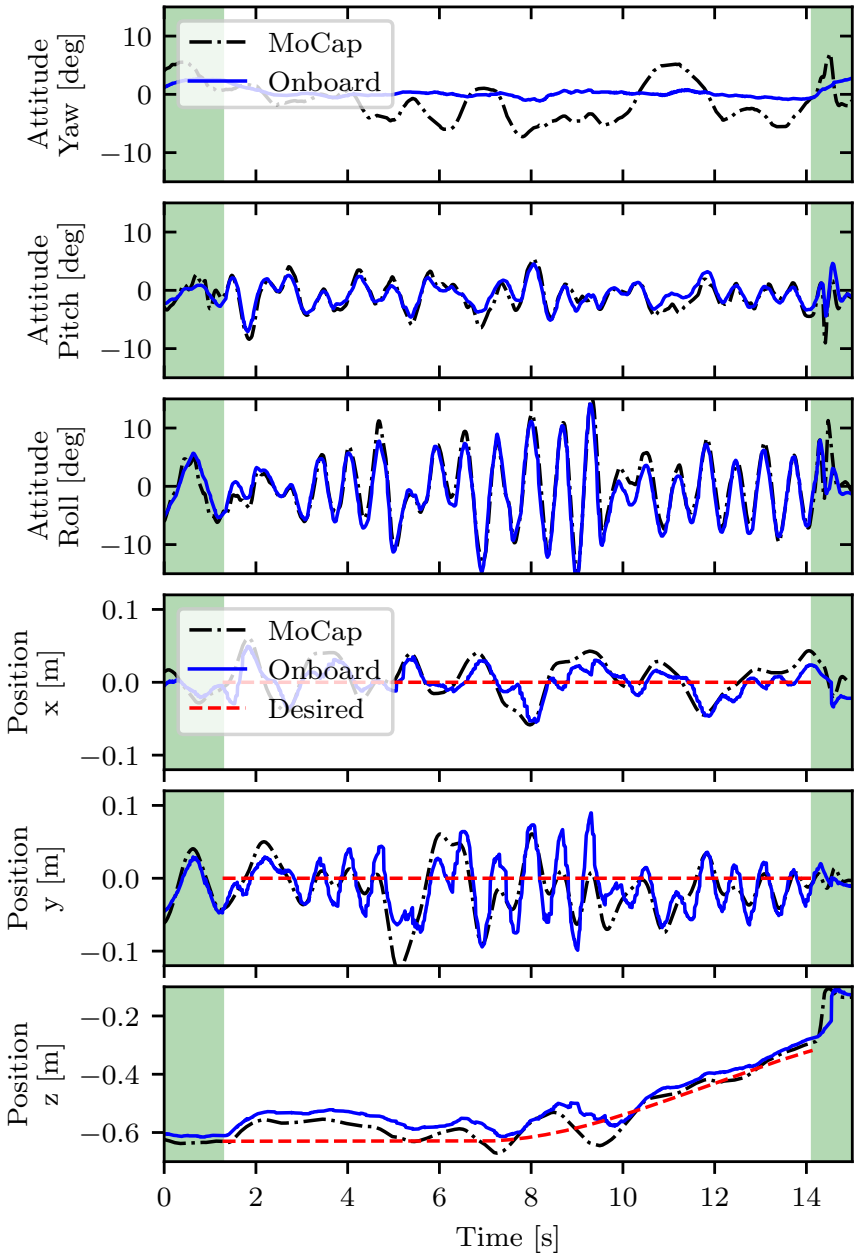

Figure 5.4: Attitude and relative position estimates from the onboard state estimator compared with the motion-capture values. We also plot desired position. Green background (at the start and end of the plot) means that the active quadcopter is controlled using offboard state estimates, while clear background means that onboard state estimates are used. The position estimation error is found to be lesser than 2 cm when the two quadcopters are in docking range. At about 14 s, the vehicles dock.

A possible extension to this work is to use onboard sensing for absolute localization of both the passive and active quadcopter, for example via GPS [75]. This will allow extension of this work's contribution to outdoor applications of modular and cooperative robots.

Chapter 6

Conclusion

This dissertation presents several approaches to extend the endurance of eVTOL aircraft, with the focus being on mitigating limitations posed by energy storage. Specifically, we propose novel designs and system architecture to solve the problem of limited endurance of eVTOLs.

In Chapter 2, we explored a simple approach tethering a series of aerial vehicles to a power supply. This eliminates the flight time limitation due to the energy source. However, this comes with the tradeoff of the limited reach of the system, which is governed by the tether length. Essentially, this concept is useful for applications where the flight time of the vehicles is the primary concern, but not the range. For example, in firefighting or long-duration surveillance, where the eVTOL vehicle needs to hold a position in a certain region. A power analysis is presented for a series of N multirotors connected to a power supply (electrically in parallel). The behavior of power consumption with respect to the thrust of each multirotor is studied, which guarantees electrical safety and helps in design optimization with respect to parameters such as the tether length, the cross-section area of the tether (which governs the resistance per unit length), and the voltage of the power supply. A boundary is observed beyond which it is impossible to produce thrusts due to fundamental electrical limitations. It is also shown that this boundary can be manipulated by changing the power supply voltage and the tether gauge (cross-section area). We then compare the power consumption for one tethered quadcopter and two tethered quadcopters and show, for a representative use case of firefighting, that a tethered system with two quadcopters consumes 26% less power than a corresponding system with one quadcopter. Finally, we present experiments demonstrating the use of a two-quadcopter tethered system as compared to a one-quadcopter tethered system in a cluttered environment, such as passing through a window and grasping an object over an obstacle.

While having unlimited flight time is great, the limited reach of a tethered system narrows the application space. Package delivery and air taxis cannot use this approach. We try to reason about fundamental causes that limit the endurance of an eVTOL and realize that the discharged portion battery is still carried as deadweight by the vehicle. So in Chapter 3, we present an approach where an aerial vehicle can eject the used portions of its energy source,

which helps reduce power consumption and increases the flight time of the vehicle. A flight time vs. energy storage mass analysis is presented to show the endurance benefit of staging to multirotors. We consider two specific problems in discrete staging – optimal order of staging given a certain number of energy sources, and optimal partitioning of a given energy storage mass budget into a given number of stages. The optimal order of staging is proven to be staging the batteries in decreasing order of their masses. We then derive results for a continuously staged case of an internal combustion engine driving propellers and show that such a multirotor has an upper limit on achievable flight time independent of the available fuel mass. Lastly, we validate the analysis with flight experiments on custom hardware and achieve a 19% increase in flight time using the battery in two stages as compared to a single stage.

Although the staging concept does not restrict the reach of the system, even continuously staging (ejecting discharged portions) an energy source is not enough to unlock arbitrarily long flight time. In addition, there are environmental concerns about discarding used batteries, limiting the application of the staging concept to controlled settings such as warehouses. We then consider the following idea – what if the ejected discharged portions of the battery are able to fly and land safely, and can be replaced with charged ones that can fly to the vehicle. In Chapter 4, we explore and demonstrate the concept of flying batteries – secondary batteries that can fly to a mission vehicle, power it and charge its onboard battery, and then fly away after discharging themselves. This procedure allows the process to be repeatable, and is, in essence, a battery-swapping system without the need for a complex swapping mechanism. The onboard (reserve) battery on the main vehicle allows for seamless switching of the power source and can continue flying the mission vehicle for some duration while waiting for a fully-charged flying battery. This also allows it to have reserves in emergency cases where a flying battery is not available. All of these steps are performed in-flight, without the mission vehicle landing during operation, which enables uninterrupted missions which can be both long duration and long range.

We develop a design tool to choose parameters for the docking mechanism and trajectory to maximize the chance of success of a mission. We perform a long-duration flight experiment where several flying batteries sequentially dock, power the mission vehicle and recharge its onboard battery, and undock. At the end of the experiment, the primary battery on the mission vehicle is shown to be nearly fully charged, which proves that the energy storage restriction on endurance and range is successfully eliminated. Importantly, the unlimited endurance does not involve a complex battery swapping mechanism and is not associated with a large increase in overall mass or size, leaving the mission vehicle in fundamentally the same safety class.

Lastly, in Chapter 5, we explore methods to port the flying battery concept with purely onboard sensing, to enable its application in the real world. Specifically, we solve the problem of precise relative localization of two eVTOL vehicles that allows them to dock reliably. We use a combination of an IMU and a camera that provides relative pose measurements with respect to a marker. The measurements from these sensors are fused via an EKF to estimate the relative pose of the mission vehicle with respect to the flying battery, and its absolute

roll and pitch. These estimates are then used to control the mission vehicle and dock it with the flying battery, which requires a centimeter-level precision. The docking using purely onboard sensing for the mission vehicle is demonstrated experimentally to be repeatable and reliable.

This dissertation has shown how the endurance and range of eVTOL aircraft can be extended arbitrarily by tackling the energy storage aspect and coming up with novel system architectures. Although the endurance could perhaps be marginally improved via design changes to increase efficiency, in this work we have unlocked arbitrarily long endurance and range for eVTOL aircraft by solving the simple but subtle task of replacing discharged portions of the energy storage with charged ones. This is achieved without complicated and heavy mechanisms, and minor but intelligent design changes which are not associated with substantial costs or weight increase. Thus, we argue that the endurance and range of eVTOL aircraft can be extended using the aforementioned ideas, with a relatively small tradeoff.

Future Work

There are several interesting avenues of research stemming from the topics covered in this dissertation.

For the series of tethered multirotors, a power analysis combining the electrical aspect with the mechanical aspect of tether forces with respect to the positions of the multirotors would be very useful for optimally placing the vehicles in the case of a surveillance scenario of a building that needs to be monitored from different locations. This would also be helpful in designing efficient trajectories for applications such as harvesting fruits in an orchard, and firefighting.

For the concept of staging energy sources, there are several environmental concerns about ejecting used batteries, which essentially limits their application to controlled spaces such as inspection in warehouses. An interesting extension would be optimally choosing the drop locations of the used stages in the warehouse, and autonomously collecting these used stages for future use. If they are to be used in an outdoor setting, another extension would be to do path planning for safe locations to eject the used stages to avoid damage to the battery and the surroundings, and automate the recovery of the ejected stages.

Finally, for the concept of flying batteries, a complete solution to get this system working outdoors still needs to be found. The use of GPS for absolute localization seems like an obvious choice, but the quality of measurements from the GPS needs to be taken into account and fused intelligently with the more precise relative localization in order to dock reliably while maintaining robustness with respect to disturbances and poor quality measurements. Optimally placing the flying battery stations for a long-range mission, and path planning for the flying battery to intercept the main vehicle path and dock with it in motion are open problems.

In summary, the problem of unlimited endurance and range still has a lot of room for exploration, with a massive design space. A neat end-to-end solution to this problem has the

potential to bring about a paradigm shift and disrupt several industries, with a few notable ones being aerial package delivery and air taxis.

Bibliography

[1] Xiao-Guang Yang et al. "Challenges and key requirements of batteries for electric vertical takeoff and landing aircraft". In: *Joule* 5.7 (2021), pp. 1644–1659.

[2] Kai Wang, Aoyong Li, and Xiaobo Qu. "Urban aerial mobility: Network structure, transportation benefits, and Sino-US comparison". In: *The Innovation* 4.2 (2023), p. 100393.

[3] Alex M Stoll et al. "Conceptual design of the Joby S2 electric VTOL PAV". In: *14th AIAA Aviation Technology, Integration, and Operations Conference*. 2014, p. 2407.

[4] Kyle A Pascioni et al. "Acoustic Flight Test of the Joby Aviation Advanced Air Mobility Prototype Vehicle". In: *28th AIAA/CEAS Aeroacoustics 2022 Conference*. 2022, p. 3036.

[5] Sean O'Neill. *Electric Air Taxis Create Megadeal Buzz*. 2022.

[6] Sajal Sharma et al. "UAV for Surveillance and Environmental Monitoring". In: *Indian Journal of Science and Technology* 9.43 (2016).

[7] Sonia Waharte and Niki Trigoni. "Supporting search and rescue operations with UAVs". In: *2010 International Conference on Emerging Security Technologies (EST)*. IEEE. 2010, pp. 142–147.

[8] Milan Erdelj et al. "Help from the sky: Leveraging UAVs for disaster management". In: *IEEE Pervasive Computing* 16.1 (2017), pp. 24–32.

[9] Jonathan Cacace et al. "A control architecture for multiple drones operated via multimodal interaction in search & rescue mission". In: *2016 IEEE International Symposium on Safety, Security, and Rescue Robotics (SSRR)*. IEEE. 2016, pp. 233–239.

[10] Cornelius A Thiels et al. "Use of unmanned aerial vehicles for medical product transport". In: *Air medical journal* 34.2 (2015), pp. 104–108.

[11] MA Boon, AP Drijfhout, and S Tesfamichael. "Comparison of a Fixed-Wing and Multi-Rotor UAV for Environmental Mapping Applications: A Case Study". In: *The International Archives of Photogrammetry, Remote Sensing and Spatial Information Sciences* 42 (2017), p. 47.

[12] Nitash P Balsara and John Newman. "Comparing the energy content of batteries, fuels, and materials". In: *Journal of chemical education* 90.4 (2013), pp. 446–452.

[13] Yaniv Maor, Elad Shifman, and ELI Moshe. *Device and method for fruit harvesting*. US Patent App. 17/200,965. 2021.

[14] Evan Ackerman and Eliza Strickland. "Medical delivery drones take flight in east africa". In: *IEEE Spectrum* 55.1 (2018), pp. 34–35.

[15] Wayne Johnson, Christopher Silva, and Eduardo Solis. "Concept vehicles for VTOL air taxi operations". In: *AHS Specialists"Conference on Aeromechanics Design for Transformative Vertical Flight*. ARC-E-DAA-TN50731. 2018.

[16] Barnes W McCormick. *Aerodynamics, Aeronautics and Flight Mechanics*. John Wiley & Sons Inc., 1995.

[17] Conrad Holda, Behnam Ghalamchi, and Mark W Mueller. "Tilting multicopter rotors for increased power efficiency and yaw authority". In: *2018 International Conference on Unmanned Aircraft Systems (ICUAS)*. IEEE. 2018, pp. 143–148.

[18] Adnan S Saeed et al. "A survey of hybrid unmanned aerial vehicles". In: *Progress in Aerospace Sciences* 98 (2018), pp. 91–105.

[19] Jerry Tang, Karan P Jain, and Mark W Mueller. "QUaRTM: A Quadcopter with Unactuated Rotor Tilting Mechanism capable of faster, more agile, and more efficient flight". In: *Frontiers in Robotics and AI* 9 (2022), p. 287.

[20] Andrea Tagliabue, Xiangyu Wu, and Mark W Mueller. "Model-free Online Motion Adaptation for Optimal Range and Endurance of Multicopters". In: *2019 International Conference on Robotics and Automation (ICRA)*. IEEE. 2019, pp. 5650–5656.

[21] Kitt C Reinhardt et al. "Solar-powered unmanned aerial vehicles". In: *IECEC 96. Proceedings of the 31st Intersociety Energy Conversion Engineering Conference*. Vol. 1. IEEE. 1996, pp. 41–46.

[22] Danny Lee, Joe Zhou, and Wong Tze Lin. "Autonomous battery swapping system for quadcopter". In: *2015 International Conference on Unmanned Aircraft Systems (ICUAS)*. IEEE. 2015, pp. 118–124.

[23] N Kemal Ure et al. "An automated battery management system to enable persistent missions with multiple aerial vehicles". In: *IEEE/ASME transactions on mechatronics* 20.1 (2014), pp. 275–286.

[24] Eamon Barrett et al. "Autonomous Battery Exchange of UAVs with a Mobile Ground Base". In: *2018 IEEE International Conference on Robotics and Automation (ICRA)*. IEEE. 2018, pp. 699–705.

[25] Seiga Kiribayashi, Jun Ashizawa, and Keiji Nagatani. "Modeling and design of tether powered multicopter". In: *2015 IEEE International Symposium on Safety, Security, and Rescue Robotics (SSRR)*. IEEE. 2015, pp. 1–7.

[26] Ryoma Moro et al. "28 GHz microwave power beaming to a free-flight drone". In: *2021 IEEE Wireless Power Transfer Conference (WPTC)*. IEEE. 2021, pp. 1–4.

[27] Michael C Achtelik et al. "Design of a flexible high performance quadcopter platform breaking the MAV endurance record with laser power beaming". In: *2011 IEEE/RSJ International Conference on Intelligent Robots and Systems*. IEEE. 2011, pp. 5166–5172.

[28] Daniel A Rico, Francisco Muñoz-Arriola, and Carrick Detweiler. "Trajectory Selection for Power-over-Tether Atmospheric Sensing UAS". In: *2021 IEEE/RSJ International Conference on Intelligent Robots and Systems (IROS)*. IEEE. 2021, pp. 2321–2328.

[29] Keigo Watanabe et al. "Development of a camera-mounted tethered Quadrotor for inspecting infrastructures". In: *IECON 2016-42nd Annual Conference of the IEEE Industrial Electronics Society*. IEEE. 2016, pp. 6128–6133.

[30] Andrew J Torgesen, Jonathan P How, and Benjamin Cameron. "Airborne Sensing for Ship Air Wake Surveys with a Tethered Autonomous UAV". In: *AIAA Scitech 2021 Forum*. 2021, p. 0381.

[31] Thomas J Nugent Jr and Jordin T Kare. "Laser power beaming for defense and security applications". In: *Unmanned systems technology XIII* 8045 (2011), pp. 384–391.

[32] Ke Jin and Weiyang Zhou. "Wireless laser power transmission: A review of recent progress". In: *IEEE Transactions on Power Electronics* 34.4 (2018), pp. 3842–3859.

[33] Jørgen Apeland, Dimitrios Pavlou, and Tor Hemmingsen. "Suitability analysis of implementing a fuel cell on a multirotor drone". In: *Journal of Aerospace Technology and Management* 12 (2020).

[34] XIE Ye et al. "Review of hybrid electric powered aircraft, its conceptual design and energy management methodologies". In: *Chinese Journal of Aeronautics* 34.4 (2021), pp. 432–450.

[35] Karan P Jain et al. "Staging energy sources to extend flight time of a multirotor UAV". In: *2020 IEEE/RSJ International Conference on Intelligent Robots and Systems (IROS)*. IEEE. 2020, pp. 1132–1139.

[36] Karan P Jain et al. "Tethered Power Supply for Quadcopters: Architecture, Analysis and Experiments". In: *arXiv preprint arXiv:2203.08180* (2022).

[37] Karan P Jain and Mark W Mueller. "Flying batteries: In-flight battery switching to increase multirotor flight time". In: *2020 IEEE International Conference on Robotics and Automation (ICRA)*. IEEE. 2020, pp. 3510–3516.

[38] Karan P Jain et al. "Modeling of aerodynamic disturbances for proximity flight of multirotors". In: *2019 International Conference on Unmanned Aircraft Systems (ICUAS)*. IEEE. 2019, pp. 1261–1269.

[39] Karan P Jain, Minos Park, and Mark W Mueller. "Docking two multirotors in midair using relative vision measurements". In: *arXiv preprint arXiv:2011.05565* (2020).

[40] Håvard F Grip et al. "Flight control system for NASA's Mars helicopter". In: *AIAA Scitech 2019 Forum*. 2019, p. 1289.

[41] Ralph D Lorenz et al. "Dragonfly: A rotorcraft lander concept for scientific exploration at Titan". In: *Johns Hopkins APL Technical Digest* 34.3 (2018), p. 14.

[42] Aldo Jaimes, Srinath Kota, and Jose Gomez. "An approach to surveillance an area using swarm of fixed wing and quad-rotor unmanned aerial vehicles UAV(s)". In: *2008 IEEE International Conference on System of Systems Engineering*. IEEE. 2008, pp. 1–6.

[43] Eric Cheng. *Aerial photography and videography using drones*. Peachpit Press, 2015.

[44] Joshua Fishman et al. "Dynamic Grasping with a" Soft" Drone: From Theory to Practice". In: *2021 IEEE/RSJ International Conference on Intelligent Robots and Systems (IROS)*. IEEE. 2021, pp. 4214–4221.

[45] Frederico Augugliaro et al. "The flight assembled architecture installation: Cooperative construction with flying machines". In: *IEEE Control Systems Magazine* 34.4 (2014), pp. 46–64.

[46] Prasanth Kotaru, Guofan Wu, and Koushil Sreenath. "Differential-Flatness and Control of Multiple Quadrotors with a Payload Suspended through Flexible Cables". In: *IEEE Indian Control Conference (ICC)*. Kanpur, India, 2018, pp. 352–357.

[47] Benyamin Kosarnovsky and S Arogeti. "A string of tethered drones-system dynamics and control". In: *2019 European Conference on Mobile Robots (ECMR)*. IEEE. 2019, pp. 1–6.

[48] Michele Bolognini and Lorenzo Fagiano. "Lidar-based navigation of tethered drone formations in an unknown environment". In: *IFAC-PapersOnLine* 53.2 (2020), pp. 9426–9431.

[49] Wojciech Walendziuk, Daniel Oldziej, and Maciej Slowik. "Power Supply System Analysis for Tethered Drones Application". In: *2020 International Conference Mechatronic Systems and Materials (MSM)*. IEEE. 2020, pp. 1–6.

[50] Lida Zikou, Christos Papachristos, and Anthony Tzes. "The power-over-tether system for powering small UAVs: Tethering-line tension control synthesis". In: *2015 23rd Mediterranean Conference on Control and Automation (MED)*. IEEE. 2015, pp. 681–687.

[51] Marco Tognon, Sanket S Dash, and Antonio Franchi. "Observer-based control of position and tension for an aerial robot tethered to a moving platform". In: *IEEE Robotics and Automation Letters* 1.2 (2016), pp. 732–737.

[52] Marco Tognon and Antonio Franchi. *Theory and Applications for Control of Aerial Robots in Physical Interaction Through Tethers*. Vol. 140. Springer Nature, 2020.

[53] Marco M Nicotra, Roberto Naldi, and Emanuele Garone. "Taut cable control of a tethered UAV". In: *IFAC Proceedings Volumes* 47.3 (2014), pp. 3190–3195.

[54] Taeyoung Lee. "Geometric controls for a tethered quadrotor UAV". In: *2015 54th IEEE conference on decision and control (CDC)*. IEEE. 2015, pp. 2749–2754.

[55] Prasanth Kotaru, Guofan Wu, and Koushil Sreenath. "Differential-flatness and control of quadrotor (s) with a payload suspended through flexible cable (s)". In: *2018 Indian Control Conference (ICC)*. IEEE. 2018, pp. 352–357.

[56] Diego S D'antonio, Gustavo A Cardona, and David Saldaña. "The catenary robot: Design and control of a cable propelled by two quadrotors". In: *IEEE Robotics and Automation Letters* 6.2 (2021), pp. 3857–3863.

[57] Vishal Abhishek, Vaibhav Srivastava, and Ranjan Mukherjee. "Towards a heterogeneous cable-connected team of UAVs for aerial manipulation". In: *2021 American Control Conference (ACC)*. IEEE. 2021, pp. 54–59.

[58] Prasanth Kotaru and Koushil Sreenath. "Multiple quadrotors carrying a flexible hose: dynamics, differential flatness and control". In: *IFAC-PapersOnLine* 53.2 (2020), pp. 8832–8839.

[59] ChangHyeon Lee et al. "Energy Consumption Analysis of Downward-Tethered Quadcopter". In: *2021 21st International Conference on Control, Automation and Systems (ICCAS)*. IEEE. 2021, pp. 1212–1215.

[60] Edward Harrington Lockwood. *A book of curves*. Cambridge University Press, 1967.

[61] Sebastian Siebert and Jochen Teizer. "Mobile 3D mapping for surveying earthwork projects using an Unmanned Aerial Vehicle (UAV) system". In: *Automation in construction* 41 (2014), pp. 1–14.

[62] Håvard F Grip et al. "Guidance and control for a Mars helicopter". In: *2018 AIAA Guidance, Navigation, and Control Conference*. 2018, p. 1849.

[63] Andreas Johanning, Markus Pagitz, and Josep M. Mirats-Tur. "Celldrone - a Modular Multi-rotor Aircraft". In: *Deutscher Luft-und Raumfahrtkongress*. 2011.

[64] HH Hall and ED Zambelli. "On the optimization of multistage rockets". In: *Journal of Jet Propulsion* 28.7 (1958), pp. 463–465.

[65] Richard D Geckler. "Ideal performance of multistage rockets". In: *ARS Journal* 30.6 (1960), pp. 531–536.

[66] JS Gray and RV Alexander. "Cost and weight optimization for multistage rockets". In: *Journal of Spacecraft and Rockets* 2.1 (1965), pp. 80–86.

[67] Analiza Abdilla, Arthur Richards, and Stephen Burrow. "Power and endurance modelling of battery-powered rotorcraft". In: *2015 IEEE/RSJ International Conference on Intelligent Robots and Systems (IROS)*. IEEE. 2015, pp. 675–680.

[68] Stephen Boyd and Lieven Vandenberghe. *Convex optimization*. Cambridge university press, 2004.

[69] Nimal Navarathinam, Regina Lee, and Hugh Chesser. "Characterization of Lithium-Polymer batteries for CubeSat applications". In: *Acta Astronautica* 68.11-12 (2011), pp. 1752–1760.

[70] Xue Wang et al. "Economic and environmental characterization of an evolving Li-ion battery waste stream". In: *Journal of environmental management* 135 (2014), pp. 126–134.

[71] Ryo Miyazaki et al. "Airborne docking for multi-rotor aerial manipulations". In: *2018 IEEE/RSJ International Conference on Intelligent Robots and Systems (IROS)*. IEEE. 2018, pp. 4708–4714.

[72] David Saldana et al. "Modquad: The flying modular structure that self-assembles in midair". In: *2018 IEEE International Conference on Robotics and Automation (ICRA)*. IEEE. 2018, pp. 691–698.

[73] Taeyoung Lee, Melvin Leok, and N Harris McClamroch. "Geometric tracking control of a quadrotor UAV on SE (3)". In: *49th IEEE conference on decision and control (CDC)*. IEEE. 2010, pp. 5420–5425.

[74] Dimitri Bertsekas. *Dynamic programming and optimal control: Volume I*. Vol. 1. Athena scientific, 2012.

[75] Abdelkrim Nemra and Nabil Aouf. "Robust INS/GPS sensor fusion for UAV localization using SDRE nonlinear filtering". In: *IEEE Sensors Journal* 10.4 (2010), pp. 789–798.

[76] Mohammad Fattahi Sani and Ghader Karimian. "Automatic navigation and landing of an indoor AR. drone quadrotor using ArUco marker and inertial sensors". In: *2017 International Conference on Computer and Drone Applications (IConDA)*. IEEE. 2017, pp. 102–107.

[77] Jan Bacik et al. "Autonomous flying with quadrocopter using fuzzy control and ArUco markers". In: *Intelligent Service Robotics* 10.3 (2017), pp. 185–194.

[78] Michael J Duffy and Anthony Samaritano. "The LIFT! project-modular, electric vertical lift system with ground power tether". In: *33rd AIAA Applied Aerodynamics Conference*. 2015, p. 3013.

[79] Bruno Gabrich et al. "A flying gripper based on cuboid modular robots". In: *2018 IEEE International Conference on Robotics and Automation (ICRA)*. IEEE. 2018, pp. 7024–7030.

[80] Moju Zhao et al. "Design, modeling, and control of an aerial robot dragon: A dual-rotor-embedded multilink robot with the ability of multi-degree-of-freedom aerial transformation". In: *IEEE Robotics and Automation Letters* 3.2 (2018), pp. 1176–1183.

[81] Guanrui Li et al. "ModQuad-Vi: A vision-based self-assembling modular quadrotor". In: *2019 International Conference on Robotics and Automation (ICRA)*. IEEE. 2019, pp. 346–352.

[82] Ryan Rocha and Stephen K Robinson. "Toward Autonomous In-flight Docking of Unmanned Multi-rotor Aerial Vehicles". In: *AIAA Scitech 2020 Forum*. 2020, p. 1486.

[83] Eric N Johnson et al. "Real-time vision-based relative aircraft navigation". In: *Journal of Aerospace Computing, Information, and Communication* 4.4 (2007), pp. 707–738.

[84] Daniel Briggs Wilson, Ali Göktogan, and Salah Sukkarieh. "Guidance and Navigation for UAV Airborne Docking." In: *Robotics: Science and Systems*. Vol. 3. 3. 2015.

[85] Andreas Huster and Stephen M Rock. "Relative position sensing by fusing monocular vision and inertial rate sensors". PhD thesis. Citeseer, 2003.

[86] Jed M Kelsey et al. "Vision-based relative pose estimation for autonomous rendezvous and docking". In: *2006 IEEE aerospace conference*. IEEE. 2006, 20–pp.

[87] L Regoli et al. "On-line robust pose estimation for rendezvous and docking in space using photonic mixer devices". In: *Acta Astronautica* 96 (2014), pp. 159–165.

[88] Mark W Mueller. "A Dynamics-Agnostic State Estimator for Unmanned Aerial Vehicles Using Ultra-Wideband Radios". In: *Dynamic Systems and Control Conference*. Vol. 51913. American Society of Mechanical Engineers. 2018, V003T36A002.

[89] Mark E Pittelkau. "Rotation vector in attitude estimation". In: *Journal of Guidance, Control, and Dynamics* 26.6 (2003), pp. 855–860.

[90] Mark W Mueller, Markus Hehn, and Raffaello D'Andrea. "Covariance correction step for kalman filtering with an attitude". In: *Journal of Guidance, Control, and Dynamics* 40.9 (2017), pp. 2301–2306.

[91] Dan Simon. *Optimal state estimation: Kalman, H infinity, and nonlinear approaches*. John Wiley & Sons, 2006.

[92] Wojciech Giernacki et al. "Crazyflie 2.0 quadrotor as a platform for research and education in robotics and control engineering". In: *2017 22nd International Conference on Methods and Models in Automation and Robotics (MMAR)*. IEEE. 2017, pp. 37–42.

[93] Sergio Garrido-Jurado et al. "Generation of fiducial marker dictionaries using mixed integer linear programming". In: *Pattern Recognition* 51 (2016), pp. 481–491.

[94] Francisco J Romero-Ramirez, Rafael Muñoz-Salinas, and Rafael Medina-Carnicer. "Speeded up detection of squared fiducial markers". In: *Image and vision Computing* 76 (2018), pp. 38–47.

[95] G. Bradski. "The OpenCV Library". In: *Dr. Dobb's Journal of Software Tools* (2000).

[96] Deebul Nair, Amirhossein Pakdaman, and Paul G Plöger. "Performance Evaluation of Low-Cost Machine Vision Cameras for Image-Based Grasp Verification". In: *arXiv preprint arXiv:2003.10167* (2020).

[97] Derrick Yeo et al. "An Empirical Model of Rotorcraft UAV Downwash for Disturbance Localization and Avoidance". In: *AIAA Atmospheric Flight Mechanics Conference*. 2015, p. 1685.

[98] Steven Yoon, Henry C Lee, and Thomas H Pulliam. "Computational analysis of multi-rotor flows". In: *54th AIAA Aerospace Sciences Meeting*. 2016, p. 0812.

[99] Waqas Khan, Meyer Nahon, and Ryan Caverly. "Propeller slipstream model for small unmanned aerial vehicles". In: *AIAA modeling and simulation technologies (MST) conference*. 2013, p. 4907.

[100] Eric Hirst. *ANALYSIS OF BUOYANT JETS WITHIN THE ZONE OF FLOW ESTABLISHMENT.* Tech. rep. Oak Ridge National Lab., Tenn., 1971.

[101] Stephen B Pope and Stephen B Pope. *Turbulent flows*. Cambridge university press, 2000.

[102] H Fellouah, CG Ball, and A Pollard. "Reynolds number effects within the development region of a turbulent round free jet". In: *International Journal of Heat and Mass Transfer* 52.17-18 (2009), pp. 3943–3954.

[103] Peter Davidson. *Turbulence: an introduction for scientists and engineers*. Oxford University Press, 2015.

[104] Gabriel Hoffmann et al. "Quadrotor helicopter flight dynamics and control: Theory and experiment". In: *AIAA guidance, navigation and control conference and exhibit*. 2007, p. 6461.

[105] Moses Bangura and Robert Mahony. "Thrust control for multirotor aerial vehicles". In: *IEEE Transactions on Robotics* 33.2 (2017), pp. 390–405.

Appendix A

Agile maneuvers in docked configuration

The increased mass and moment of inertia of the main vehicle in the docked configuration reduces its agility. However, it can still perform moderately agile motion while maintaining electrical contact, even without an active fixing mechanism. This can be analyzed by computing the required friction for zero relative acceleration between the two vehicles when docked. We assume, for simplicity, that the only forces acting on the main vehicle are its weight, total thrust from the propellers $\boldsymbol{f}_T$, and the normal $\boldsymbol{f}_N$ and friction $\boldsymbol{f}_f$ force at the docking mechanism, as is shown in Figure A.1. The flying battery is acted upon by its weight, and the normal and friction forces from the docking mechanism (equal and opposite to those acting on the main vehicle). The vector of gravity is $\boldsymbol{g}$. Letting m_{mv} and m_{fb} respectively be the mass of the main vehicle and the flying battery, we can compute the requirement for zero relative acceleration by applying Newton's law, where $\boldsymbol{a}_{\text{mq}}$ and $\boldsymbol{a}_{\text{fb}}$ are the acceleration of the main vehicle and flying battery, respectively:

$$\mathbf{0} = \boldsymbol{a}_{\text{mq}} - \boldsymbol{a}_{\text{fb}} \tag{A.1}$$

$$= \frac{m_{\text{mv}}\boldsymbol{g} + \boldsymbol{f}_T + \boldsymbol{f}_N + \boldsymbol{f}_f}{m_{\text{mv}}} - \frac{m_{\text{fb}}\boldsymbol{g} - \boldsymbol{f}_N - \boldsymbol{f}_f}{m_{\text{fb}}} \tag{A.2}$$

$$= \frac{\boldsymbol{f}_T}{m_{\text{mv}}} + \boldsymbol{f}_N \frac{m_{\text{mv}} + m_{\text{fb}}}{m_{\text{mv}} m_{\text{fb}}} + \boldsymbol{f}_f \frac{m_{\text{mv}} + m_{\text{fb}}}{m_{\text{mv}} m_{\text{fb}}} \tag{A.3}$$

Because the body-fixed thrust direction is normal to the docking platform, the forces $\boldsymbol{f}_T$ and $\boldsymbol{f}_N$ are parallel, and perpendicular to $\boldsymbol{f}_f$. As long as the thrust produced by the main vehicle is positive (as would be true under almost all flight conditions), the normal force at the platform will act into the platform (ensuring electrical contact), and no friction force is required for the vehicles to remain docked. In reality, there will be additional forces acting on the system, such as aerodynamic drag during translation. In such cases, the required friction force is non-zero. Large angular velocities or angular accelerations may lead to loss of normal force. However, placing the docking platform close to the main vehicle's center of mass makes this unlikely to occur.

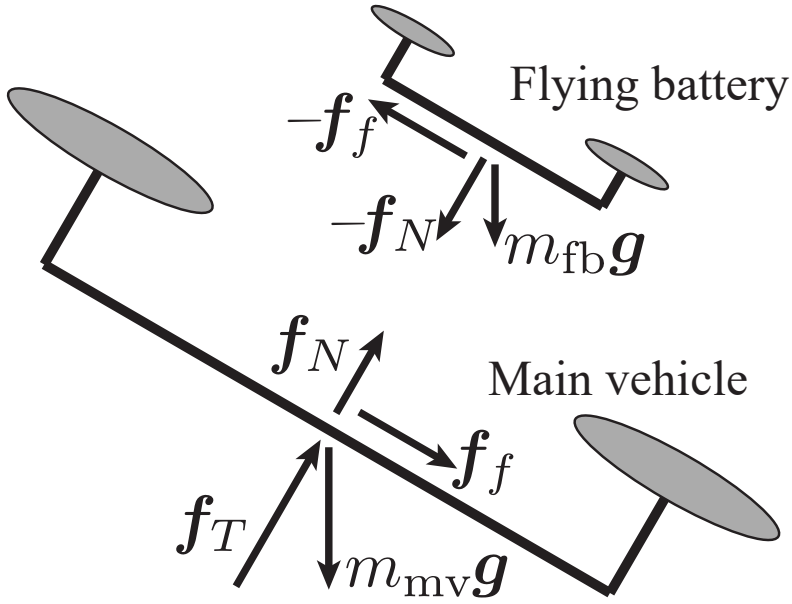

Figure A.1: Free body diagram of the two vehicles in the docked configuration. The vehicles are shown spaced apart for ease of visualization.

Appendix B

Modeling aerodynamic disturbances

The material in this chapter is based on the following previously published work.

- Karan P Jain et al. "Modeling of aerodynamic disturbances for proximity flight of multirotors". In: *2019 International Conference on Unmanned Aircraft Systems (ICUAS)*. IEEE. 2019, pp. 1261–1269

A critical consideration for docking two quadcopters mid-air is the mutual aerodynamic interference caused by the airflow of the two vehicles. This chapter explores the modeling of aerodynamic forces and torques on the one multirotor flying in the downwash of another multirotor which is especially important during vertical docking. An analysis of rotorcraft downwash is presented in [97] and [98]. Figure B.1 shows a schematic picture of two quadcopters flying in proximity.

We assume that the aerodynamic disturbances experienced by a multirotor flown in the downwash of another multirotor are primarily the result of two mechanisms:

1. Drag from oncoming flow on the frame of the vehicle
2. Change in propeller thrust due to oncoming flow

The oncoming flow is due to the downwash of a multirotor. Hence, both mechanisms require a knowledge of the velocity field produced below a multirotor. Section B.1 explains the velocity field model that we employ. The mechanisms and estimation of the aerodynamic disturbances (force and torque) on another multirotor flying in this downwash are elaborated upon in Sections B.2 and B.3.

B.1 Velocity field model

We apply the following assumption on multirotor downwash flow field based on [97]: cross-stream flow is negligible. Axial velocity, which is along $\boldsymbol{z}_B$ (the unit vector along z-axis of

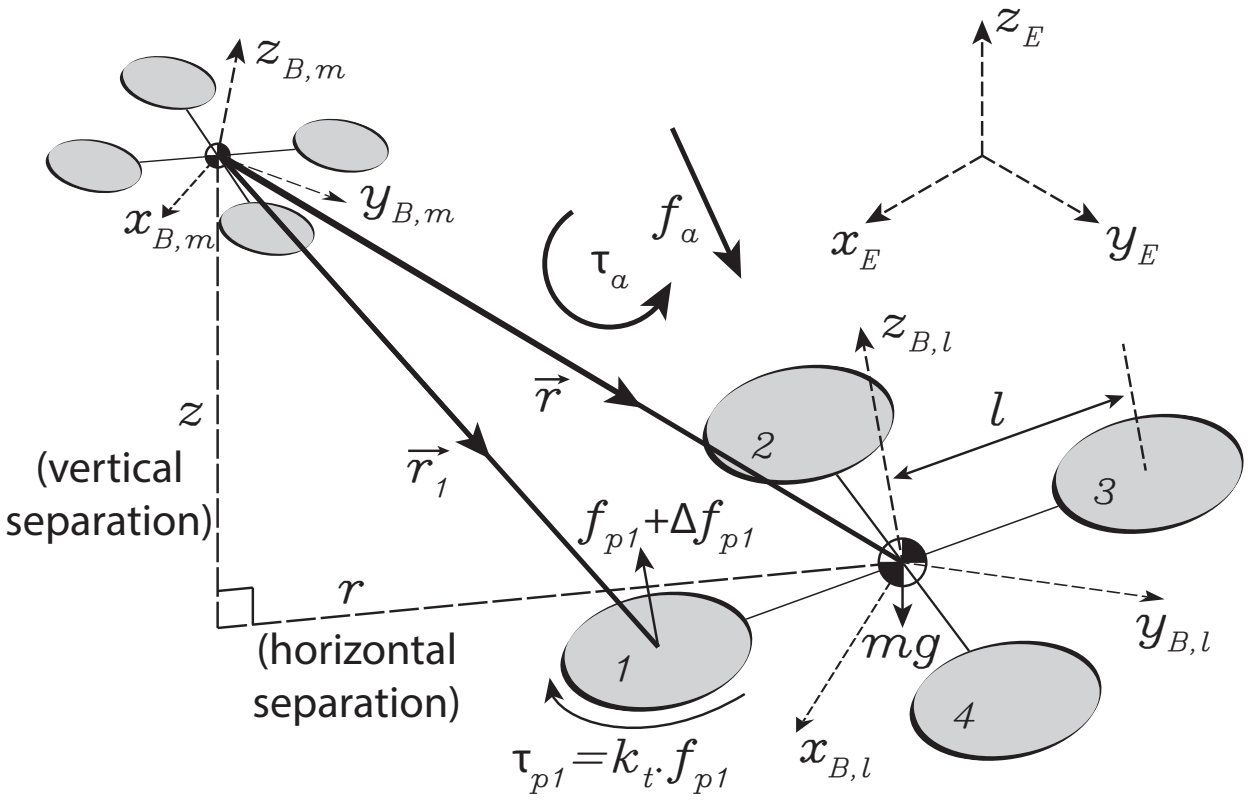

Figure B.1: Two quadcopters in proximity flight; body and inertial coordinate frames; forces and torques on large quadcopter

the concerned body), is the major component of the velocity field, and the only component we deal with.

The propeller slipstream model [99] provides an expression for the velocity field below a single propeller. It assumes that the flow is established three propeller diameters down the flow.

We model the flow field in the zone of established flow (ZEF) as axisymmetric. The velocity is now a function of vertical (axial) and horizontal (radial) separation, z and r respectively. Note that for a propeller's ZEF, low velocity induced at the center of a propeller disappears, which enables us to apply the Gaussian profile approximation with respect to radial separation [100]. Based on this information, we assume that for a multirotor's ZEF ($z > 3L$), the flows from all propellers have mixed and we can use a Gaussian profile. Here L is the vehicle size, which is twice the arm length. We shall only deal with ZEF.

Based on experimental data, we choose an inverse decay model for the centerline velocity

[101], [102].

$$\mathrm{V}_{\max}(z) = \sqrt{\frac{T}{2\rho A_p}} \frac{\mathrm{c}_{\mathrm{ax}} L}{(z - z_0)} \tag{B.1}$$

where $\sqrt{\frac{T}{2\rho A_p}}$ represents the induced velocity ($\mathrm{V_i}$) in the propeller plane given by momentum theory [16], T is the thrust produced by the propeller, ρ is the density of air, A_p is the propeller disk area, and z_0 is the virtual origin.

We normalize z with L for better intuition of velocity decay in terms of the vehicle size. The axial constant, $\mathrm{c_{ax}}$ is dimensionless and derived through experiments. Note that $\mathrm{c_{ax}}$ and z_0 depend on vehicle size and geometry according to our experimental data.

At any particular axial separation in ZEF, the velocity field follows a Gaussian profile with respect to radial separation [97, 99] given by,

$$V(z, r) = \mathrm{V}_{\max}(z) \exp\left(-\mathrm{c}_{\mathrm{rad}} \left(\frac{r}{z - z_0}\right)^2\right) \tag{B.2}$$

where $\mathrm{c_{rad}}$ is the radial decay rate and is dimensionless. It is derived using experimental data.

Since multirotor downwash is a free shear flow, the spread of the flow is assumed to grow linearly with axial separation [101], [103]. This explains the $(z - z_0)^2$ term in equation (B.2).

B.2 Drag

The force and torque due to drag is calculated using the velocity field from equation (B.2). We make the following assumptions about a multirotor frame:

1. It is a bluff body with a projected area onto a plane normal to the oncoming flow. This projected area is given by its CAD model
2. It has aerodynamic properties equivalent to a flat plate, with $C_D = 1.18$ [16].

We can predict drag force on one multirotor (large quadcopter) which is at a vertical separation of z below the other multirotor (small quadcopter) and horizontal separation of r. We assume that both the vehicles are hovering with zero roll and pitch angles. This gives us the drag force,

$$\boldsymbol{F}_D(z, r) = \int_{A_q} (-\boldsymbol{z}_{B,m}) \frac{1}{2} C_D \rho V^2(z', r') dA \tag{B.3}$$

where z' and r' are coordinates of points on the multirotor frame's surface, and A_q is the area of the multirotor frame.

The drag force integral can be calculated by dividing the multirotor frame's area into small elements and summing the forces on all these elements.

In a similar manner, we can predict torques using the velocity field as follows,

$$\boldsymbol{T}_D(z,r) = \int_{A_q} (\mathbf{r}' - \mathbf{r}) \times (-\boldsymbol{z}_{B,m}) \frac{1}{2} C_D \rho V^2(z',r') dA \tag{B.4}$$

where $\mathbf{r}$ is the position vector of the center of mass of the multirotor, and $\mathbf{r}'$ is the position vector of some point on the multirotor's frame's surface.

We define the roll, pitch, and yaw torques as the torque about $\boldsymbol{x}_B$, $\boldsymbol{y}_B$, and $\boldsymbol{z}_B$ respectively. If both vehicles are hovering then their $\boldsymbol{z}_B$'s are aligned with $\boldsymbol{z}_E$ which leads to $(\mathbf{r}' - \mathbf{r})$ being in the x-y plane. This results in the torque due to drag also being in the x-y plane, which implies that the yaw torque would be zero.

B.3 Change in Propeller Thrusts

Momentum theory [16] indicates that thrust produced by a propeller decreases as oncoming flow incident on the plane of the propeller increases in velocity, subject to constant power consumption. This effect has been addressed in [104] which compares hover thrusts with and without oncoming flows and approximates the effect as a fourth order polynomial in oncoming flow velocity, and in [105] which uses blade element momentum theory.

The degree to which the thrust of the propeller changes as a function of oncoming flow velocity is difficult to model using computational methods because the effect is heavily propeller specific and involves unsteady, turbulent flow.

For our analysis, we make the following assumptions: all oncoming flows are normal to the plane of the propeller, and Δf_p is a function of propeller speed (ω_p) and oncoming flow velocity ($\mathrm{v_{on}}$). We know that the thrust is proportional to the square of propeller speed [16]. We denote the original propeller force as $f_{p,old} = \mathrm{k_1}\omega_p^2$, and the propeller force with oncoming flow as $f_{p,new} = \mathrm{k_2(v_{on})}\omega_p^2$.

Clearly, $\mathrm{k_2}(0) = \mathrm{k_1}$. We make a first order approximation for $\mathrm{k_2(v_{on})}$ given by,

$$\mathrm{k_2(v_{on})} = \mathrm{k_1} - \mathrm{b_v v_{on}} \tag{B.5}$$

where $\mathrm{b_v}$ is the thrust decay coefficient, which is obtained experimentally.

Using equation (B.5), and $\Delta f_{pi} = f_{p,new} - f_{p,old}$, the change in propeller thrust is given by,

$$\Delta f_{pi}\,(\omega_{pi}, \mathrm{v_{on}}) = -\mathrm{b_v v_{on}}\omega_{pi}^2 \tag{B.6}$$

In the case of one vehicle flying below another, the oncoming flow velocity experienced by the bottom vehicle is a function of its relative separation from the top vehicle. In general, each propeller of the bottom vehicle will experience a different oncoming flow velocity. Let the propellers, numbered $i = 1$ through n, be at position (z_i, r_i).

The total disturbance force that the multirotor experiences due to change in propeller thrusts is the sum of Δf_{pi} of each propeller, which are assumed to be parallel to the vehicle's z-axis, $\boldsymbol{z}_B$. The disturbance force due to change in propeller forces is then given by,

$$\boldsymbol{F}_P = \sum_{i=1}^{n} \boldsymbol{z}_B \Delta f_{pi} \left(\omega_{pi}, \mathrm{v_{on}}(z_i, r_i)\right) \tag{B.7}$$

The Δf_{pi} for each propeller may be different, which produces a net torque on the vehicle. If the position vector of a propeller is $\mathbf{r}_i$, then torque due to Δf_p is given by,

$$\boldsymbol{T}_P = \sum_{i=1}^{n} (\mathbf{r}_i - \mathbf{r}) \times (\boldsymbol{z}_B) \Delta f_{pi} \tag{B.8}$$

Combining the effects of drag and change in propeller thrust, we can predict the aerodynamic force and torque at any relative separation. This completes the model for estimating aerodynamic disturbances.

B.4 Determination of model parameters

We determine the fit parameters $(\mathrm{c_{ax}}, z_0, \mathrm{c_{rad}})$ by measuring velocities at various separations in the downwash of the quadcopters. It is ensured that the quadcopter mount and all our measurements points are far away ($> 1.0\,\mathrm{m}$) from walls so that the flow field is unaffected by those. Velocity is measured using a constant temperature anemometer (TSI Inc. model 1212-60). A least-squares fit is used over the measured data, and we get $\mathrm{c_{ax}} = 4.672$, $z_0 = 0.033\,\mathrm{m}$, and $\mathrm{c_{rad}} = 60.808$.

We experimentally characterize the propeller thrust changes as a function of ω_p and $\mathrm{v_{on}}$. We use a nozzle with a fan attached to its inlet, and a honeycomb mesh in front of the fan to produce a uniform flow at the exit of the nozzle. We measure the thrust produced by the propeller for various propeller speeds and oncoming flow velocities using a thrust stand. The thrust decay coefficient is calculated via a least-squares fit, and we obtain a value of $\mathrm{b_v} = 3.710 \times 10^{-7}\,\mathrm{Nm^{-1}rad^{-2}s^3}$.

B.5 Model predictions

We perform constant velocity sweep experiments to characterize aerodynamic disturbances. In these experiments, one of the vehicles is commanded to maintain a position setpoint, and the other vehicle moves from one position setpoint to another at a constant velocity. The velocity is kept low enough so that the motion of the vehicle does not affect our characterization.

The predictions that we present are for horizontal sweep experiments where the small quadcopter maintains a fixed setpoint $(0, 0, z)$ and the large quadcopter is flown below the small quadcopter from $(0, -1, 0)$ to $(0, 1, 0)$, shown in Figure B.3. We show the predictions for $z \in \{0.5, 1.0, 1.5, 2.0, 2.5\}$ m.

Figure B.4 presents the plots for aerodynamic disturbance force in z-direction (left) and roll torque (right) on the large quadcopter versus the Y-coordinate of the large quadcopter

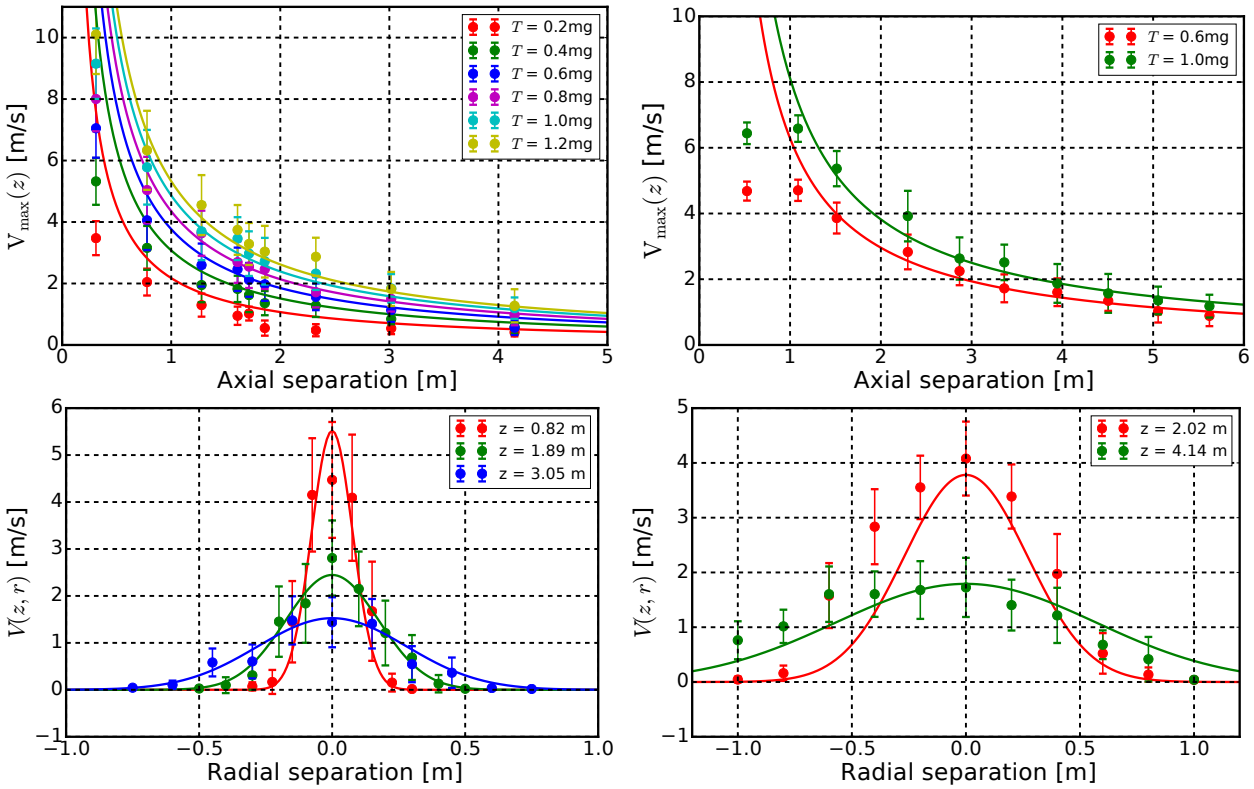

Figure B.2: Centerline flow velocity vs. axial separation for various thrusts (top), and axial flow velocity vs. radial separation for various axial separations (bottom). Presented data for small quadcopter (left) and large quadcopter (right). Error bars represent standard deviation of time-series data.

due to downwash of the small quadcopter. Top plots show the effect due to aerodynamic drag and bottom plots due to change in propeller thrusts. Forces on the large quadcopter are symmetrically distributed about $\boldsymbol{y}_B$ which results in zero pitch torque.

Experimental data for the aerodynamic disturbance force and torque gathered from proximity flight experiments of the two quadcopters is presented in Appendix B.6. Predicted values are plotted along with the experimental data to validate the model.

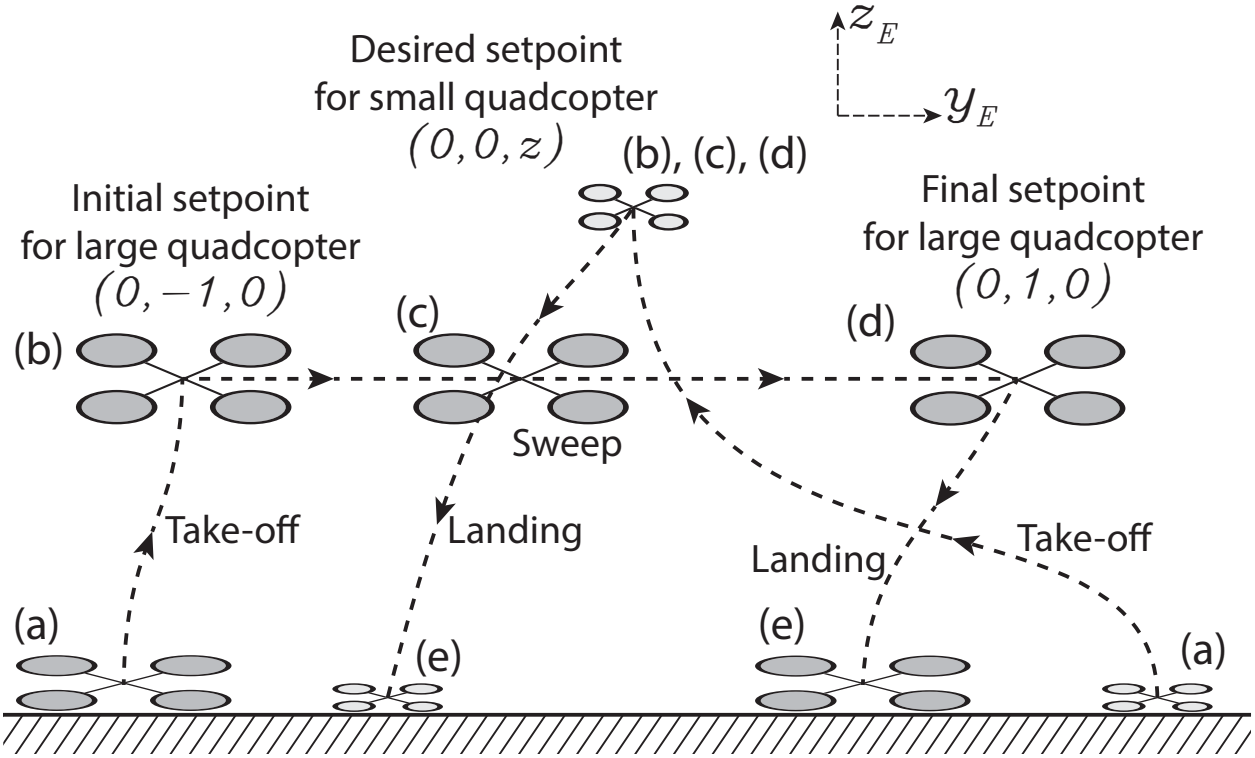

Figure B.3: Illustration of a horizontal sweep experiment: (a) Quadcopters take-off, (b) small quadcopter reaches its desired setpoint, large quadcopter reaches the initial setpoint, (c) large quadcopter begins the constant velocity sweep in +y-direction, (d) large quadcopter reaches the final setpoint, (e) Quadcopters land

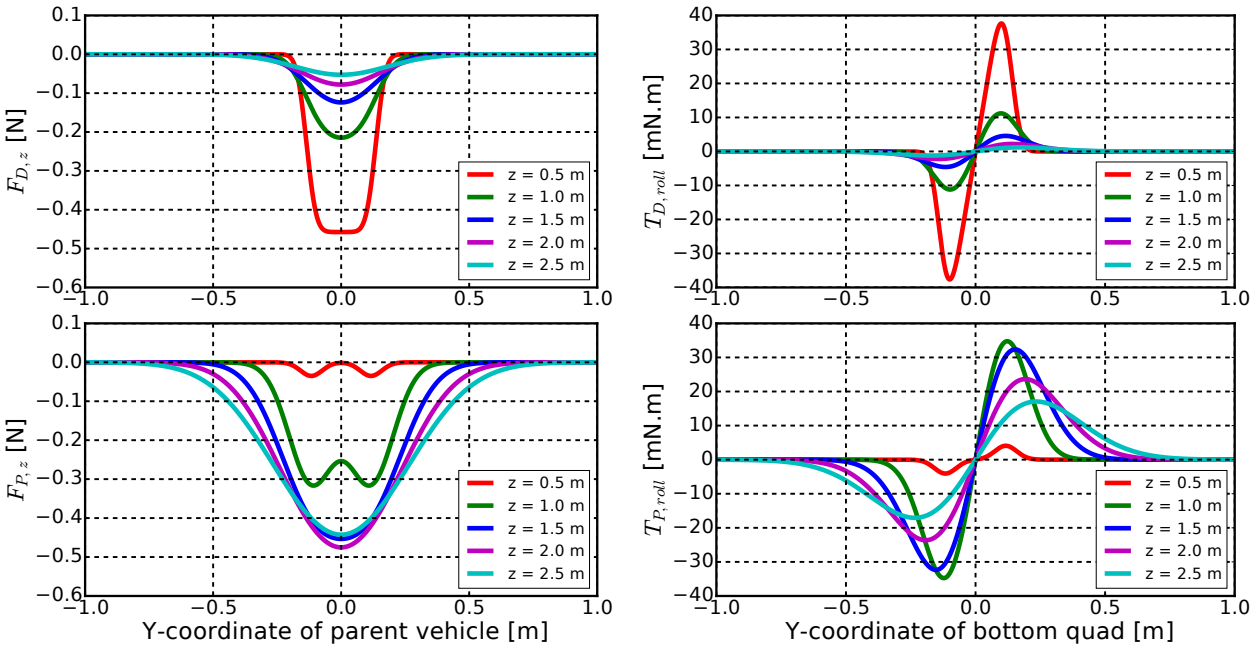

Figure B.4: Predicted values of aerodynamic forces in z-direction (left) and roll torques (right) due to drag (top) and change in propeller thrust (bottom)

B.6 Experimental validation

We present the experimental data for aerodynamic disturbance force and torque experienced by the large quadcopter when flying in proximity to the small quadcopter. The experiments conducted are described in Section B.5. The aerodynamic disturbances are estimated using data from the accelerometer, rate-gyro, and propeller forces.

Force disturbance equations

The output of accelerometer ($\boldsymbol{\alpha}$) is related to linear acceleration of the body ($\boldsymbol{a}$) as,

$$\boldsymbol{R\alpha} = \boldsymbol{a} - \boldsymbol{g} \tag{B.9}$$

where $\boldsymbol{g}$ is the acceleration due to gravity, and $\boldsymbol{R}$ is a rotation matrix which converts body frame vectors to the inertial frame. The rotation matrix is obtained via the roll, pitch and yaw angles of the quadcopter.

Application of Newton's second law to the large quadcopter shown in Figure B.1 yields,

$$m\boldsymbol{a} = \boldsymbol{f}_p + \boldsymbol{f}_a + m\boldsymbol{g} \tag{B.10}$$

where m is the mass of the body, $\boldsymbol{f}_a$ is the aerodynamic force, and $\boldsymbol{f}_p$ is the total propeller force.

Combining equations (B.9) and (B.10), we get,

$$\boldsymbol{f}_a = m\boldsymbol{R\alpha} - \sum_{i=1}^{4} f_{pi}\boldsymbol{z}_B \tag{B.11}$$

We have access to f_{pi}'s from the input PWM signal and a-priori propeller calibration data. We also have data of position and orientation of each quadcopter from the motion-capture system, which can be used to calculate relative horizontal and vertical separations between the vehicles. Thus, we can estimate aerodynamic forces as a function of relative separation between the quadcopters.

Torque disturbance equations

The onboard rate-gyro gives us angular velocity. This can be differentiated using the forward Euler method to estimate angular acceleration as follows,

$$\dot{\boldsymbol{\omega}}_k = \frac{\boldsymbol{\omega}_{k+1} - \boldsymbol{\omega}_k}{t_{k+1} - t_k} \tag{B.12}$$

Applying Newton's second law for rotation to the large quadcopter, we can write,

$$\boldsymbol{RJ}\dot{\boldsymbol{\omega}} = \boldsymbol{R}\boldsymbol{\tau}_p + \boldsymbol{\tau}_a \tag{B.13}$$

Here, $\boldsymbol{J}$ is the mass moment of inertia tensor of the body, $\boldsymbol{\tau}_a$ is the aerodynamic torque in the inertial frame, $\boldsymbol{\tau}_p$ is torque due to propeller forces in the body frame, and $\boldsymbol{\omega}$ and $\dot{\boldsymbol{\omega}}$ are the angular velocity and angular acceleration of the body in the body frame.

The torque due to propellers is a result of differences in propeller forces which create a moment about the center of the quadcopter. Referring to Figure B.1, we get,

$$\tau_{px} = \frac{l}{\sqrt{2}}[(f_{p3} + f_{p4}) - (f_{p1} + f_{p2})] \tag{B.14a}$$

$$\tau_{py} = \frac{l}{\sqrt{2}}[(f_{p2} + f_{p3}) - (f_{p1} + f_{p4})] \tag{B.14b}$$

$$\tau_{pz} = \mathrm{k_t}[(f_{p2} + f_{p4}) - (f_{p1} + f_{p3})] \tag{B.14c}$$

where $\mathrm{k_t}$ is the torque to thrust ratio of a propeller, which is obtained experimentally using an RC Benchmark Series 1580 thrust stand.

Experimental results

Figure B.5 shows the experimentally estimated aerodynamic force and torque experienced by the large quadcopter flying below the small quadcopter. Predicted values from the model are also plotted for comparison.

The forces and torques start from zero at high values of r, which is expected because the downwash velocities are very low in this region. As the large quadcopter moves closer to $r = 0$, the magnitude of forces starts to increase and achieves a maximum at $r = 0$. On the other hand, the torques attain a maximum at some non-zero r and go to zero at $r = 0$. This is expected because at $r = 0$, the forces on the quadcopter are distributed symmetrically.

The above observation is valid for both predicted values and experimental estimates. The key observation here is that aerodynamic disturbance torque is restoring, i.e. if the large quadcopter moves out of vertical alignment with respect to the small quadcopter, it is affected such that it realigns itself.

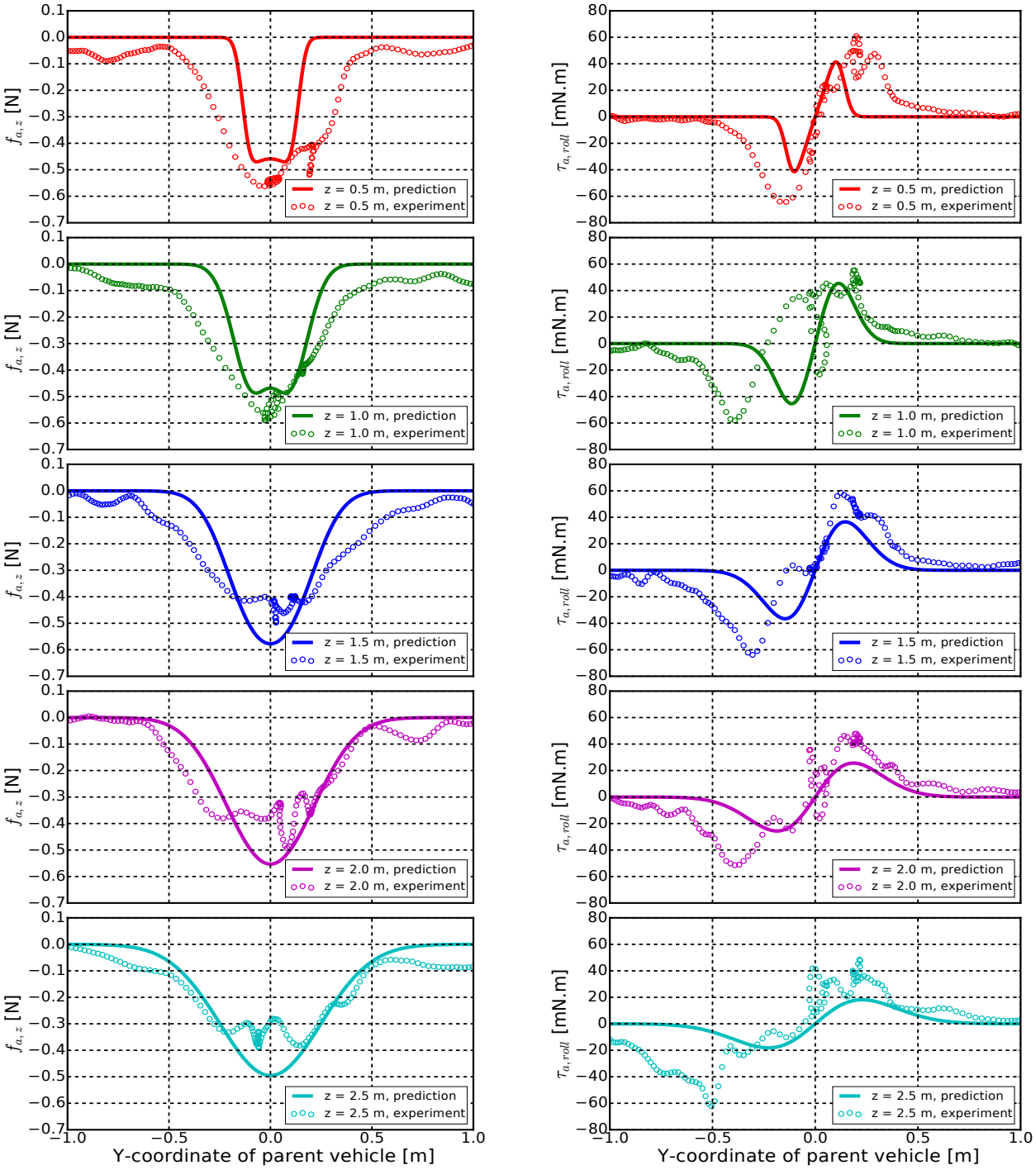

Figure B.5: Aerodynamic forces in z-direction (left) and roll torques (right). Solid lines show predicted values due to combined effect of drag and change in propeller thrust. Scatter plots show experimentally derived values.